2001

Design, Fabrication, and Testing of Cross Flow Micro Heat Exchangers.

Chad Randall Harris
Louisiana State University and Agricultural & Mechanical College

INFORMATION TO USERS

This manuscript has been reproduced from the microfilm master. UMI films the text directly from the original or copy submitted. Thus, some thesis and dissertation copies are in typewriter face, while others may be from any type of computer printer.

The quality of this reproduction is dependent upon the quality of the copy submitted. Broken or indistinct print, colored or poor quality illustrations and photographs, print bleedthrough, substandard margins, and improper alignment can adversely affect reproduction.

In the unlikely event that the author did not send UMI a complete manuscript and there are missing pages, these will be noted. Also, if unauthorized copyright material had to be removed, a note will indicate the deletion.

Oversize materials (e.g., maps, drawings, charts) are reproduced by sectioning the original, beginning at the upper left-hand corner and continuing from left to right in equal sections with small overlaps.

Photographs included in the original manuscript have been reproduced xerographically in this copy. Higher quality 6" x 9" black and white photographic prints are available for any photographs or illustrations appearing in this copy for an additional charge. Contact UMI directly to order.

ProQuest Information and Learning
300 North Zeeb Road, Ann Arbor, MI 48106-1346 USA
800-521-0600

UMI®

NOTE TO USERS

This reproduction is the best copy available.

UMI®

DESIGN, FABRICATION, AND TESTING OF CROSS FLOW MICRO HEAT EXCHANGERS

A Dissertation

Submitted to the Graduate Faculty of the
Louisiana State University and
Agricultural and Mechanical College
in partial fulfillment of the
requirements for the degree of
Doctor of Philosophy

in

The Department of Mechanical Engineering

by
Chad Harris
B.S., Louisiana State University, 1997
May 2001

DEDICATION

To my family and my wife, Katy

ACKNOWLEDGMENTS

I would like to give thanks to the people that I have worked with since I began my graduate career. My advisor, Dr. Kevin Kelly has always offered advice and been fair. His cooperation has enabled me to finish my work efficiently.

There were several other people essential to the proficient completion of the micro heat exchangers. Dr. Mircea Despa has assisted in many facets of the project and is the person who made molding possible. Andrew McCandless was always there to answer any micro fabrication procedure questions. Paul Rodriguez provided advice on a variety of issues. Emil Geiger was essential to the high quality of the final microstructures produced.

I am grateful to Dr. Elizabeth Podlaha, Dr. Dimitris Nikitopoulus, and Dr. Warren Waggenspack for accepting my invitation to be members of my committee.

This work was made possible by innovative equipment available at the Center for Advanced Microstructures and Devices as well as funding provided by the Defense Advanced Research Project Agency.

TABLE OF CONTENTS

Dedication.....ii

Acknowledgments.....iii

Abstract.....vi

Chapter I-Introduction.....1

Chapter II-Scaling.....3
II.1. Analysis.....3
II.2. Discussion.....4

Chapter III-Literature Review.....6
III.1. Conventional Scale Cross Flow Heat Exchangers.....8
III.2. Compact Heat Exchangers.....9
III.3. Electronic Cooling.....10
III.4. Cross Flow Micro Heat Exchangers with Equal Channel Dimensions.....11
III.5. Heat Exchanger Comparison.....13
III.6. Other Micro Heat Exchangers.....14

Chapter IV-Design and Modeling.....15
IV.1. Conceptual Design.....15
IV.2. Performance Parameters.....17
IV.3. Design Constraints.....18
IV.4. Optimization and Modeling Calculations.....20
IV.5. Results.....31

Chapter V-Fabrication.....38
V.1. Overview of LIGA Process.....38
V.2. Procedure.....39
V.3. Results.....56

Chapter VI-Testing.....59
VI.1. Apparatus.....59
VI.2. Procedure.....60
VI.3. Uncertainty Analysis.....65
VI.4. Results.....65

Chapter VII-Metal Cross Flow Micro Heat Exchanger.....73
VII.1. Introduction.....73

VII.2. Design....73
VII.3. Fabrication....87
VII.4. Testing....100

Chapter VIII-Performance Discussion....106

Chapter IX-Conclusions and Recommendations....110
IX. 1 Conclusions....110
IX.2 Recommendations for Future Work....111

Bibliography....112

Nomenclature....118

Appendix A: Program for Design Optimization....119

Appendix B: Finite Element Modeling....126

Appendix C: Uncertainty Analysis....131

Appendix D: Microfabrication Procedures....136

Vita....138

ABSTRACT

Cross flow micro heat exchangers were designed to maximize heat transfer from a liquid (water) to a gas (air) for a given frontal area while holding the pressure drop across the heat exchanger of each fluid to values characteristic of conventional scale heat exchangers (car radiators). The cross flow micro heat exchanger design is unique since it produces a very high rate of heat transfer/volume between dissimilar fluids with low fluid pressure drops. Predicted performance for two types of cross flow micro heat exchangers is compared to each other and to current innovative car radiators. Although the cross flow micro heat exchanger has a lower rate of heat transfer/frontal area, it can transfer more heat/volume or mass than existing heat exchangers within the context of the design constraints specified. This can be important in a wide range of applications (automotive, home heating, and aerospace). One type of cross flow micro heat exchanger was fabricated by aligning, then bonding together, two plastic parts that had been molded using the LIGA process. The other type of heat exchanger was fabricated by first electroless plating a layer of nickel over a plastic part molded using the LIGA process, then dissolving the plastic. Performance of the fabricated heat exchangers was measured and compared to the predicted performance. At the design constraints, the mathematical model predicted the fluid pressure drops and heat transfer performance within 10% of the measured performance for the fabricated cross flow micro heat exchangers.

CHAPTER I – INTRODUCTION

The ability to efficiently transfer heat between fluids using lightweight, compact heat exchangers is important in a variety of applications such as automobile radiators, air conditioning, and aircraft components. To accomplish this goal, micro channels with characteristic diameters ranging from 100 μm to 1 mm can be utilized. By constraining the flow to narrow channels, heat transfer is enhanced since the surface area/volume ratio increases and the convective resistance across a solid/fluid interface decreases. However, the well-known benefits of small channels with respect to heat transfer must be weighed against the costs of the steep pressure gradient associated with flow through micro channels. To reap the benefits of micro channels while minimizing the penalty associated with a large pressure gradient, two types of cross flow micro heat exchangers have been designed, built, and tested. In these heat exchangers, gas (i.e. air) passes through the plane of the heat exchanger via thousands of parallel short channels. Although the pressure gradient within the air channels is steep, the numerous short channels allow a large mass flow rate through the heat exchanger with a low total pressure drop. Despite the short length of the channels, the rise in the air temperature is significant. The result of micro channels in a cross flow design is a heat exchanger with high ratios of heat transfer/weight and heat transfer/volume.

The cross flow micro heat exchanger's combination of heat transfer enhancement between a liquid and a gas using micro channels and a low pressure drop of the fluids is unique. Other heat exchangers with similarities to the cross flow micro heat exchanger include conventional scale cross flow heat exchangers such as car radiators, compact

heat exchangers, electronic cooling micro heat exchangers, and cross flow micro heat exchangers with equal channel dimensions.

Due to the size of the micro channels, innovative manufacturing techniques need to be utilized to fabricate the micro heat exchanger. Various techniques that can be used to manufacture micro heat exchangers are molding, lithography, electro/electroless plating, chemical etching, diamond bit micro machining, micro electro-discharge machining, and ion beam machining. In this work, a combination of photo lithography, x-ray lithography, electro/electroless plating, and molding were used to fabricate the cross flow micro heat exchangers.

The objective of this research was to design, fabricate, and test cross flow micro heat exchangers to efficiently transfer heat between a liquid and a gas in a small volume. Two types of heat exchangers with similar dimensions (0.1-1mm) that vary in material and fabrication methods were used to accomplish this objective. For both types of heat exchangers, the mathematical models and design calculations are summarized and the design performance of the heat exchangers is compared to innovative car radiators on a basis of size, weight, pressure drop of the fluids, and heat transfer/frontal area. Each step of the heat exchanger fabrication is also explained. Finally, experiments performed on the fabricated heat exchangers are described and the experimental results are compared to the models.

CHAPTER II – SCALING

The scaling laws explained in this chapter provide insight into the advantages of micro heat exchangers.

II.1. Analysis

The effect of size on heat exchanger performance under typical design constraints will be examined. For the scaling analysis, the pressure drop and fluid temperature change will be the design constraints and assumed constant. Scaling advantages will be examined for laminar, fully developed fluid flow through a heat exchanger composed of numerous parallel circular channels with a constant wall temperature. The percentage of the total frontal area the channels occupy is assumed constant, regardless of scale. In other words, as the channel size decreases, the number of channels per unit area increases. Inlet and exit effects will be neglected. In reality, entrance and exit effects are significant and the fluid flow is often not fully developed, thus the scaling laws are only approximate.

For fluid flow through circular channels the pressure drop (Δp) across the length (L) of the channel is given by Equation (II.1).

$$\Delta p = \frac{32\mu VL}{D^2} = Constant * V * \frac{L}{D^2} \qquad \text{(II.1)}$$

V is the average fluid velocity, μ is the fluid viscosity, and D is the diameter of the channel.

As the fluid traverses the channel, it will be heated or cooled depending on the wall temperature (T_w). The fluid exit temperature is calculated using Equation (II.2).

$$\frac{T_w - T_{exit}}{T_w - T_{inlet}} = \exp\left(\frac{-PLh}{\dot{m}c_p}\right) \qquad \text{(II.2)}$$

T_{inlet} is the temperature of the fluid entering the channel, T_{exit} is the temperature of the fluid exiting the channel, P is the perimeter (πD) of the channel, h is the convection coefficient, $\dot{m}$ is the mass flow rate ($\rho V \pi D^2/4$), and c_p is the specific heat of the fluid.

The convection coefficient is calculated using Equation (II.3).

$$h = \frac{k_{fluid} Nu}{D} \tag{II.3}$$

k_{fluid} is the thermal conductivity of the fluid and Nu is a constant termed the Nusselt number.

By substituting expressions for the channel perimeter, convection coefficient, and mass flow rate into Equation (II.2) and assuming fluid properties are independent of temperature, an expression for the exit fluid temperature as a function of scale is derived and given in Equation (II.4).

$$\ln\left(\frac{T_w - T_{exit}}{T_w - T_{inlet}}\right) = \frac{-128\mu k_{fluid} Nu}{\rho \Delta p c_p} \frac{L^2}{D^4} = Constant * \frac{L^2}{D^4} \tag{II.4}$$

Inspection of Equations (II.1) and (II.4) indicate that if the ratio of L/D^2 is held constant, the pressure drop across the heat exchanger, the velocity of the fluid, and the exit temperature of the fluid are constant.

The heat transfer rate (q) can be calculated using Equation (II.5).

$$q = \dot{m} c_p (T_{exit} - T_{inlet}) \tag{II.5}$$

The heat transfer rate is invariable for constant L/D^2 ratios since the mass flow rate and fluid temperatures are constant.

II.2. Discussion

The analysis shows that under basic assumptions, heat exchanger performance scales with the ratio of L/D^2. As the length of the channel is increased or the diameter of the

channel is decreased, the fluid exits the channel closer to the wall temperature and the fluid experiences a larger pressure drop. Decreasing the channel length or increasing the diameter of the channel would result in the opposite effect.

Since the percentage of the total frontal area the channels occupy is assumed constant, the volume of the heat exchanger scales with the length of the channel. For constant L/D^2 ratios, the volume also scales with the inverse of the channel diameter squared. This illustrates the primary advantage of micro heat exchangers. For the two heat exchanger channel dimensions shown in Table II.1 with identical L/D^2 ratios, the volume of the larger heat exchanger is 100 times bigger than the smaller heat exchanger. Additionally, the smaller heat exchanger is lighter, and given that less material is used to fabricate the heat exchanger, the smaller heat exchanger may be less expensive to fabricate. Since the L/D^2 ratios are the same, the heat exchangers transfer the same amount of heat with the same fluid pressure drop. Disadvantages to the smaller heat exchanger are reduced strength and possible additional filtering requirements.

Table II.1 – Heat exchanger dimensions

	L	D
Smaller Heat Exchanger	2 mm	0.2 mm
Larger Heat Exchanger	20 cm	2 mm

CHAPTER III - LITERATURE REVIEW

The performance of the cross flow micro heat exchangers cannot be compared directly to other micro channel heat exchangers that have been fabricated and described in the literature. Heat exchangers with similarities to the cross flow micro heat exchangers include: cross flow conventional scale heat exchangers (Figure III.1), compact heat exchangers (Figure III.2), micro electronic cooling heat exchangers (Figure III.3), and cross flow micro heat exchangers with equal channel dimensions (Figure III.4). Differences between these heat exchangers and the cross flow micro heat exchangers are the heat transfer media (liquid and gas), size of the micro channels (less than 1 mm), fluid pressure drops (less than 1 psi), and cost/ease of fabrication (molding). A tabular performance summary of the following heat exchangers is shown near the end of the chapter in Table III.1. The performance for the two types of cross flow micro heat exchangers (discussed in subsequent chapters) is also included for comparison purposes.

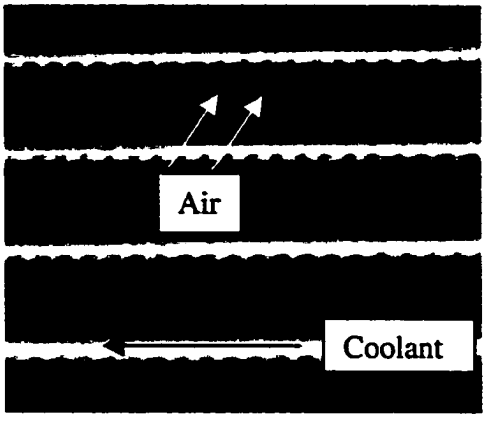

Figure III.1 – Cross flow conventional scale heat exchanger (car radiator)

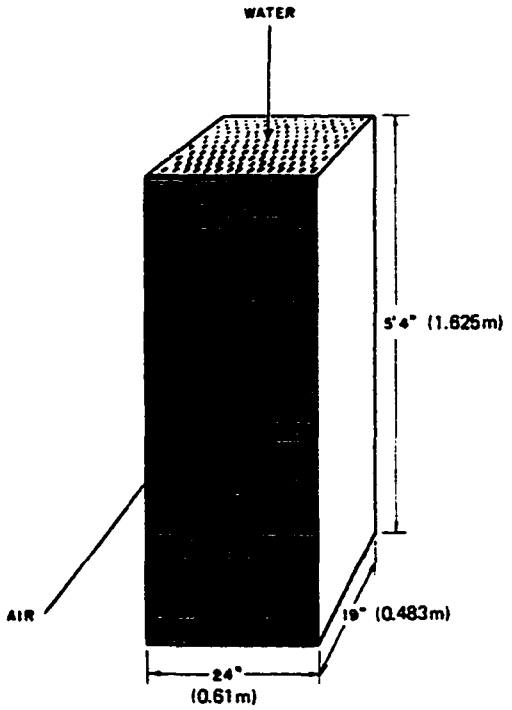

Figure III.2 – Compact heat exchanger [3]

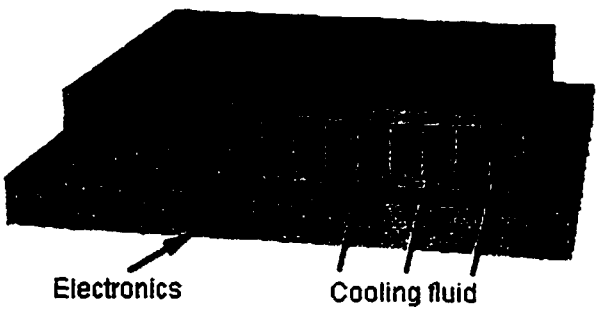

Figure III.3 – Electronic cooling heat exchanger

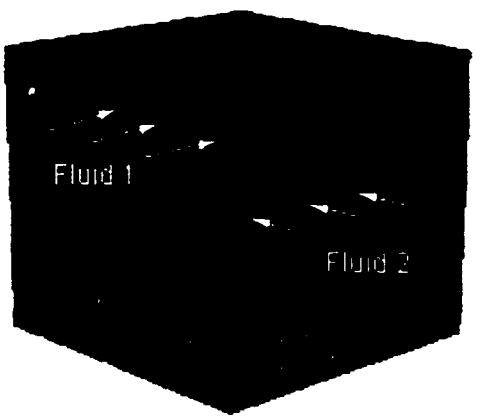

Figure III.4 – Cross flow micro heat exchanger with equal channel dimensions

III.1. Conventional Scale Cross Flow Heat Exchangers

Examples of conventional scale cross flow heat exchangers are car radiators (Figure III.1), condensers, and evaporators. Since car radiators are the most similar to the cross flow micro heat exchangers that will be discussed, they will be described in this section.

Car radiators are used to reduce the temperature of engine coolant. They employ a cross flow design that allows a sufficient mass flow rate of air through the radiator while using only the stagnation pressure associated with the motion of the automobile. Although micro channels are not utilized to enhance heat transfer, the conceptual design and pressure drops in a car radiator are similar to the cross flow micro heat exchangers. Innovative car radiators will be used as the basis of comparison for the cross flow micro heat exchangers.

In innovative car radiators, typical characteristic diameters for the air and coolant channels are 3 mm and 5 mm, respectively, and typical channel lengths for the air and coolant channels are 3 cm and 60 cm, respectively. These heat exchangers are thin compared to their large surface area and their air channels are relatively short compared their diameter ($L/D^2 = 3.3\ mm^{-1}$).

A common measure of performance for car radiators is the heat transfer/frontal area, normalized by the difference in inlet temperatures of the engine coolant (water-glycol) and the air. For current innovative car radiators [1,2], a heat transfer/area rate of 3 kW/m^2-K can be removed from the engine coolant. However, these radiators are extremely thick (1-4 cm) compared to the thickness of the micro heat exchangers that will be described (0.1-0.2 cm). Rates of heat transfer/volume and heat transfer/mass of these innovative car radiators [1,2] are around 100 kW/m^3-K and 275 W/kg-K using an

air pressure drop of 0.02 psi and engine coolant pressure drop of 0.72 psi. Although the rate of heat transfer per area is greater than the cross flow micro heat exchangers, the rate of heat transfer per volume is less than the cross flow micro heat exchangers. The air pressure drop is comparable and the water pressure gradient is an order of magnitude less than the cross flow micro heat exchangers. Since considerably greater power is required to pump a gas than a liquid, the air pressure drop is usually considerably more important than the coolant pressure drop. A more detailed comparison is given in Chapter VIII.

III.2. Compact Heat Exchangers

Compact heat exchangers transfer heat between fluids (gas to gas, liquid to liquid, or gas to liquid) with a high rate of heat transfer/volume compared to larger heat exchangers. To accomplish this, compact heat exchangers have a high heat transfer surface area compared to its volume. Typically, the fluid channels in compact heat exchangers are an order of magnitude larger and the fluid pressure drops are higher than the cross flow micro heat exchanger. The larger fluid channels result in a lower rate of heat transfer/volume compared to micro heat exchangers since the heat transfer enhancement of micro channels is not utilized.

As a basis of comparison, a compact heat exchanger (shown in Figure III.2) that uses a cross flow orientation to transfer heat between a gas (air) and a liquid (water) will be described [3]. For this compact heat exchanger, typical characteristic diameters for the air and water channels are 1.8 mm and 1.9 mm, respectively, and typical channel lengths for the air and water channels are 48 cm and 163 cm, respectively. The compact heat exchanger has comparable air and water channel dimensions and air channels that

are relatively long compared their diameter (L/D^2 = 148 mm^{-1}). The compact heat exchanger's rates of heat transfer/volume and heat transfer/frontal area of 69 W/m^3-K and 33 kW/m^2-K are achieved with an air pressure drop of 0.3 psi and water pressure drop of 2.1 psi. Again, the rate of heat transfer per area is greater and the rate of heat transfer per volume is less than the cross flow micro heat exchangers. The air pressure drop is an order of magnitude greater and the water pressure gradient is an order of magnitude less than the cross flow micro heat exchangers.

III.3. Electronic Cooling

When power is transmitted through electronic components, heat is generated. Although electronic components are becoming smaller, the heat generated in electronics is increasing. The resulting increase in heat flux drives the development of innovative cooling schemes that utilize micro channels. Current micro heat exchanger research is concentrated in the field of electronic cooling.

Typical electronic cooling micro heat exchangers transfer heat between a substrate and fluid as shown in Figure III.3. This is very different than the cross flow micro heat exchanger that transfers heat between a liquid and a gas. In addition, electronic micro heat exchangers typically employ high fluid pressure drops. Therefore, the only similarity between electronic cooling heat exchangers and the cross flow micro heat exchangers is the use of micro channels for heat transfer enhancement.

A summary of micro electronic heat exchangers using different fluids and cooling schemes to remove heat from a substrate is now summarized. Tuckerman and Pease [4] performed early research in micro channel heat transfer. Using micro channels with a length of 1 cm and characteristic diameter of 86 μm, 111 kW/m^2-K of heat was

removed from a substrate using water with a pressure drop of 30 psi. The majority of studies have used liquid (since it provides ten to one hundred times the performance of air cooling [4,5]) but studies have also been performed using air. Lower cost, lower maintenance, and higher reliability are attributes of air cooling. Kleiner [6] used micro channels with a length of 5 cm and characteristic diameter of 874 μm to achieve heat transfer rates of 2.5 kW/m^2-K using air to cool a substrate with a pressure drop of 0.25 psi. Hilbert [7] used a different air cooling scheme utilizing impingement to theoretically remove 50 kW/m^2-K from a substrate with a pressure drop of only 0.007 psi, however no experiments were performed. Wegeng et al. [8] used two-phase flow to achieve a heat transfer rate of 6.2 kW/m^2-K with a pressure drop of 1 psi. The rate of heat transfer/volume is not used as a measure of performance for electronic cooling heat exchangers. Numerous additional studies into electronic cooling using micro channels exist [9-16], however the research discussed has the highest heat transfer rates per unit area and provide the pressure drop of the fluid.

III.4. Cross Flow Micro Heat Exchangers with Equal Channel Dimensions

The cross flow micro heat exchanger with equal dimensions (Figure III.4) uses stacked micro channel plates alternating by 90° to create a heat exchanger with a very high rate of heat transfer/volume. A disadvantage of the stacking method is the cost and time involved in manufacturing and bonding together numerous plates. To simplify fabrication, fluids with similar properties are typically used as the heat transfer media to enable efficient heat transfer using identical stacked plates. Using different dimensions for the alternating micro channel plates would allow more effective heat transfer between dissimilar fluids, however the difficulty of fabrication would be increased. As

a result, all of the research for this type of heat exchanger involves heat transfer between the same fluids.

For water-water heat exchange in a cross flow micro heat exchangers with equal channel dimensions, Bier et al.[17] used 1 cm long micro channels with a characteristic diameter of 88 μm to achieve an extremely high heat transfer rate of 234 MW/m^3-K with both fluids experiencing high pressure drops of 59 psi. Kang [18] fabricated a similar heat exchanger for water-water heat exchanger consisting of 1.9 cm long micro channels with a characteristic diameter of 101 μm. This heat exchanger had a lower heat transfer rate of 30 MW/m^3-K with both fluids experiencing pressure drops of 50 psi. For an air-air heat exchanger, Rachovskij et al.[19] used micro channels with a length of 1.2 mm and a characteristic diameter of 128 μm to theoretically achieve a heat transfer rate of 4.3 MW/m^3-K with both fluids experiencing pressure drops of 0.037 psi. Rachovskij's rate of heat transfer per volume was normalized by the volume of the air channels (not the volume of the heat exchanger) and the temperature difference between the inlet fluid temperature and the wall temperature (not the difference in the inlet temperature of the different fluid streams). For nitrogen-nitrogen heat transfer in a copper heat exchanger consisting of micro channels with a length of 1.4 cm and a characteristic diameter of 88 μm, Bier et al. [20] achieved a heat transfer rate of 1.0 MW/m^3-K when the heated nitrogen fluid stream experienced a pressure drop of 0.88 psi. Although the rate of heat transfer/area is not typically used as a measure of performance for cross flow micro heat exchangers with equal channel dimensions, the rate of heat transfer/area was estimated for the data shown in Table III.1 using the geometries given for the heat exchangers. Although these cross flow micro heat

exchangers with equal dimensions have greater rates of heat transfer per volume than the cross flow micro heat exchanger, their pressure drops are greater and fabrication is more difficult the cross flow micro heat exchangers. A more detailed comparison between the cross flow micro heat exchanger with equal channel dimensions used to transfer heat between nitrogen streams and the cross flow micro heat exchangers is given in Chapter VIII.

III.5. Heat Exchanger Comparison

The performance and scaling parameter of many of the heat exchangers discussed in this chapter are summarized in Table III.1. Although it is difficult to compare heat exchangers with different fluids, geometries, temperatures, and pressure drops, Table III.1 gives a very general comparison of the performance of many different heat exchangers. The optimum heat exchanger will depend on the application.

Table III.1 – Summary of heat exchanger performance and scaling parameters

Heat Exchanger (CF = Cross Flow)	Fluid Δp (psi)	L/D^2 (mm^{-1})	q/A (kW/m^2-K)	q/V (MW/m^3-K)
Plastic CF Micro	Air – 0.026 Water – 0.72	Air – 15 Water – 150	0.58	0.40
Metal CF Micro	Air – 0.026 Water – 0.72	Air – 7.4 Water – 420	1.3	1.0
Conventional Scale CF - Car Radiator [1]	Air – 0.026 Cool – 0.25	Air – 3.3 Cool– 24	3.1	0.12
Compact [3]	Air – 0.30 Water – 2.1	Air – 150 Water – 450	33	0.069
Electronic Cooling Micro [4]	Water – 30	NA	110	NA
Electronic Cooling Micro [6]	Air – 0.25	NA	2.5	NA
CF Micro – Equal Channel Dim. [17]	Water – 59 Water – 59	Water – 1300 Water – 1300	2300	230
CF Micro – Equal Channel Dim. [20]	N_2 – 0.88 N_2 – 0.15	Nit. – 1800 Nit. – 1800	6.4	0.46

III.6. Other Micro Heat Exchangers

The four types of heat exchangers explained represent the majority of heat exchangers with similarities to the cross flow micro heat exchanger. Additional micro heat exchanger research efforts include cryocoolers for cooling sensors and diode lasers [21,22], stirling engines [23], seal faces [24], turbine blades [25,26], and chemical reactors [27,28].

CHAPTER IV – DESIGN AND MODELING

IV.1. Conceptual Design

The objective of this research was to efficiently transfer heat between air and water in a small volume with low fluid pressure drops. Initially the design shown in Figure IV.1 was attempted to accomplish this goal. Alternating air and water layers are stacked with micro channels on each layer to enhance heat transfer.

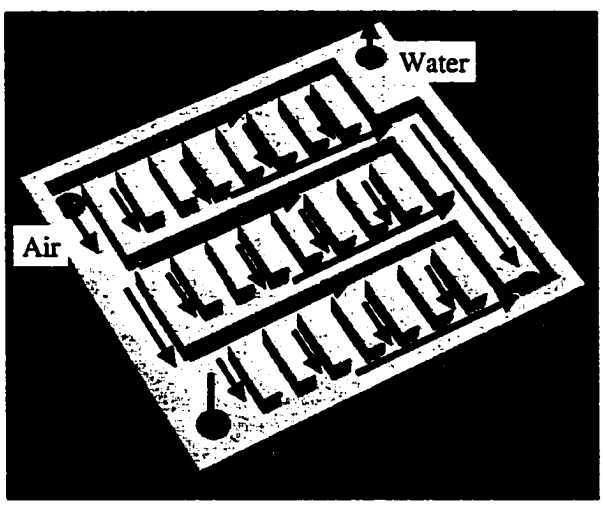

Figure IV.1 – Initial micro heat exchanger

This design was fabricated in plastic and tested. A picture of the micro channels on the fabricated initial micro heat exchanger is shown in Figure IV.2. Since the primary resistance to heat transfer is in the air layer, the heat exchanger was tested by bonding the heat exchanger to a heated aluminum block and measuring the air flow rate, pressure drop, heat input to the aluminum, and inlet and exit temperatures. The experimental results of this heat exchanger were disappointing. The pressure drop of the air was extremely high due to the relatively small area that the air had to pass through to reach the micro channels compared to the open cross sectional area of the micro channels. To achieve a heat transfer rate of 0.344 kW/m^2-K, a pressure drop of 3.1 psi was needed. This pressure drop was unacceptably high.

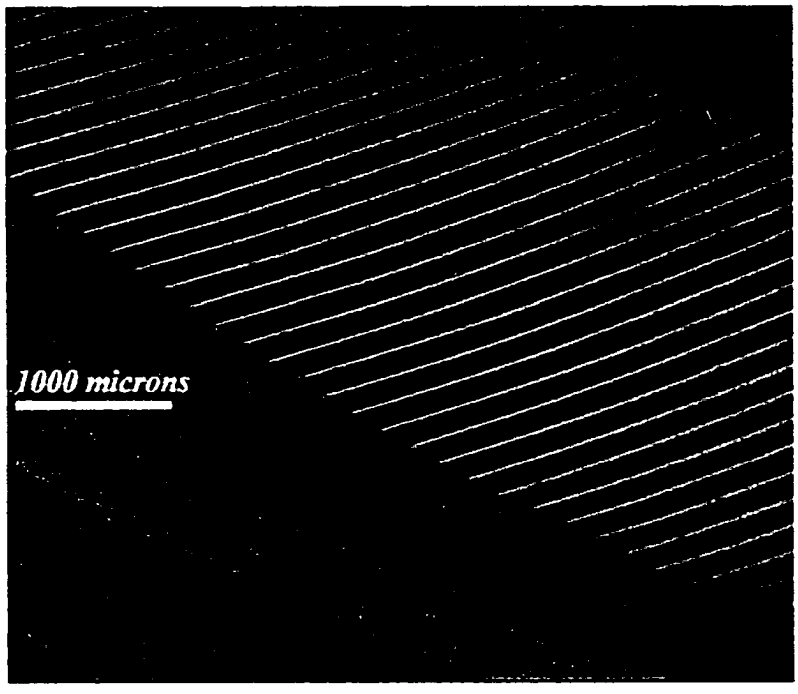

Figure IV.2 – Fabricated plastic initial micro heat exchanger

Therefore a new design was developed to reduce the air pressure drop. Using a cross flow heat exchanger similar to a car radiator allows a large open area for air to flow through the heat exchanger. The conceptual design for this type of heat exchanger is shown in Figure IV.3.

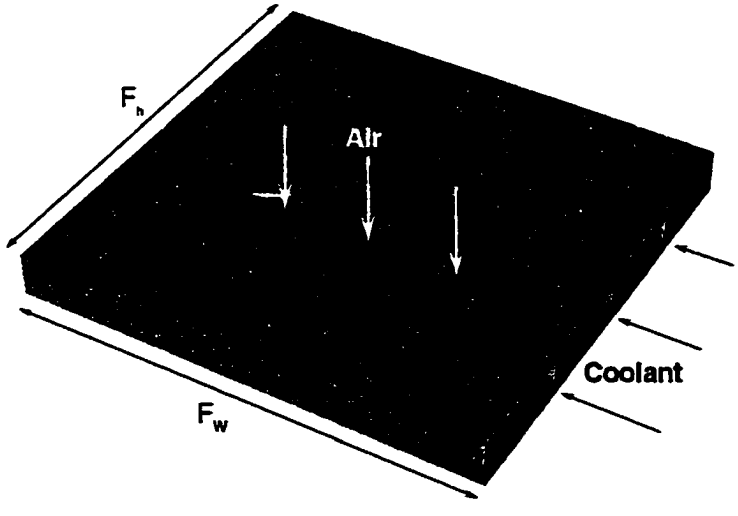

Figure IV.3 – Cross flow micro heat exchanger

As shown in the previous chapter, the cross flow micro heat exchanger can transfer heat at a rate of 0.58 kW/m^2-K using an air pressure drop of 0.026 psi. This is far superior to the initial design.

IV.2. Performance Parameters

In order to design the cross flow micro heat exchanger, performance criteria were established. Due to the similarity of design, a car radiator was selected as the application. The performance criteria will likely be slightly different for other applications such as air conditioning and aerospace, but the majority of principles that will be discussed can be extended to other applications.

The goal of a car radiator is to dissipate heat to atmospheric air to prevent the engine from overheating. For a given set of design constraints (i.e. pressure drop of each fluid and difference in inlet temperature between the two fluids) a well-designed cross flow radiator provides a high rate of heat transfer/frontal area of the radiator. Other measures of design performance include weight, size, noise, and filtering requirements. The goal described in this chapter is to design a cross flow micro heat exchanger to maximize heat transfer/frontal area within specified design constraints. Other performance parameters include rates of heat transfer/mass and heat transfer/volume. Noise and filtering requirements are also mentioned as possible performance parameters. Noise calculations were not performed. Since velocities and flow rates are similar to existing car radiator designs, the noise should be similar. Filtering requirements of the cross flow micro heat exchanger are expected to be greater than a car radiator that needs virtually no filtering. The purpose of this research is to compare the performance of the micro heat exchanger with a conventional scale heat exchanger, disregarding the

filtering issue. However, the filtering issue will eventually need to be addressed in cases where the micro heat exchanger offers a possible advantage.

IV.3. Design Constraints

Fluids

The fluids chosen to transfer heat in the cross flow heat exchanger were air and water. These fluids are non-toxic, readily available for testing, and common to many heat exchangers.

Pressure drop of fluids

The head produced by typical fans, or in the case of an automobile, the stagnation head associated with an automobile running at 50 miles per hour, provide a reasonable measure of the typical pressure drop of the air across the heat exchanger. Many fans can produce substantial flow rates across a pressure differential of 175 Pa (0.7 inches of water). Therefore the pressure drop of the air across the heat exchanger was specified at 175 Pa. The pressure drop of the water should be minimized to reduce pumping requirements. A reasonable low end pressure drop from the literature [1,2,29] is 5 kPa. This is the value specified for the micro heat exchanger. The specified value for the pressure drop of the water is far less crucial to the design process than that of the air since the work to pump the liquid is much less than the work to pump the air.

Temperature of the fluids

The inlet temperatures for the air and water were chosen to be 25° and 58°C because these are the temperatures that will be used during testing. Generally, the heat transfer numbers will be normalized by the difference in temperature between the inlet fluids.

Geometry

A basic schematic of the cross flow micro heat exchanger was shown in Figure IV.3. The size of the heat exchanger designed (F_w = 5.1 cm, F_h = 5.1 cm) is limited by the present manufacturing infrastructure at LSU. However the dimensions could be increased dramatically if the need existed. The dimensions that specify the internal geometry of the heat exchanger are shown in Figure IV.4.

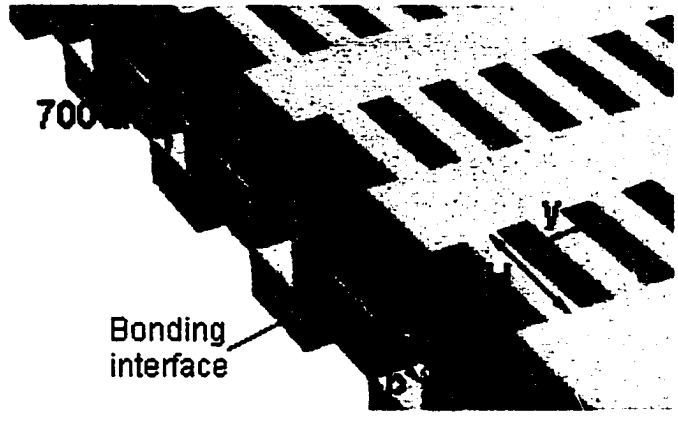

Figure IV.4 – Schematic for geometric design constraint variables

The cross section of each air channel (w x H) is a variable. The width of the fins (y) separating adjacent channels is also a variable. For strength and manufacturing considerations, the minimum allowed values of both the fin width (y) and the channel width (w) is set at 200 μm. The thickness of the wall (a) separating the water and air is not a design variable and is given a value of 125 μm. This value is chosen primarily because the alignment and bonding of the upper and lower halves of the heat exchanger over dimension (a) is crucial to ensure the water channels are sealed. While a smaller value of (a) produces a more effective heat exchanger, there was concern that the alignment/sealing of the water channels would be unsuccessful if the wall was too thin. The width of the water channel (b) is another variable. To ensure adequate water flow

area and for manufacturing considerations, the minimum allowed value for the width of the water channel is set at 500 μm. The maximum depth of the water channel was limited to 700 μm. Although a larger depth would slightly improve performance by allowing a larger flow rate of water given the water pressure drop constraint, the maximum depth was chosen to ensure sufficiently thick water channel walls for strength. Finally, present micro manufacturing capabilities at LSU limit the thickness of each half of the heat exchanger to 1.0 mm. This could be increased to 2 mm if the need existed. Since the final step of the manufacturing process involves fly cutting and polishing (see Chapter V – Fabrication), the thickness of each half is reduced. Therefore, the maximum length of the channels (L) for an assembled heat exchanger, within the present manufacturing limitations, is 1.45 mm.

IV.4. Optimization and Modeling Calculations

The geometry that maximizes heat transfer/frontal area has been calculated for plastic, ceramic, and aluminum micro cross flow heat exchangers. The heat exchanger shown in Figure IV.3 is fabricated by bonding together two molded plastic halves. Presently, only plastic parts are molded at Louisiana State University, but designs for ceramic and aluminum are presented in anticipation of the ability to fabricate the heat exchanger out of a more conductive material. The four design variables for the heat exchanger are the water channel width (b), the air channel width (w), the fin width (y), and the fin length (H). An initial set of these four variables is chosen, and the following procedure is used to calculate the heat transfer. The Mathematica computer program used in the optimization is shown in Appendix A. Values of the fluid and material properties are also given in the program. An iterative procedure is used to find the

variable set that maximizes heat transfer/frontal area within the set of specified design constraints (i.e. specified pressure drop of the air and water across the heat exchanger and thickness (L) of the heat exchanger).

Assumptions in optimization

The following five assumptions were used for the geometrical optimization.

1. Macroscale vs. microscale behavior: The modeling that will be described uses macroscale heat transfer assumptions to predict the performance of the heat exchanger. Macroscale analysis treats the fluid as a continuum, an assumption that is true where the length scale is much greater than the mean free path of the fluid particles. The air channel flow should obey the macroscale modeling accurately. Although several researchers [21,22,30-34] have investigated gas microscale effects, the scales in all of these studies were less than 100 μm and in most of these studies the scales were less than 10 μm. Since the smallest scale of the air channels is around 200 μm, the macroscale modeling should be very accurate.

Water channel liquid flow is in the regime that microscale effects just begin to become appreciable. The results for the behavior of fluid flow and heat transfer in microfluidic environments are extremely mixed and inconsistent. A trend for liquids found by examining the research [35-39] as a whole is that the heat transfer is enhanced and the friction factor is decreased compared to the macroscale case. This is very different than conventional behavior where the heat transfer coefficient scales with the friction factor (Colburn analogy). A consistent trend is that transition to turbulence occurs at a lower Reynolds number than macroscale analysis predicts [36-39].

Although microscale phenomena may have a small effect on the water flow in the cross flow micro heat exchanger, the contribution of microscale effects will be neglected in the design because the water convective heat transfer resistance is small and the water pressure drop is not crucial.

2. Fully developed water flow: The water flow through the heat exchanger is assumed fully developed in the calculation of the water pressure drop and the water channel heat transfer coefficient for the optimization analysis. This assumption results in a slightly greater water flow rate and lower heat transfer coefficient. The overall effect of the assumption on the predicted heat transfer is expected to be very small for several reasons. The water is fully developed in the majority of the water channel when the pressure drop constraint is satisfied, the water pressure drop is not a critical parameter (shown later in chapter in Results – Sensitivity) in predicting the heat transfer, and the water convection heat transfer resistance is only a small percentage of the overall heat transfer resistance. A more accurate model is used to predict the water pressure drop in Chapter VI – Testing.

3. Front and rear face heat transfer neglected: Heat transfer on the front and rear faces of the heat exchanger is neglected. Since the contact area associated with the inner walls of the air channels comprise 75% of the total area available for heat transfer (gas side) and the regions on the front and rear faces are at local stagnation points with low convection coefficients, heat transfer on the front and rear faces is expected to be a very small portion of the total heat transfer. The heat transfer is slightly underestimated as a result of this assumption.

4. Three dimensional effects: The water was assumed to be directly adjacent to the air through the thickness of the heat exchanger in the optimization analysis. As shown in Figure IV.4, the water channel walls comprising the front and rear face of the heat exchanger, and not the water channel, are adjacent to the air channel near the inlet and exit. The error is magnified since the convection coefficient is very high near the inlet of the air channel (Figure IV.5). Therefore three-dimensional finite element analysis is necessary to accurately model the heat exchanger. This assumption causes the optimization model to overestimate the heat transfer.

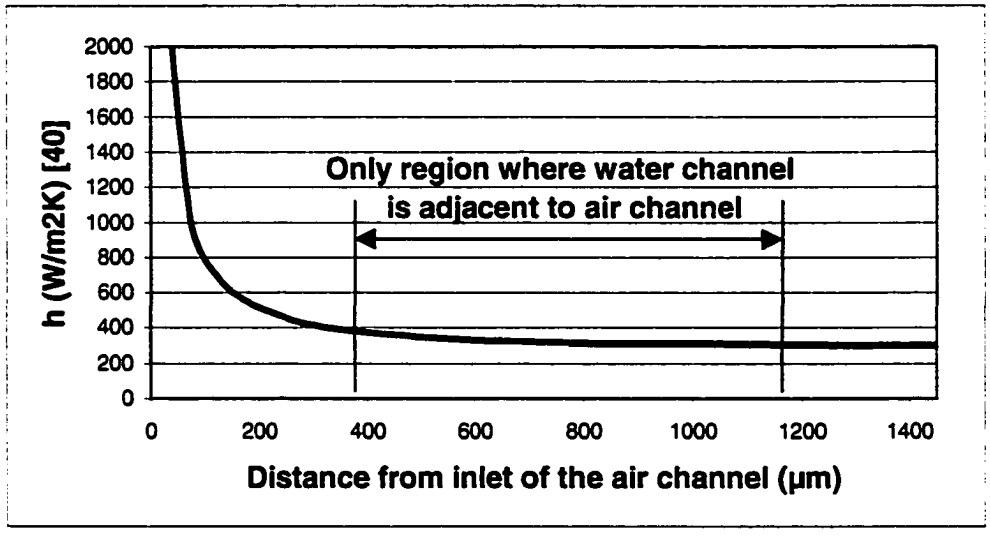

Figure IV.5 – Convection coefficient variation down the length of the air channel

5. Longitudinal air conduction: Conduction in the longitudinal direction of the air channel was assumed negligible compared to convection. For certain micro heat exchangers involving gas flow [20], longitudinal air conduction can be appreciable. This assumption was verified using a method described by Bier et al. [20]. In summary, if the product of the number of heat transfer units (Equation IV.1) and a characteristic number for longitudinal conduction (Equation IV.2) is much less than one, longitudinal conduction in a fluid can be neglected.

$$NTU = \frac{UA_{HT}}{\dot{m}_{air} c_{p\text{-}air}} \quad \text{(IV.1)}$$

$$\Lambda = \frac{k_{air}}{L} \frac{Hw}{\dot{m}_{air} c_{p\text{-}air}} \quad \text{(IV.2)}$$

U is the overall heat transfer coefficient and A_{HT} is the total heat transfer area.

For the optimized plastic heat exchanger (described later), the product of these two numbers was 0.0007 validating this assumption.

Calculations

1. The hydraulic diameter of the air channel, $D_{h\text{-}air}$, is calculated as 4A/P where A is the cross sectional area (w x H) of the air channel and P is the perimeter (2w + 2H).

2. The relation between the pressure drop across the channel and the velocity of air through the channel is given by Equation (IV.3) where the first term on the right hand side is pressure drop caused by viscous drag and the second term is related to inlet and exit losses. The constant K is the minor loss coefficient. Inlet and exit minor loss coefficients were estimated for laminar flow and a ratio of free flow area to total frontal area of 0.25 using correlations for compact heat exchangers. These correlations include the influence of the velocity profile in the channels on the momentum rates and the resulting effect on the change of momentum at the entrance and exit [3]. As a result, the loss coefficients for laminar and turbulent flow vary considerably. The sum of the estimated inlet minor loss coefficient of 1.15 and the estimated exit minor loss coefficient of 0.40 results in an overall estimated value of 1.55 for the minor loss coefficient [3]. If the flow were assumed fully turbulent ($Re \rightarrow \infty$), the inlet and exit loss coefficients would have been 0.55 and 0.37. The value of the non-fully developed friction factor, f, is a function of velocity and geometry and is obtained from curve fit

tabular empirical correlations for non-fully developed flow through rectangular channels [40]. Both the friction factor, f, and the bulk velocity, V, are iteratively calculated using Equation (IV.3) and given values of Δp, L, ρ, and $D_{h\text{-}air}$.

$$\Delta p = \frac{f\rho_{air}V_{air}^2 L}{2D_{h-air}} + K\frac{\rho_{air}V_{air}^2}{2} \qquad \text{(IV.3)}$$

3. The average non-fully developed Nusselt number in the air channels is a function of the dimensionless quantities in Equation (IV.4) and is obtained from a curve fit of tabular empirical correlations [40]. The Nusselt number is required to determine the convection coefficient on the inner walls of the air channel.

$$Nu = \frac{h_{air}D_{h\text{-}air}}{k_{air}} = f\left(\frac{L}{D_{h\text{-}air}\,Re\,Pr}, \frac{w}{H}\right) \qquad \text{(IV.4)}$$

4. The flow within the water channels is considered fully developed and laminar. The convection coefficient governing the thermal resistance between the water and the wall is given by Equation (IV.5) where the hydraulic diameter of the water channel ($D_{h\text{-}water}$) is a function of the water channel width (b) and the water channel depth (about half the heat exchanger thickness).

$$h_{water} = \frac{3.7k_{water}}{D_{h\text{-}water}} \qquad \text{(IV.5)}$$

The appropriate length scale for this correlation derived for circular channels is the hydraulic diameter, $D_{h\text{-}water}$. A typical value of $D_{h\text{-}cool}$ is 583 μm, based on a water channel cross section of 500 μm x 700 μm.

5. The heat transfer to each air channel can now be calculated. Figure IV.6 shows the resistive network between a water channel and an air channel. The dashed line is the

boundary of the unit cell being analyzed. By symmetry, the total heat transfer to the air channel is twice the heat transfer from one water channel to one air channel. R_1 is the convection resistance at the water/wall interface. R_2 is the conduction resistance through the thickness of the wall separating the water and air channels. The assumption of 1-D heat transfer in this wall was investigated using 2-D analysis. The error in calculating the heat transfer using this assumption was only around 3%. R_3 is the effective convection resistance, based on the inner area of the air channel and the difference in temperature between the base of the fin and the local temperature of the air. The values of R_1, R_2, and R_3 are given by Equations (IV.6a), (IV.6b), and (IV.6c).

$$R_1 = \frac{1}{h_{water}(w+y)L} \tag{IV.6a}$$

$$R_2 = \frac{a}{k_{wall}(w+y)L} \tag{IV.6b}$$

$$R_3 = \frac{1}{h_{air}(\eta_f H + w)L} \tag{IV.6c}$$

η_f is the fin efficiency defined by Equation (IV.7).

$$\eta_f = \frac{\tanh\left(\sqrt{\frac{2h_{air}}{yk_{wall}}}\frac{H}{2}\right)}{\sqrt{\frac{2h_{air}}{yk_{wall}}}\frac{H}{2}} \tag{IV.7}$$

The sum of R_1, R_2 and R_3 equals the resistance from one water channel to an air channel. By symmetry, the total heat transfer resistance (R_{tot}) to a single air channel is one half this sum (Equation (IV.8)).

$$R_{tot} = \frac{R_1 + R_2 + R_3}{2} \tag{IV.8}$$

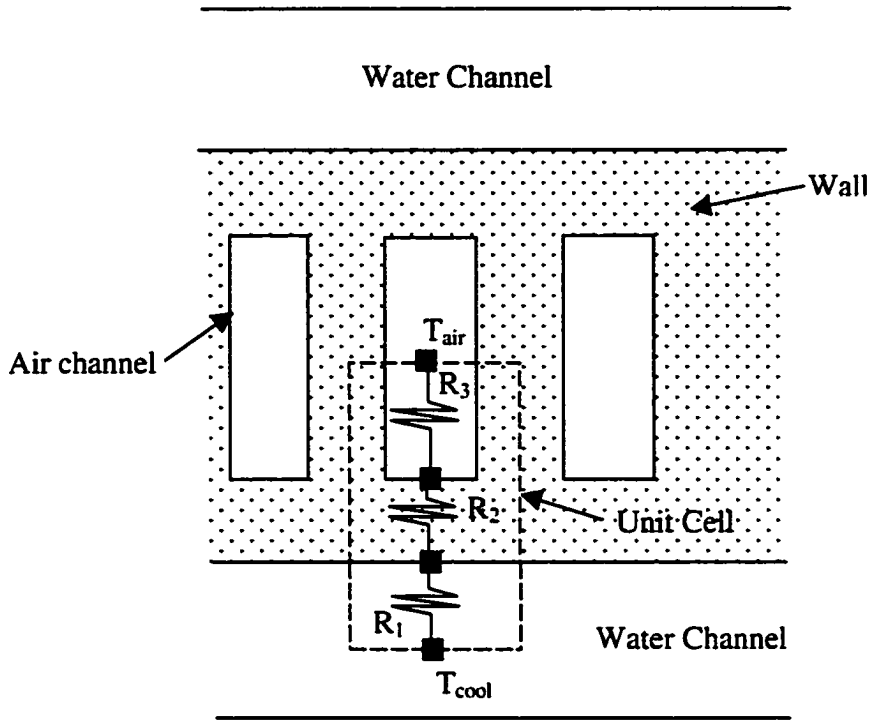

Figure IV.6 – Cross sectional view of heat exchanger -resistance network

Assuming the water temperature is constant and equal to the inlet water temperature, the exit temperature of the air is found by manipulating Equation (IV.9).

$$\frac{T_{water\text{-}inlet} - T_{air\text{-}exit}}{T_{water\text{-}inlet} - T_{air\text{-}inlet}} = \exp\left(-\frac{1}{\dot{m}_{air} c_{p\text{-}air} R_{tot}}\right) \qquad \text{(IV.9)}$$

The mass flow rate of air through the channel is ρ_{air} VwH.

Finally, the heat transfer to a single air channel is given by Equation (IV.10).

$$q_{channel} = \dot{m}_{air} c_{p\text{-}air} (T_{air\text{-}exit} - T_{air\text{-}inlet}) \qquad \text{(IV.10)}$$

The frontal area of the unit cell occupying a single channel has dimensions (b+2a+H)(y+w). An excellent estimation of the total number of air channels (N) in the heat exchanger is obtained by dividing the total frontal area of the heat exchanger (F_w x

F_h) by this unit cell area. The total heat transfer for the heat exchanger is given by Equation (IV.11).

$$q = Nq_{channel} \tag{IV.11}$$

6. The initial assumption that the exit temperature and inlet temperature of the water are equal provides a slightly high estimate of the total heat transfer. The following iterative process converges quickly and greatly reduces the error:

i) The number of water channels is equal to the height of the heat exchanger (F_h) divided by the distance between water channels (b+2a+H). The mean velocity of the water, V_{water}, through the channels for laminar flow is given by Equation (IV.12), where correlations for circular tubes are used and the length scale is the hydraulic diameter of the water channel, $D_{h\text{-}water}$.

$$V_{water} = \sqrt{\frac{2D_{h\text{-}water}\Delta P_{water}}{f\rho_{water}F_w}} \tag{IV.12}$$

The friction factor for laminar fully developed flow is estimated as $64/Re_{water}$.

ii) After calculation of the total number of water channels, the cross section of the water channels, and the mean fluid velocity through the water channels, the mass flow rate of the water through the heat exchanger is determined. Using Equation (IV.13) the exit temperature of the water is calculated.

$$q = \dot{m}_{water}c_{p\text{-}water}(T_{water\text{-}inlet} - T_{water\text{-}exit}) \tag{IV.13}$$

iii)The average value of the water temperature is the average of $T_{water\text{-}inlet}$ and $T_{water\text{-}exit}$. Since the water changes temperature only slightly (about 1°-2°C), this is an accurate estimate of the average water temperature. If greater accuracy is desired, this average value of temperature could be substituted into Equation (IV.9) as the updated value of

T_{water} and repetition of equations (IV.9)-(IV.13) would produce new value of $T_{water\text{-}exit}$. Once the average water temperature is determined, the heat transfer is calculated using Equation (IV.14).

$$q_{final} = q\frac{(T_{water-avg} - T_{air-inlet})}{(T_{water-inlet} - T_{air-inlet})} \qquad \text{(IV.14)}$$

7. Initial estimates of b, w, y, and H as well as the material properties of the heat exchanger and fluids are the inputs required to solve Equations (IV.3)-(IV.14) and calculate the total heat transfer of the heat exchanger. The heat exchanger design is optimized by holding three variables constant while the value of the fourth is varied to maximize heat transfer/frontal area. The fourth variable assumes this new value during the next step in the optimization process where the first, second, and fourth variables are held constant, while the third is varied to find a maximum. This iterative procedure is continued and quickly converges.

8. In the above analysis, the shape of the air channels was rectangles. Other air channel shapes (parabola and trapezoid) were investigated to determine if rectangular air channels optimized heat transfer. Calculations showed rectangular air micro channels are optimum for heat transfer due to the air channel width and fin width constraints. Under these constraints, the different channel shapes result in a reduced number of air channels and for the optimized designs for the different shapes, less open area for air to flow. This results in lower rates of heat transfer for non-rectangular channels.

9. Once the heat exchanger was designed, the overall heat transfer coefficient, U, was calculated using Equation (IV.15).

$$U = \frac{q_{final}}{A_{HT}T_{lm}} \qquad \text{(IV.15)}$$

A_{HT} is the total heat transfer area for both the air and water channels and T_{lm} is the log mean temperature difference between the water and air in the heat exchanger. The overall heat transfer coefficient is a measure of the heat transfer resistance between the fluids.

The volume of the heat exchanger was calculated by multiplying the frontal area of the heat exchanger by the length of the air channels. To determine the mass of the fabricated heat exchanger, an effective volume of heat exchanger material was calculated using the geometry of the unit cell. The effective material volume was multiplied by the density of the heat exchanger material to calculate the mass of the heat exchanger. Since the mass of current innovative dry radiators is typically reported, the mass of the water in the heat exchanger channels was not included in the calculation of the mass of the heat exchanger.

10.A finite element model is utilized to accurately predict the heat transfer due to three-dimensional effects. The unit volume was constructed using the geometry calculated in the optimization. A finite element solution using ANSYS was performed to obtain the solution within the solid to the following steady state three-dimensional heat equation with no heat generation.

$$\frac{\partial^2 T}{\partial x^2}+\frac{\partial^2 T}{\partial y^2}+\frac{\partial^2 T}{\partial z^2}=0 \qquad \text{(IV.16)}$$

The air convection coefficient, obtained from Nusselt number empirical correlations, was varied along the length of the air channel since the air is developing through the channel. The finite element solution with data is outlined in Appendix 2. The solution assumes macroscale fluid behavior and insulated front and rear heat exchanger faces.

IV.5. Results

Optimum Designs

The optimum designs and predicted performance for plastic, ceramic, and aluminum cross flow micro heat exchangers are shown in Table IV.1. The only geometrical difference between the optimized heat exchangers is the height of the air channel. As the thermal conductivity increases, the optimum air channel height (H) increases because the fins conduct heat better. In turn, the heat transfer increases due to a greater open area for air flow, increased fin effectiveness, and lower conduction resistance. A reduced number of air and water channels are additional effects of increasing the air channel height. The air channel width, fin width, and water channel width have the minimum values set by design constraints (w = 200μm, y = 200 μm, b = 500 μm). In other words, smaller dimensions are better. This is the inherent scaling advantage of micro heat exchangers.

Table IV.1 – Optimum designs

Material	k (W/mK)	H (μm)	N_{air}	V_{air} (m/sec)	Re_{air}	m (kg)	U (W/m^2K)	q (W)
Plastic	0.193	750	4300	7.9	155	2.15	126	**49**
Ceramic	3.0	1300	3100	8.5	184	4.94	254	**100**
Aluminum	237	1700	2600	8.7	194	5.06	290	**113**

The air velocities and Reynolds numbers are similar regardless of the heat exchanger material because only the height of the air channel varies. The mass does vary with heat exchanger material due to varying densities (ρ_{PMMA} = 1150 kg/m^3, ρ_{Al} = 2702 kg/m^3). Interestingly, the heat transfer/mass under the same design constraints for heat exchangers made from the three distinctly different materials vary by less than 13%.

Comparing the heat transfer rates of heat exchangers made of different materials, ceramic (k = 3 W/m-K) and aluminum (k = 237 W/m-K) heat exchangers have similar performance. However, the plastic heat exchanger (k = 0.193 W/m-K [41]) has significantly reduced performance. Once the thermal conductivity reaches a moderate value, convection heat transfer resistance dominates and greater performance enhancement can be achieved by relaxing the geometric design constraints (i.e. allowing dimensions (a), (b), and (w) to be smaller) compared to improving the thermal conductivity of the heat exchanger material. Cross flow micro heat exchanger performance will be compared to conventional scale heat exchangers in the performance discussion chapter.

Sensitivities

Sensitivity is defined as the ratio between relative changes of two variables. The sensitivity of heat transfer to a design constraint is a measure of the relative importance of the design constraint to heat transfer. The sensitivities of various design constraints are calculated for the optimized plastic heat exchanger design using the following equation and the optimization analysis equations.

$$S = \frac{\partial q}{\partial x}\frac{x}{q} \tag{IV.17}$$

x is the design constraint for which the sensitivity is determined.

An example of these calculations is shown in Appendix 1. The sensitivities of several design constraints are shown in Table IV.2.

Table IV.2 – Sensitivities

	w	y	a	b	L	p_{air}	p_{water}
Sensitivity (%)	-22	-20	-39	-37	68	15	1

As shown by the highest sensitivity of 68%, increasing the length of the air channel (L) is most important in improving heat transfer. In other words, increasing the length of the heat exchanger by 10% while holding the other geometrical parameters and pressure drops constant, will increase the heat transfer by approximately 6.8%. The longer air channel increases the surface area for heat transfer causing the air to exit the heat exchanger warmer. This heat transfer advantage overrides the fact that the air flow rate decreases with increasing channel length (satisfying the pressure drop constraint) . A disadvantage of increasing the length of the air channel is an increase in the volume and mass of the heat exchanger.

Decreasing the width of the wall separating the water and air (a) is also important in improving heat transfer especially when the heat exchanger is fabricated from a low conductivity plastic. By decreasing the wall width, there is less conduction resistance between the fluids and more space for micro channels. The heat transfer improvement achieved by decreasing the width of the wall between the water and air is shown in Figure IV.7. Additional plots from the optimization analysis are shown in Appendix A. These graphs do not account for three-dimensional effects.

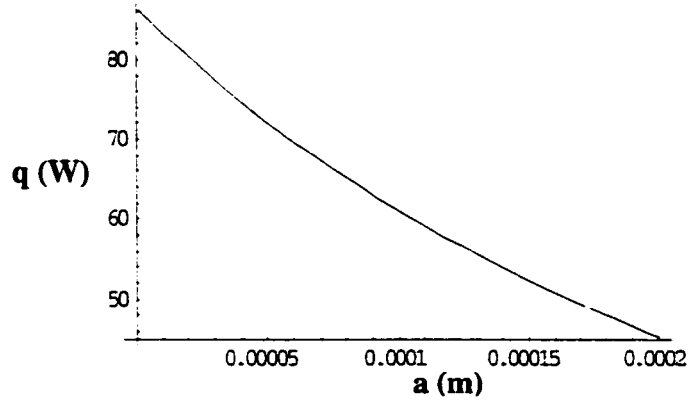

Figure IV.7 -Effect of the plastic fluid separating wall thickness on heat transfer

Another important dimension for heat transfer is the width of the water channel (b). By decreasing this width, the area for air channels is increased thereby increasing the flow rate of the air. The disadvantage of reducing the width of the water channel is a reduced water flow rate that causes a larger water temperature change (i.e. lower average water temperature).

Other less effective methods to increase the heat transfer are to decrease the width of the fin (y), decrease the width of the air channel (w), and increase the allowed pressure drop of the air (p_{air}). As shown by a very low sensitivity, the pressure drop of the water is not an important factor for heat transfer performance. In general, the use of more aggressive design constraints increase the difficulty of fabrication and decrease the strength of the heat exchanger.

It is important to note that the sensitivities given are only valid at the design geometries and pressure drop constraints. An illustrative example is the heat transfer sensitivity to the air channel length for a very thick heat exchanger (i.e. air exits the heat exchanger close to the temperature of the water). In this case, increasing the length of the air channel would decrease the heat transfer because the air flow rate would be reduced to satisfy the pressure drop constraint and the air exit temperature would still be close to the water temperature.

Finite element analysis results

The heat transfer data given in Table IV.1 were obtained using finite element analysis. Figure IV.8 shows the temperature field on a unit cell of the heat exchanger. Air entering the air channel at 25°C is heated by water at 58°C as it traverses the air channel. Darker colors indicate colder temperatures as indicated by the temperature key

given. At the top left of the unit cell, the temperature is the coolest. This is expected since the air has not been heated yet, the convection coefficient is highest near the inlet of the heat exchanger, and the conduction length through the solid to the hot water is greatest. As the air traverses the heat exchanger, the walls become warmer since the air is heated, convection coefficient decreases, and conduction length decreases. Near the exit of the air channel, the walls become slightly cooler due to an increase in the conduction length.

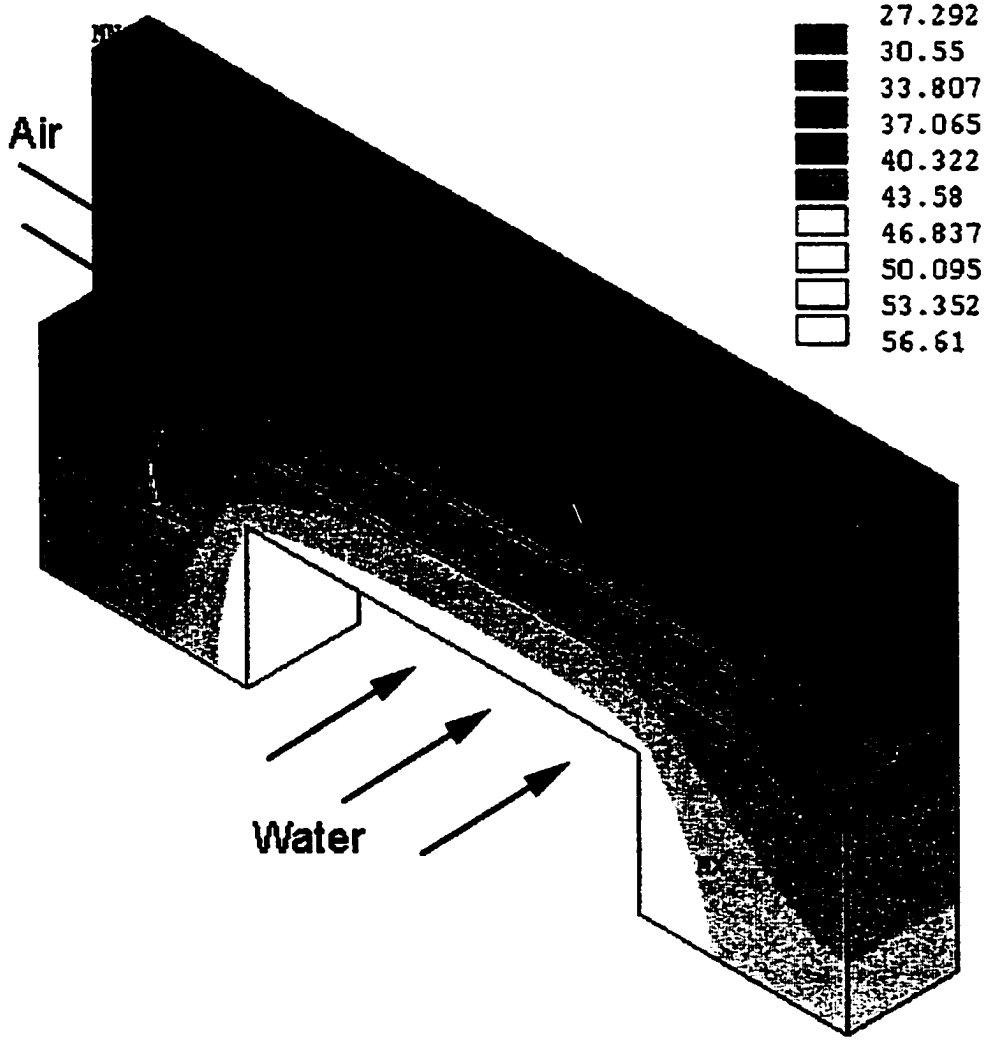

Figure IV.8 - 3-D model of heat exchanger

The result of the finite element solution for the plastic heat exchanger is about a 15% decrease in heat transfer compared to the analytic model used in optimization analysis for the range of air velocities that will be used for testing. Conduction heat transfer resistance diminishes the heat transfer enhancement due to large convection coefficients present in the developing length. For higher thermal conductivity materials, the conduction heat transfer resistance is reduced and the heat transfer approaches the analytic model. This also occurs as the water channel depth approaches the thickness of the heat exchanger (L).

The average temperature at the base of the fin and the bulk air temperature were plotted (Figure IV.9) versus the length down the air channel for the optimization analysis (2-D) as well as the finite element analysis method (3-D). The base of the fin temperature was warmer near the inlet and exit of the air channel for the optimization analysis since the water channel was assumed to be adjacent to the air channel. Warmer temperatures at the base of the fin result in greater heat transfer rates for the analytic model. In the middle of the air channel, the base of the fin is still warmer for the optimization analysis since the air in this region is warmer due to greater heating near the inlet of the channel. For the finite element analysis, the cooler air temperature (i. e. reduced heat transfer rates) is the result of cooler temperatures at the base of the fin.

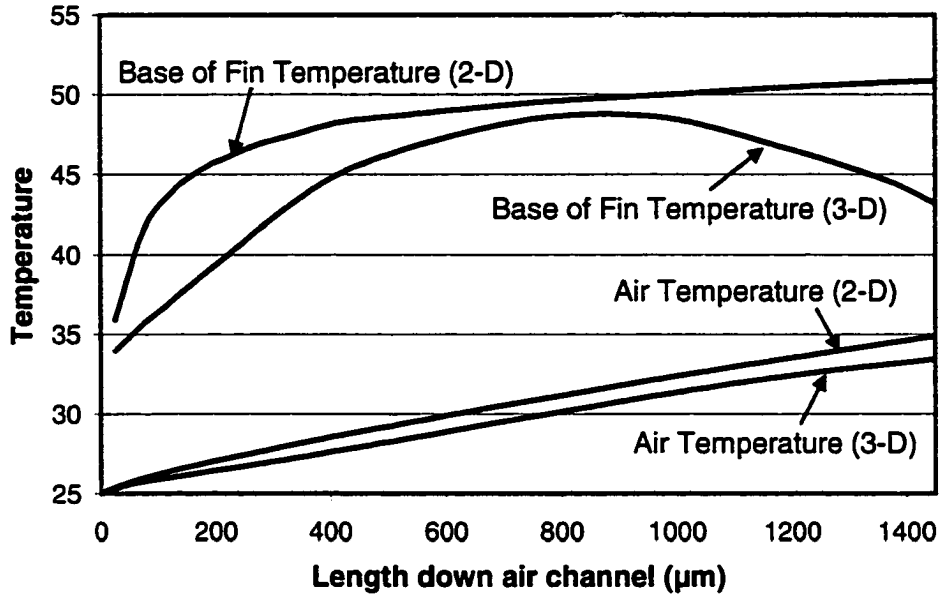

Figure IV.9 - Optimization analysis vs. finite element analysis

CHAPTER V - FABRICATION

The cross flow micro heat exchanger was fabricated using a combination of the LIGA process, conventional machining, alignment, and bonding. Initially, two halves of the heat exchanger are produced by the LIGA process [42]. Conventional machining is then used to open the air channels. Alignment and bonding steps complete the fabrication of the heat exchanger.

V.1. Overview of LIGA Process

LIGA's three processing steps are X-ray LIthography, Galvanoforming (electroplating), and Abforming (molding). A schematic of the LIGA process is shown in Figure V.1.

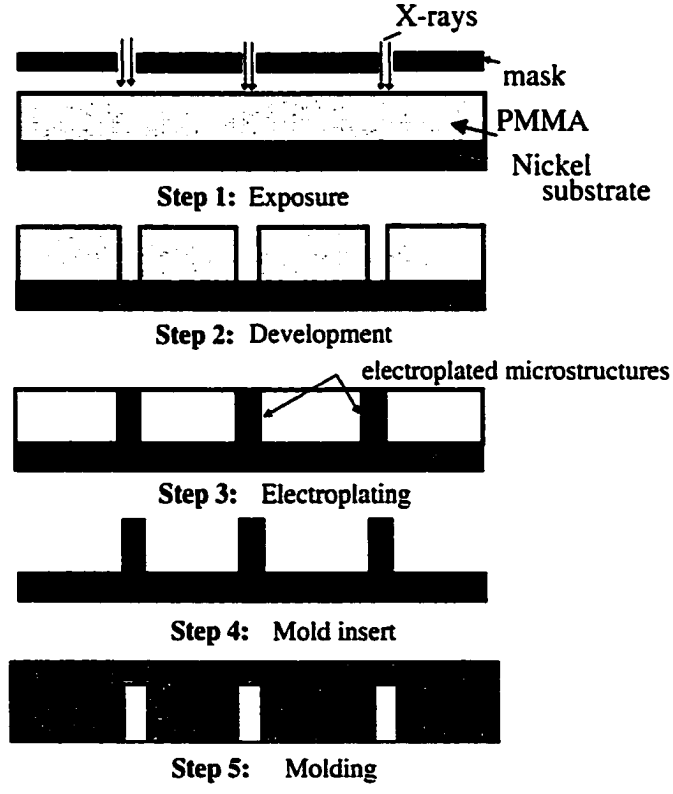

Figure V.1 – Schematic of LIGA process

The LIGA process used to manufacture the heat exchanger begins with the fabrication of an x-ray mask that consists of patterned absorber structures on a substrate transparent to x-rays. The mask is placed between a PMMA covered metal substrate and incoming collimated x-rays. During this step, called exposure (step 1), x-rays break bonds in the molecular chains of PMMA thereby decreasing its molecular weight in regions where the absorber is absent. The PMMA sheet is then placed in a developer solution to remove exposed areas of the PMMA (step 2). Microstructures are electroplated in the voids of the PMMA sheet (step 3). The PMMA is then stripped resulting in a metal substrate covered with microstructures called a mold insert (step 4). Using the mold insert, plastic is molded (step 5) by embossing or injection molding to create plastic parts. This method of fabrication can be used to manufacture microstructures having heights exceeding 1 mm with submicron accuracy [43].

V.2. Procedure

Numerous steps are used to create the final molded heat exchanger pieces. These steps involve alternating tones for the heat exchanger pattern. In order to better explain the fabrication process, the appearance of the air channels for each step will be described (in parenthesis). Note that in the final molded part, the air channels will be troughs (i.e. no plastic). The procedure used to manufacture the cross flow micro heat exchanger will now be discussed.

X-ray mask

Creating an x-ray mask was the first step in the fabrication of the heat exchanger. The plastic design obtained from the optimization procedure was drawn in AutoCad. This drawing was used to create a 2" by 2.6" cross flow micro heat exchanger pattern

with inlet and exit plenums for water flow on an optical mask using a pattern generator. To create the optical mask, the following procedure was followed.

1. Expose thin resist layer on 5" by 5" chrome covered quartz plate to ultraviolet light forming a pattern originating from the AutoCad file.
2. Remove resist in areas exposed to ultraviolet light.
3. Etch chrome in areas resist was removed.

The completed optical mask consists of a chrome absorber pattern to block ultraviolet light on an optically transparent quartz plate substrate. (The chrome absorber is present for the air channels)

Using the optical mask, an x-ray mask was prepared using a gold absorber on graphite membrane x-ray mask. Gold was selected as an absorber due to its high x-ray absorption and ease of electroplating. Graphite was selected as the membrane material due to its low cost, low absorption of x-rays, and mechanical strength. A detailed x-ray mask fabrication procedure is given in Appendix D. A general outline of this procedure is as follows.

1. Polish 125 μm thick graphite substrate.
2. Spin coat 20 μm of SJR 5740 resist on graphite substrate.
3. Bake graphite and resist on hotplate.
4. Expose resist to ultraviolet light through optical mask.
5. Submerse resist in developer solution to remove areas of resist exposed to ultraviolet light. (Air channels have resist)
6. Electroplate 12 μm of gold in areas that resist was removed. (Air channels do not have gold)

7. Dissolve resist.

8. Secure graphite to frame for x-ray exposure.

This x-ray mask combination is similar to that developed at LSU [44, 45] except that SJR 5740 resist was used instead of SU8 resist due to SJR's better adhesion to graphite and more straightforward development and removal. The thickness of the gold absorber was selected to enable exposure of a 1 mm thick sheet of PMMA. A thinner absorber would allow additional radiation to reach areas under the absorber, thereby reducing the dimensional accuracy of the PMMA structures and increasing the taper of the structure walls [46]. A thicker absorber would require a thicker layer of ultraviolet light sensitive resist to be patterned on the graphite substrate possibly reducing the dimensional accuracy of the x-ray mask.

The completed x-ray mask is shown in Figures V.2 and V.3. Figure V.2 shows an overview of the x-ray mask. A paper clip is included to show the small scales of the heat exchanger. Figure V.3 more clearly shows the air channels, water channels, and alignment hole.

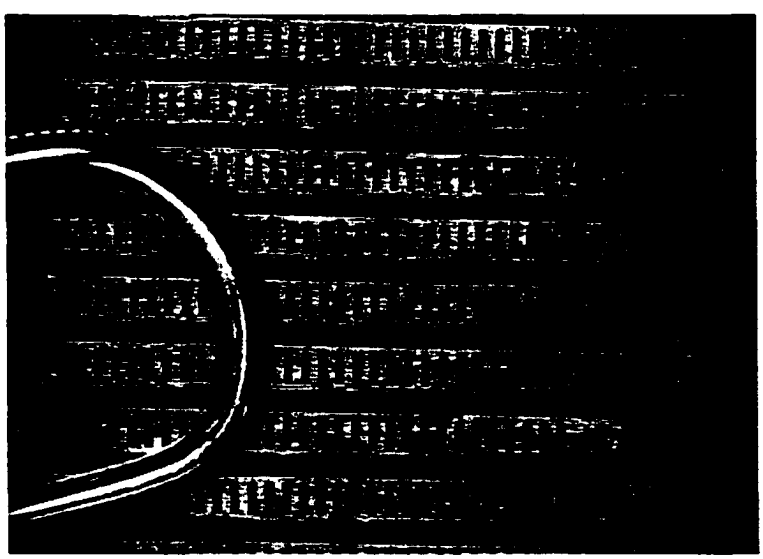

Figure V.2 – X-ray mask (overview)

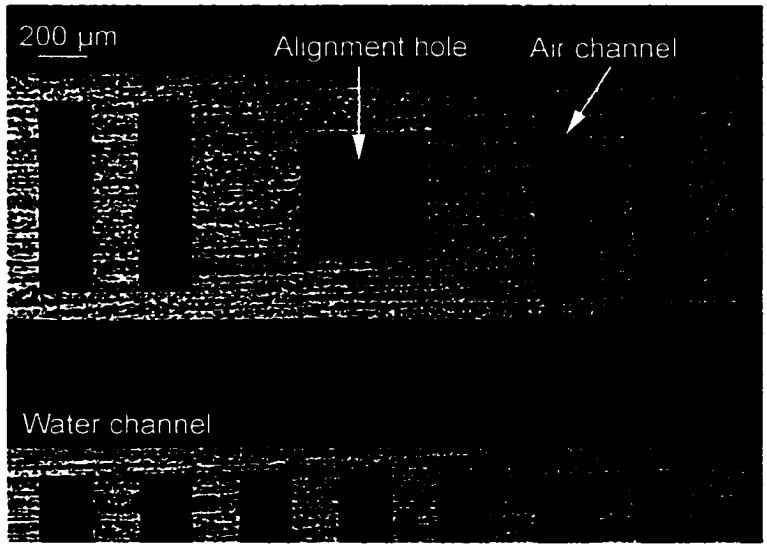

Figure V.3 – X-ray mask (Close up)

Exposure and Development

Before using the x-ray mask to pattern PMMA, the titanium substrate needed to be oxidized and PMMA bonded. A detailed surface preparation and bonding procedure is given in Appendix D. A general outline of this procedure is as follows.

1. Clean titanium substrate using soap and acid etch.
2. Oxidize titanium substrate using an aqueous solution of sodium hydroxide and hydrogen peroxide. The titanium is oxidized to create a thin titanium oxide layer that enhances the bond between PMMA and metal [47,48].
3. Anneal PMMA and slowly cool to remove residual stress [49], reduce absorbed moisture [50], and cause partial crystallization forming nanochannels allowing the escape of gaseous materials during exposure [51].
4. Prepare a methylmethacrylate based bonding solution.
5. Bond annealed PMMA to oxidized titanium substrate using the bonding solution.

The x-ray mask was used to expose (step 1) a 1 mm thick sheet of PMMA bonded to a thick titanium substrate to x-rays. The x-rays, generated at CAMD's synchrotron in

Baton Rouge, had a characteristic energy of 1.5 GeV and critical wavelength of about 3 Å. After exposure, the PMMA covered titanium was immersed in developer solution [52] at room temperature to remove the exposed plastic (step 2). (The PMMA has been dissolved for the air channels) Figure V.4 shows the developed PMMA on a titanium substrate.

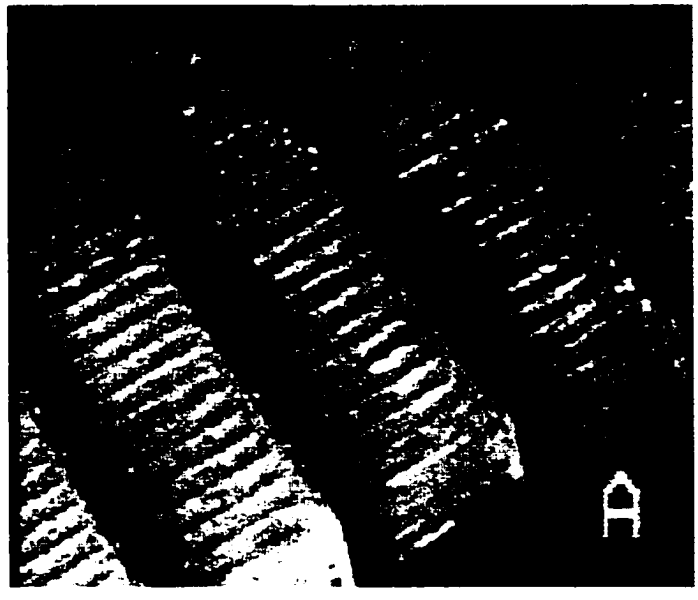

Figure V.4 - Developed PMMA

Electroplating and mold insert

Nickel structures were electroplated (step 3) into the voids using a nickel sulfamate bath. The nickel electroplating occurred at a temperature of 55 °C, pH of 4.0, and current density of 20 mA/cm^2. After the voids were filled, electroplating continued until the overplated area had a thickness of 3 mm. One week was necessary to complete the electroplating. The nickel structures were then mechanically removed from the titanium. The back side of the mold insert was surface ground such that the back side was flat and parallel to the patterned side. A final machining operation was necessary

to complete the mold insert before the PMMA was dissolved. Since the air channels are through holes and the water channels need to be enclosed on the front and back faces of the heat exchanger, the 1000 μm tall nickel structures on the mold insert that correspond to the water channels were milled down by 650 μm. Thus, after molding, the water channels on each half of the heat exchanger will have depth of 350 μm. A jeweler's saw mounted on a milling machine and a magnifying glass were used to perform the machining operation. After machining, the PMMA was dissolved in acetone to complete the mold insert (step 4). (Rectangular nickel structures represent air channels) SEM micrographs of the completed mold insert are shown in Figures V.5 and V.6.

Molding

Each half of the heat exchanger was embossed in PMMA (step 5) using the completed mold insert. A schematic of the embossing step is shown in Figure V.7. In this step, the mold insert is heated then pressed into PMMA to create the heat exchanger

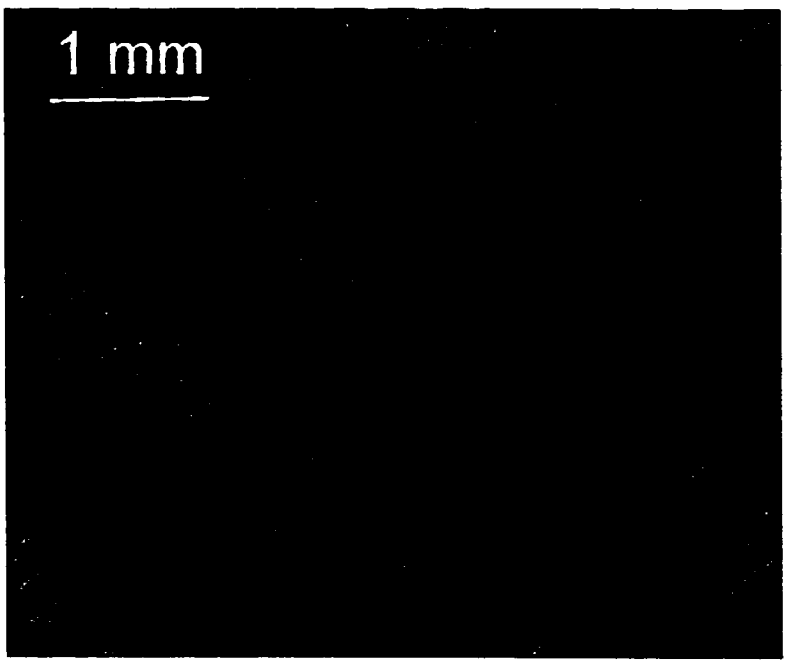

Figure V.5 – Completed nickel mold insert

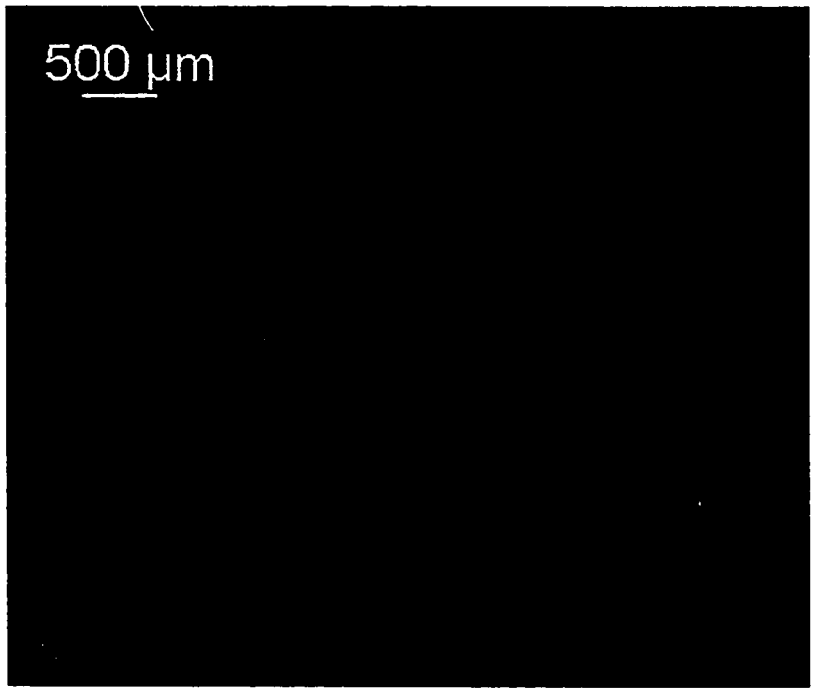

Figure V.6 – Completed nickel mold insert

pattern. (Air channels are troughs in the molded piece) The temperature of the mold insert is important because too high of a temperature will result in degradation of the plastic and too low of a temperature will result in incomplete mold insert filling. After pressing, the PMMA and mold insert are cooled for demolding. The demolding temperature is also important. Demolding at too low of a temperature will cause unnecessary shrinkage in the part requiring very high demolding forces. Demolding at too high of a temperature will distort the part since the plastic will be too weak to withstand demolding forces. SEM micrographs of the embossed piece are shown in Figures V.8 and V.9.

Another viable method that could have been used to mold the PMMA heat exchanger using the existing mold insert is injection molding [53]. This method is favorable for mass production, however embossing provides a reduced probability of mold insert

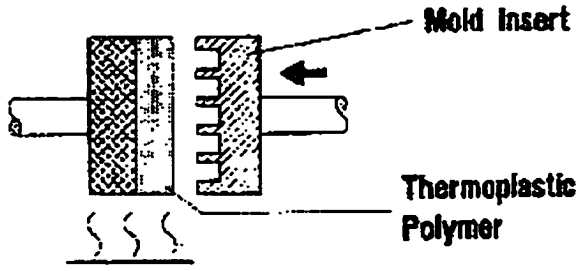

Figure V.7 – Schematic of embossing step

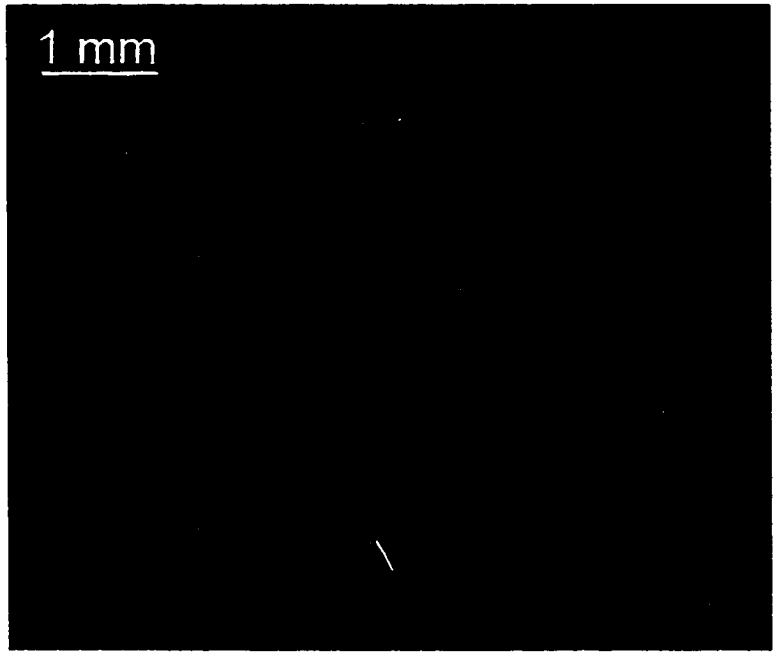

Figures V.8 - Embossed heat exchanger (Overview)

damage, better feature detail, less deformation during molding, and lower thermal shrinkage for the molding of micro parts [54].

Although the performance of the heat exchanger would be improved if the material was ceramic or aluminum, current capabilities restricted the heat exchanger material to PMMA. The option of embossing the heat exchanger into copper or aluminum by pressing the mold insert into heat softened metal was pursued, however satisfactory transfer of the mold insert pattern to metal was unattainable. Options such as ceramic

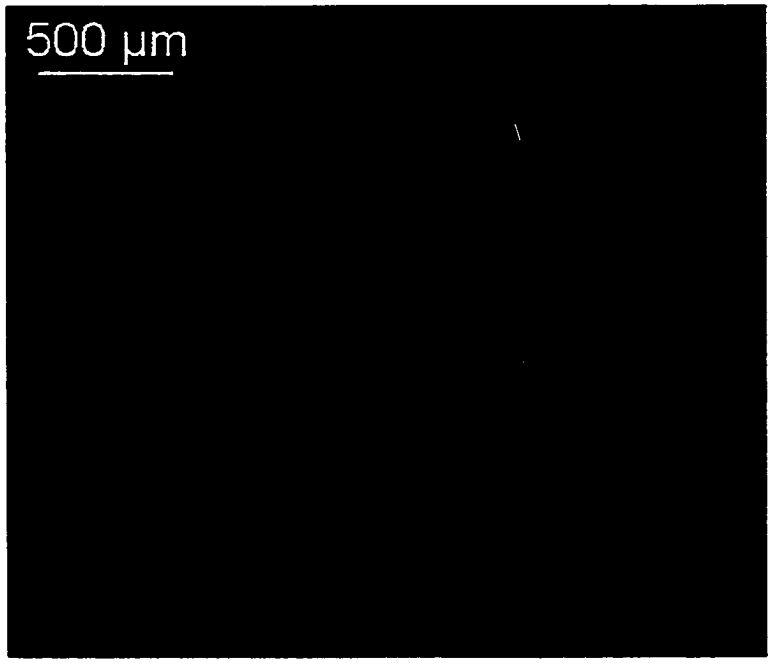

Figures V.9 - Embossed heat exchanger (Close up)

molding, metal injection molding, and infiltration of plastic with more thermally conductive materials are fabrication possibilities that can utilize the LIGA technique to improve the performance of the heat exchanger. Ideally, the heat exchanger would be fabricated using metal injection molding. This relatively new method can produce a high volume of complex ferrous parts. A micro heat exchanger fabricated using metal injection molding can have very high thermal conductivity and bonding could be performed during the sintering step of the process. Initial development of micro metal injection molding has already demonstrated fabrication capabilities of 260 µm lateral width with an aspect ratio of 5 [55].

There are methods other than LIGA that could be used to produce the cross flow micro heat exchanger. One current fabrication option that would create a heat exchanger with better thermal properties is etching. Using wet or dry etching [41], through air channels and water channel troughs could be produced in silicon, however it

would not be feasible to mass produce the heat exchanger using etching methods due the cost involved in deep etching vertical sidewalls. A silicon heat exchanger would also be brittle. An important advantage to the LIGA process is that once the mold insert is manufactured, parts can be molded quickly and inexpensively.

Post molding operations

Additional steps were necessary to prepare the molded piece for alignment and bonding. First, the back side of the embossed piece was fly cut and polished using 400 grit sandpaper to open the air channels. Using accurate lapping and polishing equipment, this step can be performed with polished thickness control to ±2 μm [56]. The back side of the plenums were not fly cut to allow sufficient thickness for the inlet and exit tubing. On one of the two pieces that will comprise the heat exchanger, two holes were milled in each the inlet and exit plenum to allow for tubing connections. Two holes were used to increase the water flow area into the plenums and to produce a more uniform water flow rate distribution across the water channels. On the same piece, pressure taps were machined for measurement of the water pressure drop across the heat exchanger.

Bonding and alignment

Requirements for bonding the heat exchanger are distinctly different than typical requirements for bonding other micro fluidic devices. Since the pieces need to be aligned after the adhesive is applied, an adhesive worklife of at least 5 minutes is required. Another unique characteristic of the heat exchanger is bonding two porous surfaces. This makes it difficult to apply a uniform thin layer of adhesive on either side.

Common bonding methods [57,58] such as solvent bonding using a spinner to create the thin uniform layer of solvent will fail for both these reasons.

Several options of varying complexity exist for bonding PMMA. The simplest methods are solvent and adhesive bonding. In solvent bonding, plastic is covered with solvent then the parts are pressed together. The plastic molecules intertwine and the solvent evaporates creating a bond close to the strength of the bulk plastic. Disadvantages of solvent bonding related to use with the micro heat exchanger include cracking due to stress crazing, short worklife due to solvent evaporation, and sensitivity to bonding pressure (distortion can occur) [59]. In adhesive bonding, the adhesive itself forms the bond between the two surfaces. A long worklife and a bond strength greater than the parent material are possible with adhesives [60]. If an ultraviolet light sensitive adhesive is used, the worklife can be extended almost indefinitely. The primary disadvantage of adhesive bonding is the presence of a bondline. More complicated bonding methods include induction, fusion, ultrasonic, and vibration bonding [61] but their complexity and high equipment costs render them impractical for use in the heat exchanger bonding step. A final method for bonding PMMA is heat bonding. The disadvantage of this technique is either low bond strength or distortion. If the pieces are heated sufficiently to achieve excellent bond strength, some degree of distortion will usually occur.

Several bonding techniques were experimentally investigated to bond the sides of the heat exchanger. The bonding methods investigated were adhesive bonding with a urethane adhesive, strong spray adhesive, mist spray adhesive, ultraviolet glue, acrylic adhesive, and heat sensitive glue, solvent bonding with methylmethacrylate bonding

solution and acetone, and bonding using heat only. Each technique was qualitatively evaluated on bond strength, ability to apply a thin uniform layer (uniformity), presence of a bondline, worklife, ease of use, clogging of the channels, deformation of plastic, transparency, and high temperature resistance. The results are shown in Table V.1. Using these criteria, the best technique was clearly the urethane adhesive.

Table V.1 – Qualitative comparison of bonding methods (1 = Worst, 5 = Best)

Bonding Technique	Bond Strength	Uniformity	Presence of a Bondline	Worklife	Ease of Use
Urethane Adhesive	**4**	**4**	**2**	**4**	**4**
Strong Spray Adhesive	5	2	1	3	4
Mist Spray Adhesive	3	5	3	1	4
Ultraviolet Glue	2	2	2	5	1
Acrylic Adhesive	3	3	2	4	3
Heat Sensitive Glue	2	3	4	5	1
MMA Bonding Solution	4	2	4	2	2
Acetone	1	2	5	1	5
Heat Only	3	5	5	5	4

Bonding Technique	Clogging of Channels	Deformation Due to Glue	Trans-parency	High Temp. Resistance
Urethane Adhesive	**4**	**5**	**3**	**4**
Strong Spray Adhesive	2	5	1	3
Mist Spray Adhesive	4	5	5	3
Ultraviolet Glue	4	4	4	5
Acrylic Adhesive	4	4	4	5
Heat Sensitive Glue	5	3	5	2
MMA Bonding Solution	5	2	5	5
Acetone	5	2	5	5
Heat Only	4	1	5	5

Three urethane adhesives were qualitatively tested. The two part Durabond M-06FL medium viscosity urethane adhesive manufactured by Loctite was selected primarily due to its higher PMMA bonding strength than the other urethane adhesives tested. The Durabond M-06FL is designed for highly flexible bondlines with high peal strength and high shear strength. This adhesive can be spun onto a silicon wafer to provide a layer

that will not clog the channels, will not deform the plastic, and has a sufficiently long setting of 5 minutes. Urethane adhesives are known for excellent sealing and bonding with acrylics [62]. Using Loctite's strength data (tensile strength = 1,300 psi, shear strength = 1000 psi) for the M-06FL urethane adhesive, less than a 5 μm width bond is necessary to constrain water at a pressure of 5 kPa [63]. Since the width of the bond is designed to be between 100 μm and 125 μm depending on alignment, the strength of the adhesive is far greater than required.

The fabricated halves of the heat exchanger were prepared for bonding by thoroughly cleaning the bonding surfaces in soap and water, followed by drying and flattening in an oven at 93°C. Urethane adhesive was then mixed and a nickel-sized portion was applied to a silicon wafer. The wafer was spun at 3800 RPM to achieve a thin coating. One of the sides of the heat exchanger was pressed on the urethane covered silicon wafer and removed to coat the sample. Clamps were utilized to ensure the pressed heat exchanger did not shift on the silicon wafer. Shifting may cause an unnecessary adhesive layer on the sidewalls of the heat exchanger. Figure V.10 and V.11 show the embossed piece after the adhesive has been applied.

A smooth adhesive coating with a thickness generally between 10 and 20 μm results. There is a glue thickness profile across the heat exchanger since the thickness of the viscous adhesive is a function of the distance from the axis of rotation during spinning. A peak is observed near the axis of rotation, however the peak area is small (less than 2 mm in diameter) with respect to the overall size of the heat exchanger (50 mm by 50 mm). Even though at the peak, the thickness of the adhesive layer was 75 μm, the thickness of the glue layer was greater than 30 μm for an area smaller than 0.5 mm in

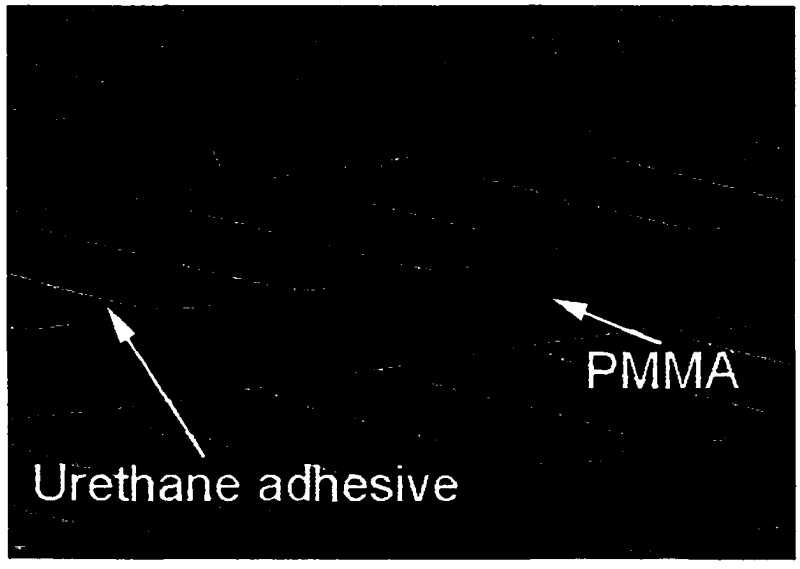

Figure V.10 – Urethane covered embossed heat exchanger (overview)

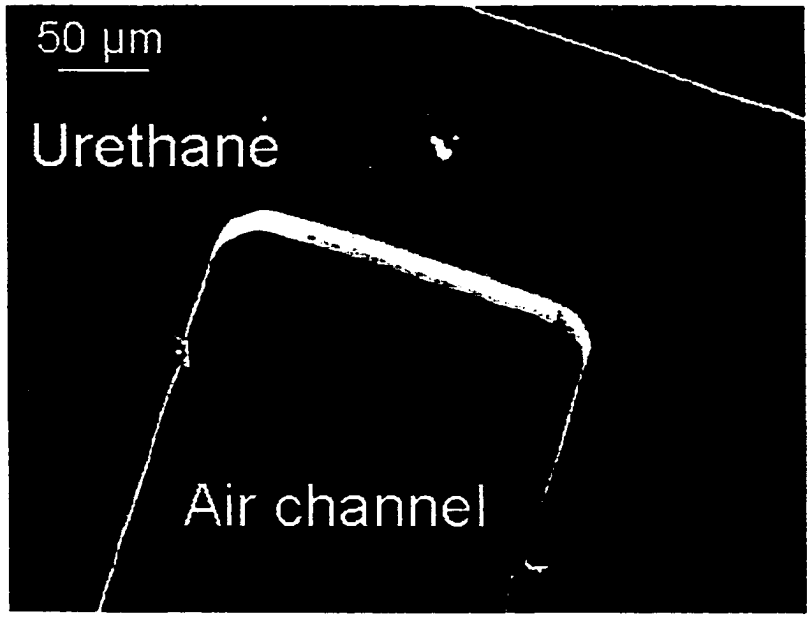

Figure V.11 – Urethane covered embossed heat exchanger (close up)

diameter. Slight channel clogging may occur in this area. The clogging is not expected to appreciably affect performance due to the small area involved. Although accurate spraying of adhesive across the heat exchanger to create more uniform thin layer is an alternative to the spin coating technique, the equipment necessary to use this technique

is very costly and the adhesive will likely be sprayed in undesirable areas such as plenums and air channels.

After adhesive application, the pieces were aligned using nine 500 μm-diameter alignment holes and 0.5 mm pencil lead as alignment pins. Advantages of using pencil lead as alignment pins include the ability to quickly polish the lead to the desired size and easily trim off the excess lead between the assembly and bonding steps. After alignment, the sides of the exchanger were pushed together and the excess lead was trimmed. A pneumatic press was used to press the pieces together at 40 psi for 24 hours. Pictures of the fabricated heat exchanger are shown in Figure V.12-V.14. Figure V.12 shows an overview of the heat exchanger, Figure V.13 shows the alignment and polishing of the air channels, and Figure V.14 shows the alignment and bonding of the water channels. Alignment of better than 30 μm is observed throughout the entire heat exchanger.

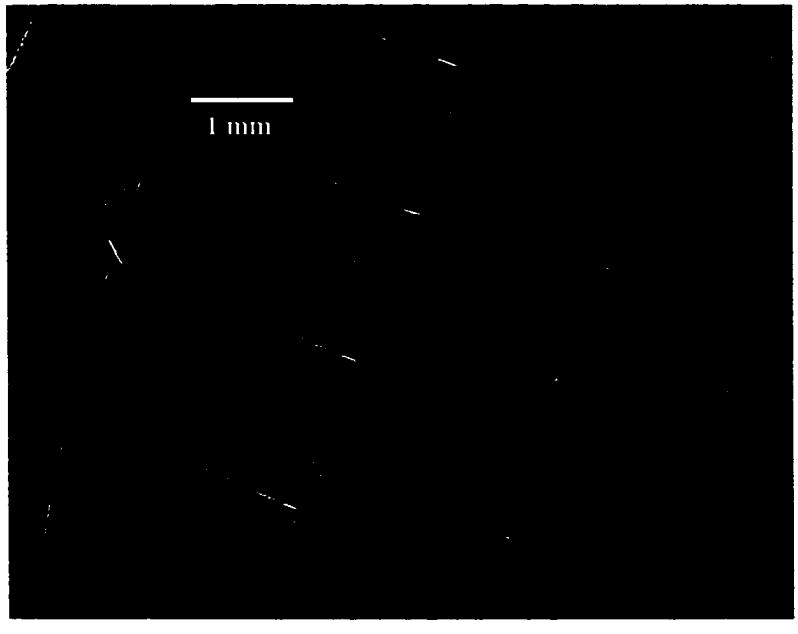

Figure V.12 – Assembled plastic heat exchanger (overview)

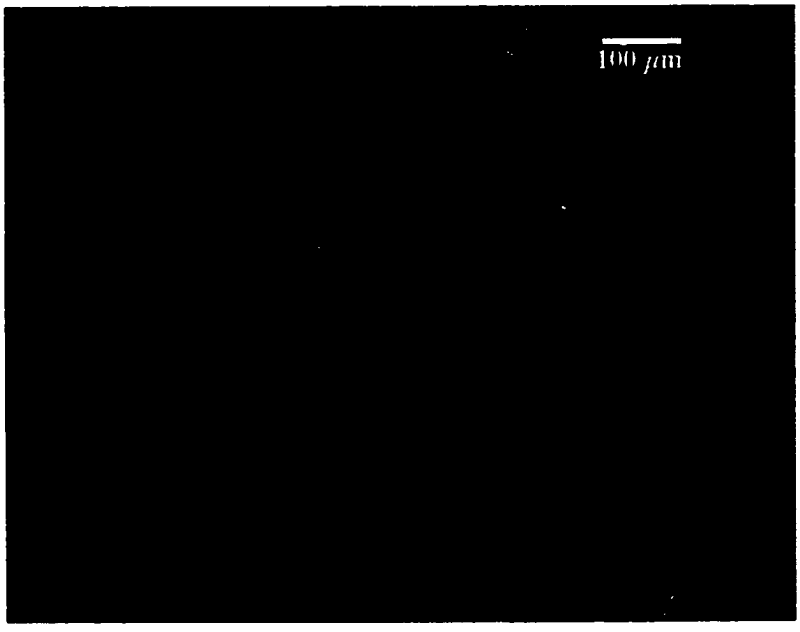

Figure V.13 – Assembled plastic heat exchanger (air channels)

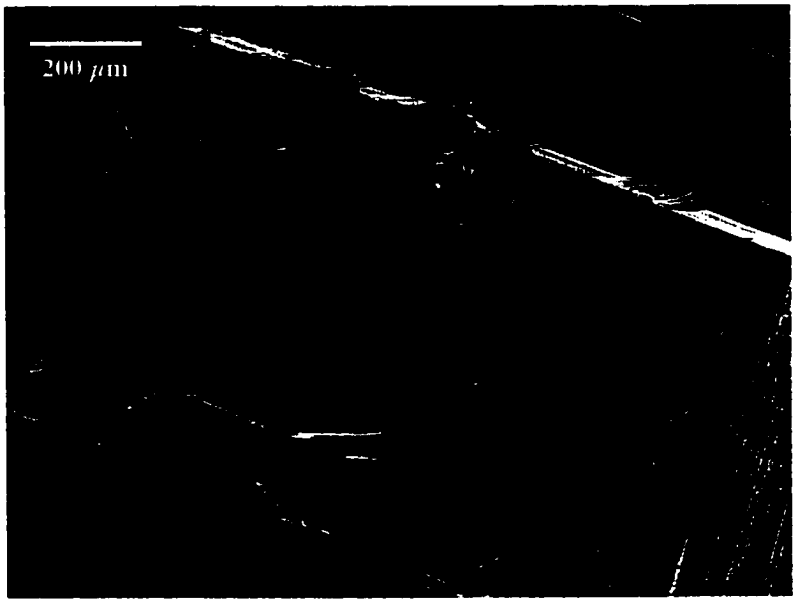

Figure V.14 – Assembled plastic heat exchanger (water channels)

Although more accurate methods of alignment are available, the alignment achieved using lead and alignment holes for prototype development was satisfactory. For larger scale manufacturing, a more complicated alignment schemes for accurate alignment may be valuable. One method to improve the alignment tolerance is to use different

mold inserts to mold the each half of the heat exchanger such that one molded piece will have alignment holes and the other molded piece will have alignment posts. When bonded, the holes and posts will mate thereby aligning the halves very accurately. Fischer et al. [55] has achieved submicron alignment using a similar method. With greater alignment accuracy, the thickness of the wall separating the fluids (a) can be reduced enhancing heat transfer performance. The increased difficulty in fabrication for this alignment method comes from the manufacture of an additional mold insert.

The final step in the fabrication of the plastic cross flow micro heat exchanger was to bond polyethylene tubing using epoxy in the two milled holes at the inlet and exit plenums. A Y-connector was used to combine the two inlet and two exit tubes respectively.

Stacking

Numerous heat exchangers can be stacked to produce a counter flow micro heat exchanger. Figure V.15 shows two plastic cross flow micro heat exchangers stacked and bonded to create a counter flow micro heat exchanger. To fabricate this heat exchanger, the molded pieces that comprise the middle of the heat exchanger were fly cut over their entire area and the backing to the plenums was removed. The top and bottom pairs of heat exchanger molded and fly cut pieces were aligned and bonded using the method previously described. Then the top and bottom pairs were aligned and bonded to complete the counter flow heat exchanger. By stacking multiple heat exchanger layers, the thickness of the heat exchanger is almost unlimited. Flowing the fluids in a counter flow orientation increases the mean temperature difference between

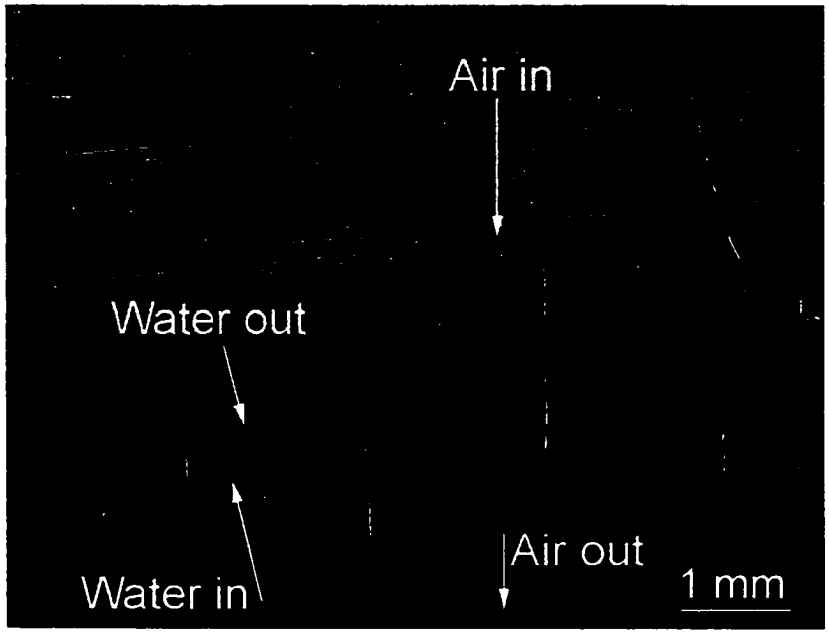

Figure V.15 – Stacked plastic heat exchanger

the fluids. The stacking technique combined with the counter flow design results in increased heat transfer rates under given pressure drop constraints.

V.3. Results

Water was pumped through the fabricated plastic cross flow micro heat exchanger. Sealing between the water and air was achieved over the entire heat exchanger area. Measurements of geometrical parameters of the heat exchanger were taken using an optical microscope coupled with a displacement measurement system. Statistical data of the measurements are summarized in Table V.2. The top of the molded piece measurements refer to the geometrical dimensions near the center of the bonded heat exchanger. The polished face measurements refer to the geometrical dimensions at the air inlet and exit of the heat exchanger.

The mean of the polished face and top of the molded piece dimensions vary by 3-9 μm due to imperfect x-ray beam collimation in the x-ray exposure step of LIGA and the

Table V.2 – Measurements (in μm) of fabricated heat exchanger

	Mean	Standard Deviation	Design
Air channel width (w) - polished face	189.9	5.1	200
- top of molded piece	198.6	2.7	
Fin width (y) - polished face	208.4	4.1	200
- top of molded piece	201.0	3.3	
Air channel height (H) - polished face	745.6	4.4	750
- top of molded piece	748.4	3.0	
Water channel width (b)	498.2	3.7	500
Water channel depth	709.2	52.9	
Heat exchanger thickness (L)	1443	26	
Width of separating wall (a)	126.1	2.8	125
Misalignment	17.3	6.9	

polishing that opened the air channels after fly cutting. Typically, imperfect x-ray collimation results in around 1 μm of taper over a 1 mm structure. Since there are two sides that comprise each measurement, about 2 μm of the difference is likely due to the x-ray exposure step. The polishing step creates a small lip that protrudes over the open areas. If x-ray exposure is assumed to account for 2 μm of the difference in dimensions between the polished face and the top of the molded piece, then the measurements indicate that the polishing step causes the remaining 1-7 μm of difference. Therefore an average lip size of 0.5-3.5 μm is expected. Since these values are small compared to the overall geometrical dimensions, the heat exchanger performance is affected only slightly. Additional polishing with extra high grit sandpaper or briefly exposing the heat exchanger to solvent fumes could be used to reduce the size of the lip.

The dimensions (H, w, y, a, b) that were determined by the conventional LIGA process were within 2 μm of the design values. Typically, the geometrical values for the troughs or holes in the molded plastic parts were slightly less than the design and the geometrical values for the molded plastic walls were slightly greater than the design.

The conventional machining processes performed during fabrication were not as accurate as the LIGA technique. Reducing the height of the water micro channels on the mold insert using the jewelers saw resulted in a large standard deviation for the water channel depth. Post molding fly cutting and polishing to open the air channels removed 250-300 μm of heat exchanger pattern from the molded pieces. The resulting thickness of the water channel wall comprising the front and rear faces of the heat exchanger was around 375 μm. Although not perfect, the alignment of the heat exchanger halves was more than sufficient for sealing. Misalignment was likely due to overpolishing of the lead alignment rods and non-perfect symmetry of the bonded heat exchanger pieces. The lead was slightly overpolished to reduce the likelihood of damaging the alignment hole walls and to allow for quick assembly since the adhesive setting time was only 5 minutes.

CHAPTER VI – TESTING

VI.1. Apparatus

A testing apparatus was designed and fabricated to measure the performance of cross flow micro heat exchangers. Important measurements were the inlet and exit temperatures, pressure drops, and flow rates of the air and water. Overall and detailed views of the testing device are shown in Figure VI.1.

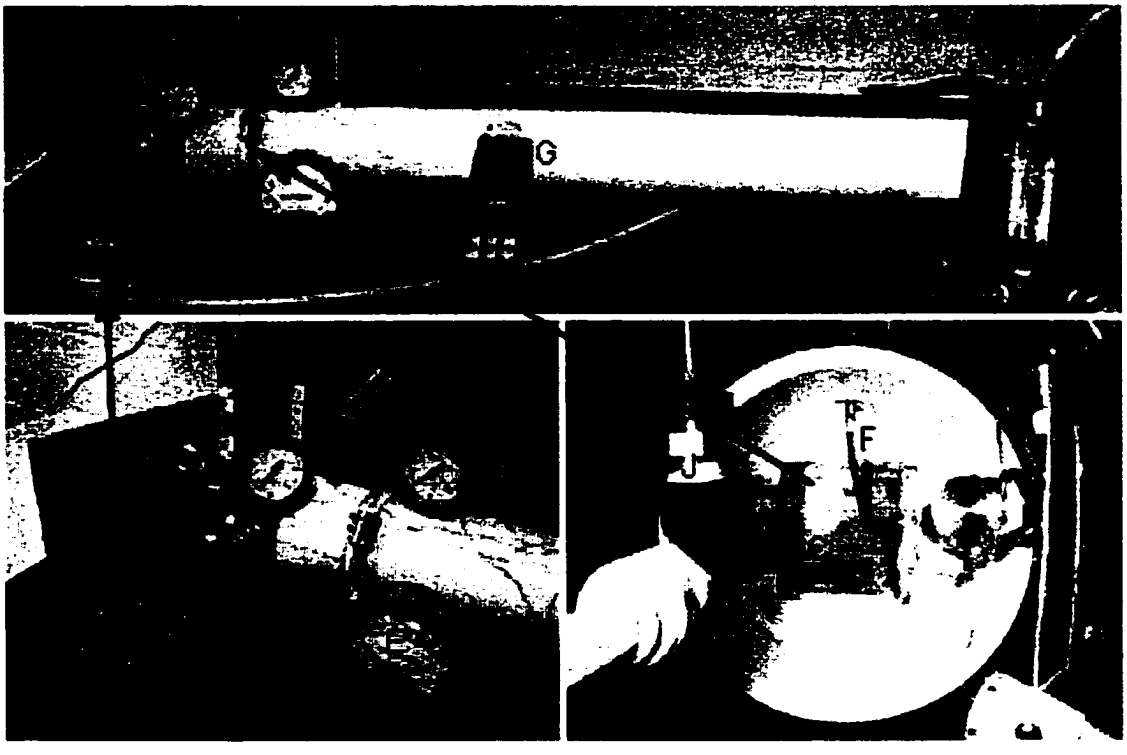

Figure VI.1 - Testing apparatus

Air

A pressurized air line supplies the testing apparatus with air at room temperature (about 25°C). The flow rate of the air through the heat exchanger is adjusted using a ball valve and pressure regulator (not shown). A filter (not shown) is used to remove moisture and contaminants from the air. The air passes through a flow meter (A) and into a four foot long tube with an inner diameter of four inches. A pressure gage (B) is

used near the flow meter to ensure the pressure is near atmospheric. As the air nears the heat exchanger (C), a thermocouple (D) is used to measure the inlet air temperature. The temperature of the air is expected to change only slightly (<0.05°C) between the thermocouple and heat exchanger due to flow acceleration. A low pressure gage (E) is located prior to the heat exchanger to measure the air pressure drop. After the air passes through the heat exchanger, another thermocouple (F) is used to measure the exit air temperature. A three inch long section of four inch inner diameter tubing is used to separate the warm air exiting the heat exchanger from cooler atmospheric air to enable accurate exit air temperature measurement. All of the readings from the thermocouples are obtained using a temperature reader (G).

Water

A pressurized water line supplies the testing apparatus with water. The water is heated to 58°C using a water heater. This is the highest water temperature the water heater can provide. The flow rate of the water is again adjusted using a ball valve and pressure regulator (not shown). A filter is used to remove contaminants from the water. The water flow rate is measured by a water flow meter (H) and the inlet temperature is measured by a thermocouple (I). After the water traverses through the heat exchanger (C), the exit water temperature is measured by another thermocouple (J). A pressure transducer (not shown) is used to measure the pressure drop in the water channel.

VI.2. Procedure

Measurement verification

The flow meters, pressure transducer, pressure gage, and thermocouples were tested to verify their measurements. The water flow meter was tested by capturing water

exiting the flow meter for a given amount of time. Two different beakers were used to measure the flow and the results were identical. The flow rates determined using the water flow meter and the timed beaker method did not agree. Calibration of the water flow meter was necessary. As shown in Figure VI.2, the flow meter readings are consistently a factor of 1.15 smaller than the actual flow rates. For the testing results, the values obtained from the water flow meter were corrected by multiplying the water flow meter reading by 1.154.

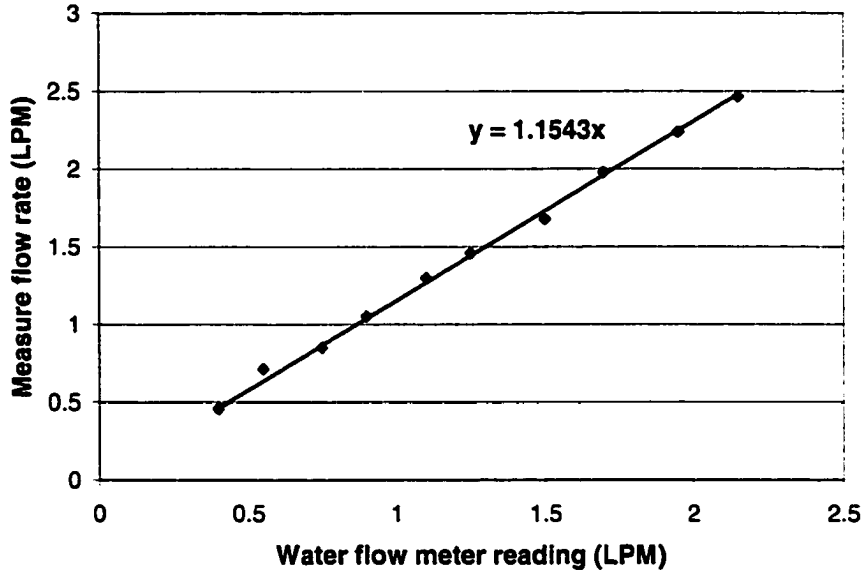

Figure VI.2 – Water flow meter calibration curve

The accuracy of the air flow meter was investigated using a different air flow meter produced by a different company for a different measurement range. The readings between the two air flow meters were the same for the measurement range that they overlapped thus the air flow meter measurements were assumed accurate.

The water pressure drop transducer and air pressure gage were tested using a transducer and pressure gage with different measuring pressure ranges. The readings

between the transducers and gages were the same thus the transducers and gages were assumed accurate.

A thermometer was used to test the thermocouples. The thermocouple and thermometer read the same temperature in atmospheric air and hot water within the accuracy of the thermometer. Thermocouple temperature readings varied by up to 0.2°C. Generally, the variations were the same for atmospheric air and hot water temperature measurements. At the beginning of each testing session, the variations at room temperature were noted. For the testing results, the temperature measurements were corrected for the differences.

Exit air temperature thermocouple placement

Before the tests were run, exit air temperature measurements at constant moderate fluid flow rates were measured at various air channel locations on the heat exchanger. The thermocouple used to measure the exit air temperature was placed close (about 1 mm) to the back side of the heat exchanger to minimize the effect of room temperature air arriving at the thermocouple. Measurements taken at different areas resulted in slightly different exit air temperatures. The air temperatures deviated up to about 0.3 °C from the average temperature due to the water temperature variation across the heat exchanger, slightly different air channel lengths due to polishing, and slightly different coolant channel depths due to insert machining. For the remainder of testing, the thermocouple was placed in a region where an average exit air temperature was observed. The thermocouple was typically located near the center of the heat exchanger.

Heat transfer and pressure drop measurements

The flow rate of air was varied within the accurate limits of the instruments to provide plots of pressure drop and air temperature change as a function of flow velocity through the air channels. Since a change in water flow rate would result in only a small change in heat transfer, the water flow rate was held constant for comparison of heat transfer for a variety of air flow rates. For all heat transfer testing, the water flow rate was 0.6 lpm.

Initially, low air flow rates were used and the heat transfer was allowed to reach steady state. Steady state was defined by the exit temperature of the air changing by at most 0.1°C in a one minute time span. When steady state was achieved, all four temperatures were recorded as well as the fluid flow rates and pressure drop of the air. The flow rate was then increased slightly and measurements were again recorded when steady state heat transfer was achieved. Typically, steady state was achieved in a couple of minutes due to the small change in flow rate. This process was continued until the air flow rate was too high for an accurate measurement. Even at this flow rate, the pressure at the air flow meter was small (<0.5 psi). If the pressure were larger, the air flow meter measurements would need to have been corrected since the air flow meter is designed to measure air at atmospheric pressure. The air flow rate was then significantly reduced and steady state measurements were taken to verify earlier measurements.

Air pressure drop measurements were also taken without a heat exchanger to determine the pressure drop due to flow through the tube downstream of the air pressure gage. This pressure drop was negligible at the flow rates used for testing.

Water pressure drop

The pressure drop of the water was measured at a separate time than the heat transfer and air pressure drop. For water pressure drop measurements, the objective was to determine the pressure drop in the channels only. To determine the water channel pressure drop the following procedure was followed.

1. After heat transfer and air pressure drop measurements were complete, one of the plenums was removed. To remove the plenum, a razor blade was used to scribe a trough in both sides of the heat exchanger. The plenum was then broken off at the scribed trough. The ends of the water channels were investigated to ensure that they were clean.
2. Using a gage pressure transducer located in the remaining plenum, the water pressure drop through the heat exchanger was measured for a variety of flow rates.
3. The remaining plenum was then removed. This plenum provides very short channels (<1 mm) to investigate the pressure drop due to inlet and exit effects as well as the flow in the plenum.
4. Using the same gage pressure transducer, the pressure drop of the water across the plenum and very short channels was measured for a variety of water flow rates.
5. The water channel pressure drops were calculated by subtracting the step 4 pressure drops from the step 2 pressure drops.

VI.3. Uncertainty Analysis

An uncertainty analysis was performed to quantify the accuracy and data validity of the testing results. The detailed uncertainty analysis is given in Appendix C. The outcome of the uncertainty analysis of the experimental data results is summarized in Table VI.1.

Table VI.1 – Uncertainty of experimental data results

	P_{air}	P_{water}	V_{air}	Re_{water}	$\%\Delta T_{air}$	ΔT_{water}	q
Uncertainty (±%)	4	1	3	6	3	15	4

All of the uncertainties are less than 6% at the design conditions except the uncertainty of the water temperature across the heat exchanger (ΔT_{water}). The cause of the high uncertainty of ΔT_{water} is the absolute temperature uncertainty caused by the water heat losses between the thermocouples and the inlet and exit of the water channels is significant compared to the small change in water temperature across the heat exchanger.

VI.4. Results

Using the methods described above, pressure drop and heat transfer tests were performed on two fabricated heat exchangers. Measurements and model predictions over the accurate measurement ranges of the testing apparatus are shown. The pressure drop constraints discussed in Chapter IV (Δp_{air} = 175 Pa, Δp_{water} = 5 kPa) are within these ranges.

Air pressure drop

Air pressure drop results are shown in Figure VI.3. The solid line is the pressure drop model predictions and the squares and circles are experimental data for two

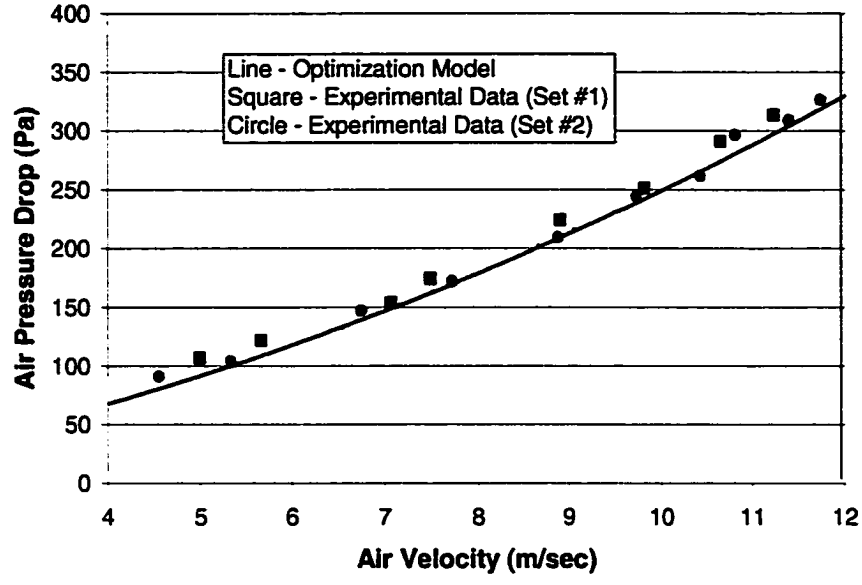

Figure VI.3 - Air pressure drop results

different heat exchangers. Over the air velocity range shown, the air channel Reynolds number varies from 78 to 235 indicating laminar flow.

Overall the model predicts the air pressure drop well, however the air pressure drop is generally slightly higher than the model predicts. The primary cause for this is likely the slight misalignment between the two halves of the heat exchanger. This creates a flow disturbance halfway through the thickness of the heat exchanger. Also, a thin glue layer halfway through the thickness of the heat exchanger and imperfect polishing may cause an increase in pressure drop at the inlet and exit of the air channels.

Water pressure drop

Results for water pressure drop measurements are shown in Figure VI.4. Circles and squares indicate experimental data for two different heat exchangers. The model pressure drop is calculated from Equation (IV.12) using rectangular channel empirical correlations to estimate the friction factor for non-fully developed flow. The value of the non-fully developed friction factor (f) is a function of velocity and geometry.

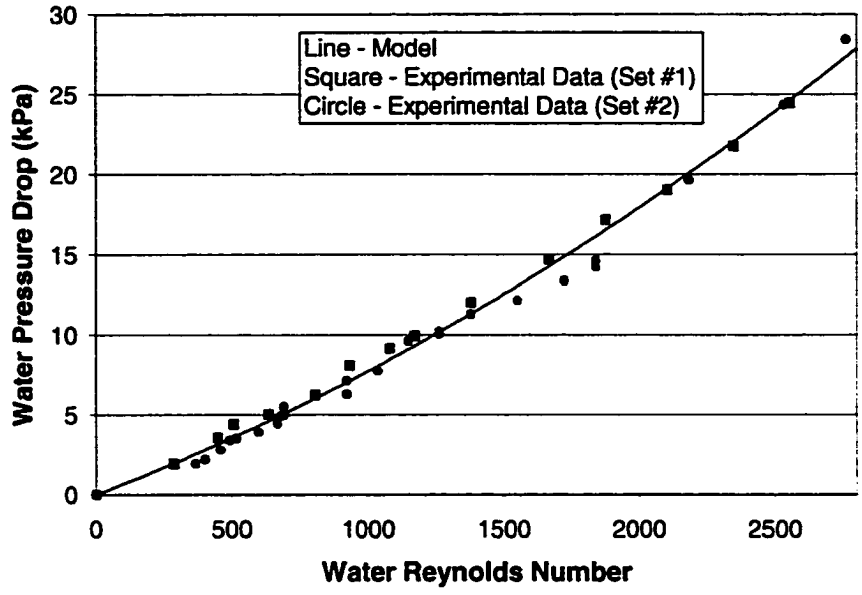

Figure VI.4 - Water pressure drop results

The flow rate of 0.6 lpm used for the heat transfer tests corresponds to a Reynolds number of 690 and pressure drop around 5 kPa. Overall the model predicts the water pressure drop well. Reasons the pressure drop would be expected to be greater than the model are slight misalignment between heat exchanger halves and varying channel depth down the length of the water channel. A reason why the pressure drop may be expected to be less than the model is the previously observed decrease in the friction for liquid flow in microchannels [35-39].

Heat transfer

The heat transfer results are presented in the form of the percentage change in air temperature as a function of air velocity or air pressure drop. The percentage change in air temperature is defined as the measured change in air temperature divided by the difference in temperature between the inlet air temperature and the average temperature of the water (Equation VI.1).

$$\%\Delta T = \frac{T_{air-exit} - T_{air-inlet}}{T_{water} - T_{air-inlet}} \qquad \text{(VI.1)}$$

This scale allows different heat exchanger test data with different inlet fluid temperatures to be compared using the same graph.

Heat transfer results as a function of air channel velocity are shown in Figure VI.5. The line is the optimization model predictions, the squares and circles are two sets of experimental data, and the asterisks represent the more accurate finite element model. The experimental data fits the finite element analysis model very well. Reasons why the heat transfer may be expected to be greater than model predictions are the omission of front and rear face convection and the added flow disturbances due to misalignment, polishing, and the glue layer. Reasons why the heat transfer may be expected to be less than model predictions are increased conduction lengths due to polishing and a glue layer near the bonding interface. Overall, the combined effects did not appreciably change the heat transfer results.

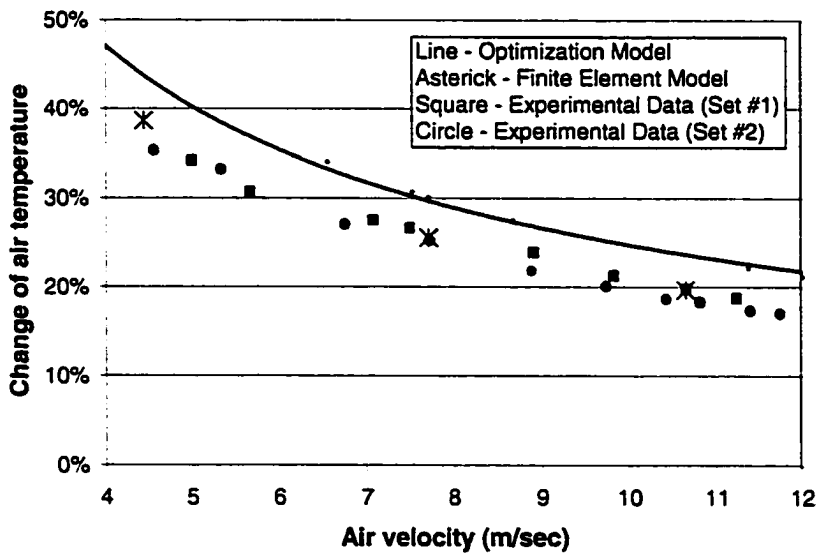

Figure VI.5 - Heat transfer results as function of air velocity

Heat transfer results as a function of air pressure drop are shown in Figure VI.6. Although this graph is a better measure of the performance of the heat exchanger, plotting the heat transfer in this manner introduces errors in the pressure drop model or pressure drop measurements into the results. The experimental data still fits the finite element analysis model well since the model for the pressure drop is satisfactory.

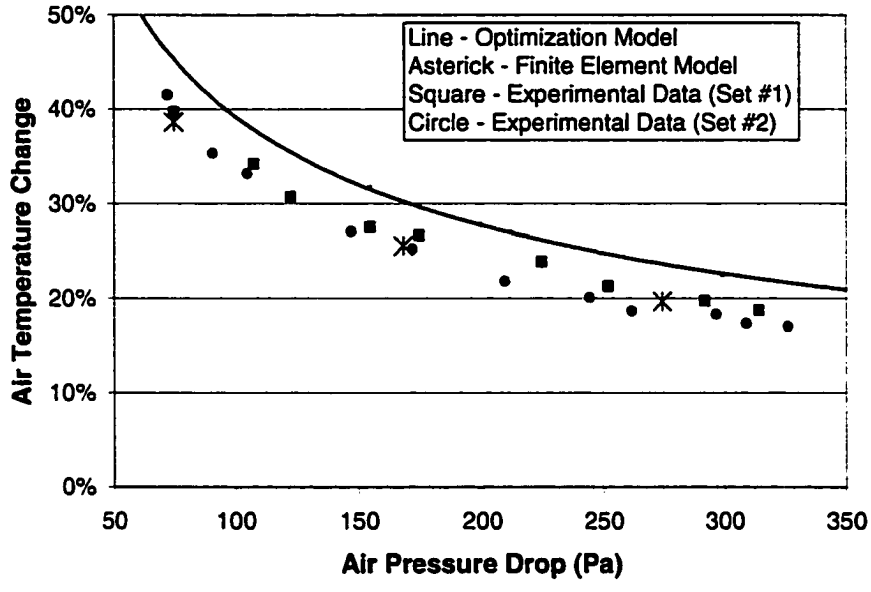

Figure VI.6 - Heat transfer results as function of air pressure drop

The normalized rate of heat transfer as a function of air pressure drop is shown in Figure VI.7. Although this figure is the best measure of performance, inaccuracies in the pressure drop and flow rate calculations and measurements are conveyed in the heat transfer results. At low pressure drops, the finite element model predicts less heat transfer than measurements. Inaccuracies of the pressure drop model lead to the deviations. Near the air pressure drop design constraint of 175 Pa, the finite element model predicted the heat transfer accurately.

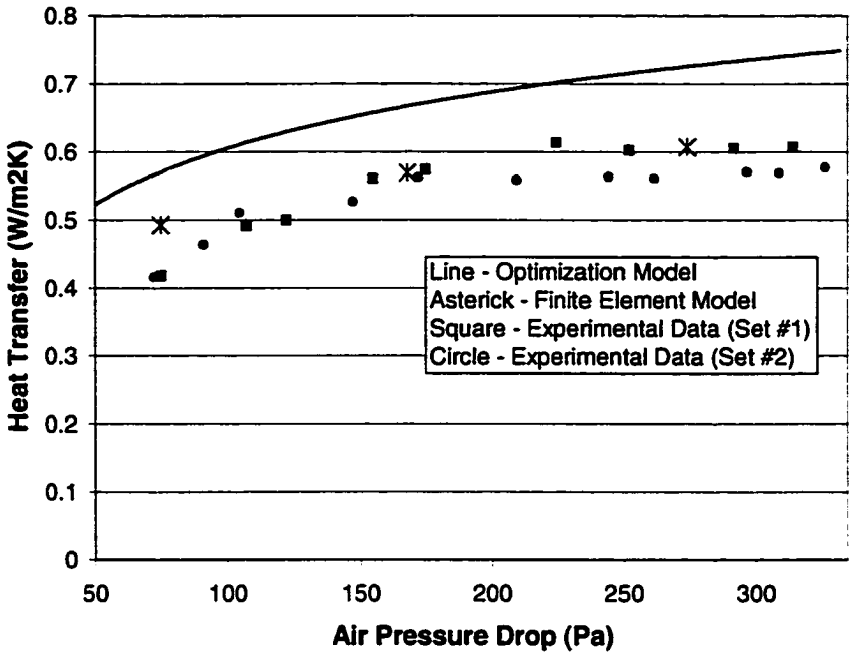

Figure VI.7 - Heat transfer results as function of air pressure drop

Heat Balance

The heat transfer could also have been estimated from measurements of the water flow rate and inlet and exit temperatures of the water. If the heat transfer were determined in this manner, the experimental heat transfer results would not be as accurate as the heat transfer results obtained from air measurements because the water changes temperature by only around 1°C and the thermocouple accuracy is 0.1°C. Another problem with the calculation of heat transfer from water measurements is heat losses between the thermocouples and the inlet and exit of the heat exchanger.

Heat transfer determined from the water flow rate and inlet and exit temperatures is valuable however. A heat balance between the air and water was used as additional verification of accurate heat transfer measurement. The expected water temperature change obtained from the heat balance is shown in Equation (VI.2).

$$\dot{m}_{air}\, c_{p-air}(T_{air-exit} - T_{air-inlet}) = \dot{m}_{water}\, c_{p-water}(T_{water-exit} - T_{water-inlet}) \quad \text{(VI.2)}$$

The water temperature drop due to heat losses between the inlet and exit of the heat exchanger and the thermocouples was estimated by measuring the temperature drop between thermocouples for steady state heat transfer with no forced air flow. This method slightly overestimates the heat loss since a small amount of heat exchange still occurs within the heat exchanger due to natural convection and conduction. The estimated temperature drop due to heat loss is added to the expected water temperature change calculated in Equation (VI.3). The calculated and measured water temperature changes are shown in Figure VI.8. The agreement between the expected and measured water temperature changes is within the uncertainty of the measured water temperature change (15%) verifying the heat transfer measurements.

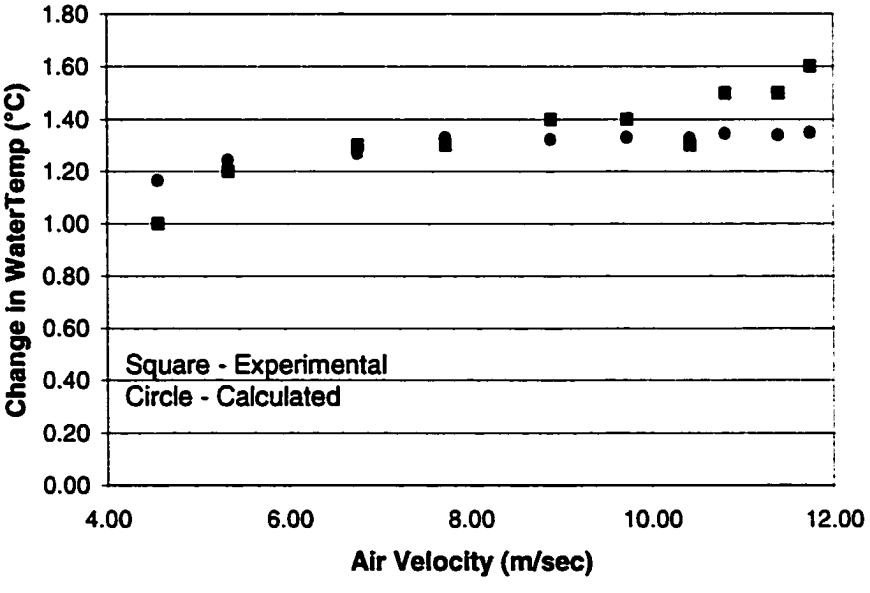

Figure VI.8 – Actual and expected exit temperature of water

Maximum pressures before leakage

The testing apparatus limited the maximum allowable air and water pressures. Due to pressure losses between the compressed air source and heat exchanger, the maximum attainable air pressure at the front face of the heat exchanger was 0.5 psi. At this pressure, there was no water leakage. The water pressure transducer limited the maximum allowable water pressure to 30 psi. For water pressures at the inlet plenum up to 30 psi, no heat exchanger leakage was observed.

CHAPTER VII - METAL CROSS FLOW MICRO HEAT EXCHANGER

VII.1. Introduction

The cross flow micro heat exchanger previously discussed achieved high heat transfer rates in a small volume with low fluid pressure drops. The performance of this heat exchanger can be improved by fabricating the heat exchanger out of a more thermally conductive material. The plastic cross flow micro heat exchanger also has a limited maximum operating temperature. These drawbacks provide the motivation to fabricate a new cross flow micro heat exchanger out of metal using many of the same technologies used to fabricate the initial plastic cross flow micro heat exchanger. The metal cross flow micro heat exchanger was fabricated using i) the LIGA technique to produce a plastic sheet with through holes, ii) electroless plating a layer of metal uniformly over the entire plastic sheet (including in the holes), and iii) dissolving the plastic. The result is a metal cross flow micro heat exchanger that has exceptional performance and can operate in high temperature environments. Envisioned applications again include automobile radiator, air conditioning, and aerospace. In this chapter, the design, fabrication, and testing of the metal cross flow micro heat exchanger will be described. The previously described cross flow micro heat exchanger will be referred to as the plastic cross flow micro heat exchanger.

VII.2. Design

Conceptual Design

A schematic of the metal cross flow micro heat exchanger is shown in Figure VII.1. The conceptual design is very similar to that of the plastic cross flow micro heat

exchanger. Numerous parallel, short air channels allow a substantial flow rate of air with a low pressure drop. The water channel meanders around the outside of the air channels resulting in more intimate contact between the air and water. This reduces the conduction lengths and conduction heat transfer resistance.

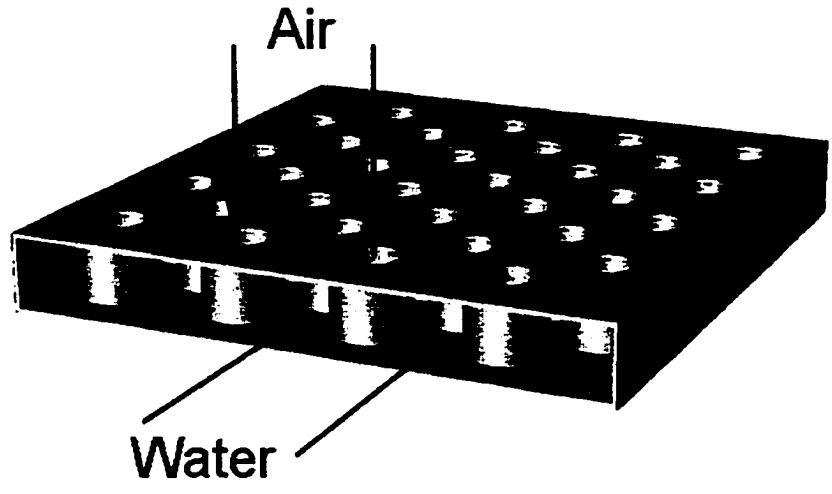

Figure VII.1 – Schematic of metal heat exchanger

Performance Parameters

The performance parameters will be the same as those discussed in Chapter IV. The goal is to design a cross flow micro heat exchanger to maximize heat transfer/frontal area within specified design constraints.

Design Constraints

The fluids (air and water), pressure drops (Δp_{air} = 175 Pa, Δp_{water} = 5 kPa), and temperature of the fluids ($T_{air\text{-}inlet}$ = 25°C, $T_{water\text{-}inlet}$ = 58°C) will be same as those for the plastic cross flow micro heat exchanger. The basic schematic for the geometry of the cross flow micro heat exchanger is shown in Figure VII.2. The air channel shape is a hexagon and will be discussed in step 8 of the calculations.

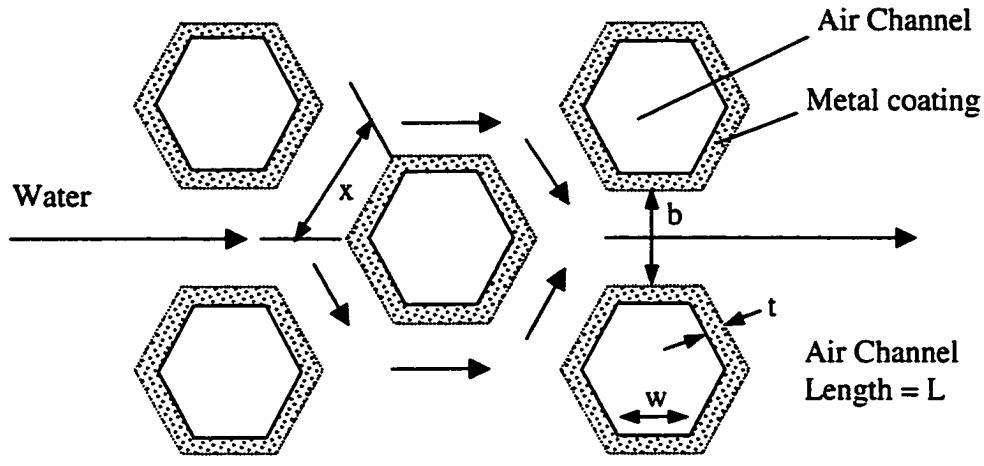

Figure VII.2 - Schematic for Design Constraint Variables

The variables in the optimization are the length of one side of the hexagon (w) and the width of the water channel (b). As the hexagon side length (w) increases, the open area for air flow increases however the air convection coefficient decreases. As the width of the water channel (b) increases, open area for water to flow increases but the open area for air to flow decreases. To ensure successful fabrication, the minimum water channel width (b) is given a value of 150 μm. The thickness of the metal (t) is not a design variable and is given a value of 70 μm for adequate strength. It will be shown later that the metal thickness is an important variable controlling the air channel density and, therefore, heat transfer. The equivalent water channel length (x) is determined by values of the hexagon side length (w), width of the water channel (b), and thickness of the metal (t). The air channel length (L) is also not a design variable and is given a value of 1 mm or 2 mm. By selecting values for the optimization variables for good performance using air channel lengths of 1 mm and 2 mm, initial prototype development can be performed to produce a 1 mm thick heat exchanger. Subsequent thicker (2 mm) heat exchangers can then be made by several methods. To fabricate a

thicker heat exchanger, two electroless plated heat exchangers could be stacked, two sheets of PMMA with through holes could be stacked then electroless plated to form the heat exchanger, or the thicker heat exchanger could be fabricated directly using the same x-ray mask. For prototype development purposes, the maximum size of the heat exchanger is 1.3" X 1.5" (F_w X F_h). These dimensions could be increased dramatically if the need existed.

Optimization and Modeling Calculations

The geometry that maximizes heat transfer/frontal area has been calculated for a nickel-phosphorous (k = 4.2 W/mK [64]) cross flow micro heat exchanger. The modeling assumptions and values of the fluid properties are the same as those used in the optimization of the plastic heat exchanger.

Many of the same equations used in modeling the plastic cross flow micro heat exchanger will be used to model the metal cross flow micro heat exchanger. These equations will be included in this section for continuity purposes. The modeling program is not included however it is similar to the program shown in Appendix A. The following calculation steps were used to optimize and predict the metal heat exchanger performance.

1. The hydraulic diameter of the air channel, $D_{h\text{-}air}$, is calculated as 4A/P where A is the cross sectional area of the air channel and P is the perimeter. Using the geometry of an equilateral hexagon with equal internal angles, Equation (VII.1) is derived.

$$D_{h-air} = \sqrt{3}w \qquad \text{(VII.1)}$$

2. The relation between the pressure drop across the channel and the velocity of air through the channel is given by Equation (VII.2) where the first term on the right hand

side is pressure drop caused by viscous drag and the second term is related to inlet and exit losses. The constant K is the minor loss coefficient. The inlet minor loss coefficient was estimated for a rounded pipe entrance ($r/D_h = 0.21$) as 0.03 [65]. The exit minor loss coefficient for laminar flow and a ratio of free flow area to total frontal area of 0.33 was estimated to be 1.15 using correlations for heat exchangers [3]. The sum of the inlet and exit minor loss coefficients result in an overall estimated value of 1.18 for the minor loss coefficient. The value of the non-fully developed friction factor, f, is a function of velocity and geometry and is obtained from empirical correlations for non-fully developed flow through square and circular channels [40]. Since little data is available for developing flow in hexagonal channels, the average of the friction factor for square and circular channels is used to approximate the flow behavior. For fully developed laminar flow, the friction factor obtained using this averaging method only deviates from the friction factor for hexagonal channels modeled using a finite difference method by 0.5% [65]. Both the friction factor, f, and the bulk velocity, V, are iteratively calculated using Equation (VII.2) and given values of Δp, L, ρ, and $D_{h\text{-}air}$.

$$\Delta p_{air} = \frac{f \rho_{air} V_{air}^2 L}{2 D_{h-air}} + K \frac{\rho_{air} V_{air}^2}{2} \qquad \text{(VII.2)}$$

3. The average non-fully developed Nusselt number in the air channels is a function of the dimensionless quantities in Equation (VII.3) and is obtained from the average of empirical correlations [40] for circular and square channels. For fully developed laminar flow, the Nusselt number obtained using this averaging method only deviates from the Nusselt number for hexagonal channels modeled using a finite difference

method by 2% [65]. The Nusselt number is required to determine the convection coefficient on the inner walls of the air channel.

$$Nu = \frac{h_{air} D_{h\text{-}air}}{k_{air}} = f\left(\frac{L}{D_{h\text{-}air} Re Pr}, \frac{w}{H} \right) \qquad \text{(VII.3)}$$

4. The water channel flow is difficult to model accurately. Fortunately, it is not crucial to closely predict the water flow heat transfer characteristics because heat transfer is insensitive to the water pressure drop and the water/wall convection resistance is very small compared to the air/wall convection resistance. For the model that will be used to estimate the convection coefficient and pressure drop of the water, short independent non-fully developed water channels of equivalent length (x) will be used.

The water channels will be broken up into two types depending on the water flow rate. Figure VII.3 illustrates that the mass flow for some water channels (dots) is greater than other water channels (shaded). In subsequent water pressure drop equations, the high flow rate water channels will be denoted by the subscript (high fr) and the low flow rate water channels will be denoted by the subscript (low fr). The ratio of the number of lower mass flow rate water channels to the number of higher mass flow rate water channels is two to one. This ratio will be used in calculating the average convection coefficient. Since the different flow rate channels are in series, the pressure drop for each type of channel will be added.

The relation between the pressure drop across the channel and the velocity of water through the channel is given by Equation (VII.4). The inlet and exit losses within the heat exchanger are estimated using the high flow rate channels. It is assumed that the inlet loss into the high flow rate water channel accounts for the exit loss from the low

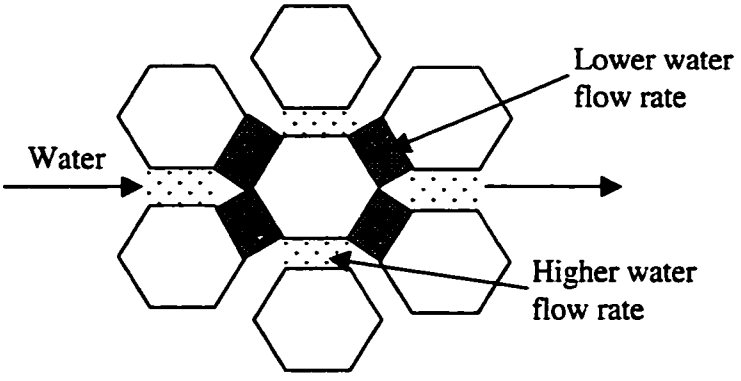

Figure VII.3 – Schematic of two types of water channels

flow rate water channel and the exit loss from the high flow rate water channel accounts for the inlet loss into the low flow rate water channel. Inlet and exit minor loss coefficients were estimated for laminar flow and a ratio of free flow area to total frontal area of 0.5. The sum of the estimated inlet minor loss coefficient (0.18) for a gradual contraction with an included angle of 120° and the estimated exit minor loss coefficient (0.30) results in an overall estimated value of 0.48 for the minor loss coefficient [66]. The overall minor loss coefficient associated with flow entering and leaving the heat exchanger is estimated to be 0.85 [66] for a ratio of free flow area total frontal area of 0.25. The value of the non-fully developed friction factor, f, is a function of velocity and geometry and is obtained from curve fit tabular empirical correlations for non-fully developed flow through rectangular channels [40]. Both the friction factor, f, and the bulk velocity, V, are iteratively calculated using Equation (VII.4) and given values of Δp, L, ρ, and $D_{h\text{-water}}$. The hydraulic diameter is again calculated as four times the cross sectional area of the channel divided by the perimeter of the channel.

$$\Delta p_{water} = \begin{pmatrix} \left(\frac{N_{water} f \rho_{water} V_{water}^2 L}{2D_{h-water}}\right)_{lowfr} + \left(\frac{N_{water} f \rho_{water} V_{water}^2 L}{2D_{h-water}}\right)_{highfr} + \\ \left(N_{water} K \frac{\rho_{water} V_{water}^2}{2}\right)_{highfr} + \left(K \frac{\rho_{water} V_{water}^2}{2}\right)_{inlet,exit} \end{pmatrix} \quad \text{(VII.4)}$$

Due to the conservation of mass of an incompressible fluid, the water velocity in the high flow rate channels is twice the water velocity in the low flow rate channels. From geometry, the number high flow rate water channels in a series is calculated using Equation (VII.5).

$$(N_{water})_{series} = \frac{F_w}{3\left(w + \frac{2t}{\sqrt{3}} + \frac{b}{\sqrt{3}}\right)} \quad \text{(VII.5)}$$

Since the adjacent low flow rate water channels are in parallel, this equation is also valid for the calculation of the number of low flow rate water channels used in Equation (VII.4).

The average non-fully developed Nusselt number in the water channels is a function of the dimensionless quantities in Equation (VII.6) and is obtained from curve fit tabular empirical correlations [40]. A weighted average is used because the flow rate is low around four sides of the hexagon and high around only two sides of the hexagon. The Nusselt number is required to determine the convection coefficient on the outer walls of the air channel.

$$Nu = \frac{h_{water} D_{h\text{-}water}}{k_{water}} = \frac{2 * f\left(\frac{L}{D_{h\text{-}water} Re Pr}\right)_{lowfr} + f\left(\frac{L}{D_{h\text{-}water} Re Pr}\right)_{highfr}}{3} \quad \text{(VII.6)}$$

5. The heat transfer to each air channel can now be calculated. Figure VII.4 shows the resistive network between the water and air. The dashed line is the boundary of the unit

cell being analyzed. R_1 is the convection resistance at the water/wall interface. R_2 is the conduction resistance through the thickness of the wall separating the water and air channels based on the average wall width. R_3 is the average convection resistance at the air/wall interface. The values of R_1, R_2, and R_3 are given by Equations (VII.7a, b, and c).

$$R_1 = \frac{1}{h_{water}(w + \frac{2t}{\sqrt{3}})L} \qquad \text{(VII.7a)}$$

$$R_2 = \frac{t}{k_{wall}(w + \frac{t}{\sqrt{3}})L} \qquad \text{(VII.7b)}$$

$$R_3 = \frac{1}{h_{air} wL} \qquad \text{(VII.7c)}$$

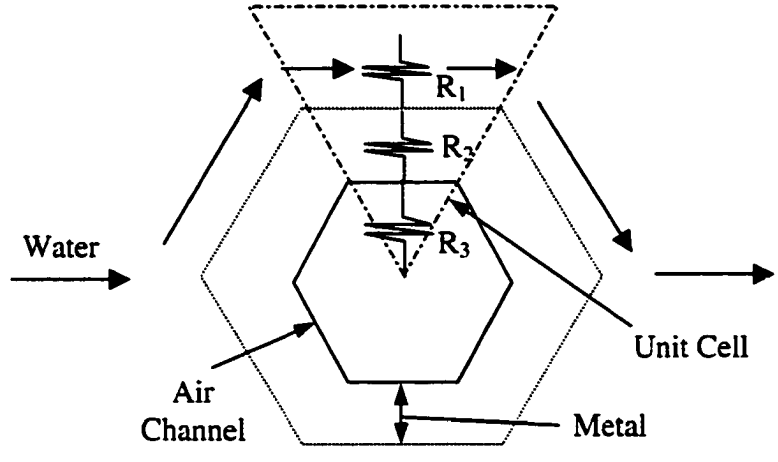

Figure VII.4 – Resistance Network

The sum of R_1, R_2 and R_3 equals the resistance between the water and air in the unit cell. By symmetry, the total heat transfer resistance (R_{tot}) to a single air channel is one sixth this sum.

$$R_{tot} = \frac{R_1 + R_2 + R_3}{6} \qquad \text{(VII.8)}$$

Assuming the water temperature is constant and equal to the inlet water temperature, the exit temperature of the air is calculated by manipulating Equation (VII.9).

$$\frac{T_{water\text{-}inlet} - T_{air\text{-}exit}}{T_{water\text{-}inlet} - T_{air\text{-}inlet}} = \exp\left(-\frac{1}{\dot{m}_{air} c_{p\text{-}air} R_{tot}}\right) \qquad \text{(VII.9)}$$

Using the geometry of the equilateral hexagon with sides of length (w) and equal internal angles, Equation (VII.10) is derived to calculate the air mass flow rate.

$$\dot{m}_{air} = \rho_{air} V_{air} \left(\frac{3\sqrt{3}}{2} w^2\right) \qquad \text{(VII.10)}$$

Finally, the heat transfer between the water and a single air channel is given by Equation (VII.11).

$$q_{channel} = \dot{m}_{air} c_{p\text{-}air} (T_{air\text{-}exit} - T_{air\text{-}inlet}) \qquad \text{(VII.11)}$$

To determine the number of air channels, the frontal area of the unit cell occupying a single air channel is calculated using Equation (VII.12).

$$A_{cell} = 2\sqrt{3}\left(\frac{\sqrt{3}}{2} w + t + \frac{b}{2}\right)^2 \qquad \text{(VII.12)}$$

An excellent estimation of the total number of air channels (N) in the heat exchanger is obtained by dividing the total frontal area of the heat exchanger (F_w x F_h) by this unit cell area. The total heat transfer for the heat exchanger is given by Equation (VII.13).

$$q = N q_{channel} \qquad \text{(VII.13)}$$

6. The initial assumption that the exit temperature and inlet temperature of the water are equal provides a slightly high estimate of the total heat transfer. A simple process greatly reduces the error.

i) To calculate the water mass flow rate, the number of parallel, high flow rate water channels is calculated using Equation (VII.14).

$$(N_{water})_{highfr-parallel} = F_h \left(\frac{1}{\frac{4w}{\sqrt{3}} + 2t + b} \right) \qquad \text{(VII.14)}$$

ii) The mass flow rate of the water through the heat exchanger is then determined from Equation (VII.15).

$$\dot{m}_{water} = (N_{water})_{highfr-parallel} \rho_{water} (V_{water})_{highfr} b(L - 2t) \qquad \text{(VII.15)}$$

iii)Using Equation (VII.16) the exit temperature of the water is calculated.

$$q = \dot{m}_{water} c_{p-water} (T_{water-inlet} - T_{water-exit}) \qquad \text{(VII.16)}$$

iv) The average value of the water temperature is the average of $T_{water-inlet}$ and $T_{water-exit}$. Since the water changes temperature by less than 4°C, this is a reasonable estimate of the average water temperature. If greater accuracy is desired, this average temperature could be substituted into Equation (VII.9) as the updated value of T_{water} and repetition of equations (VII.9, 11, 13, and 16) would produce a new value of $T_{water-exit}$. Once the average water temperature is determined, the heat transfer is calculated using Equation (VII.17).

$$q_{final} = q \frac{(T_{water-avg} - T_{air-inlet})}{(T_{water-inlet} - T_{air-inlet})} \qquad \text{(VII.17)}$$

7. Initial estimates of the length of one side of the hexagon (w) and the width of the water channel (b) as well as the material properties of the heat exchanger and fluids are the inputs required to solve Equations (VII.1)-(VII.17) and calculate the heat transfer between the water and air. The heat exchanger design is optimized by holding one

variable constant while the value of the second is varied to maximize heat transfer/frontal area. The second variable assumes this new value during the next step in the optimization process where the first is varied to find a maximum. This iterative procedure is continued and quickly converges.

8. In the above analysis, hexagonal air channels were used. Other air channel shapes (circle and square) were investigated to determine if hexagonal air channels optimize heat transfer. Calculations proved hexagonal air micro channels are optimum for heat transfer due to the water channel width constraints. Under this constraint, the different channel shapes lead to a reduction in the open area for air to flow. The result is lower rates of heat transfer for non-hexagonal channels. Although hexagon shaped air channels produce the highest rates of heat transfer under the design constraint, circles may be a better air channel shape for strength purposes.

9. Once the heat exchanger was designed, the overall heat transfer coefficient, U, was calculated using Equation (VII.18).

$$U = \frac{q_{final}}{A_{HT} T_{lm}} \qquad \text{(VII.18)}$$

A_{HT} is the total heat transfer area for both the air and water channels and T_{lm} is the log mean temperature difference between the water and air in the heat exchanger. The overall heat transfer coefficient is a measure of the heat transfer resistance between the fluids.

The volume of the heat exchanger was calculated by multiplying the frontal area of the heat exchanger by the length of the air channels. To determine the mass of the fabricated heat exchanger, an effective volume of heat exchanger material was calculated using the geometry of the unit cell. The effective material volume was

multiplied by the density of the heat exchanger material to calculate the mass of the heat exchanger. Since the mass of current innovative dry radiators is typically reported, the mass of the water in the heat exchanger channels was not included in the calculation of the mass of the heat exchanger.

10. A finite element analysis of the optimized metal heat exchanger was not necessary due to the relatively high conductivity of metal and the intimate contact between the water and air (i.e. short conduction lengths).

Results

The optimum designs for the nickel-phosphorous cross flow micro heat exchanger are shown in the first two rows of Table VII.1. A compromise between the optimum designs was selected to produce good performance for heat exchangers of varying thickness. The values chosen for the optimization variables were a hexagon side length of 245 μm and a water channel width of 150 μm. The heat exchanger performance using these dimensions is shown in the bottom two lines of Table VII.1. There is negligible predicted performance loss using the selected design compared to the optimized designs.

Table VII.1 – Optimum and actual designs

	L (mm)	w (μm)	N_{air}	Open Area	V_{air} (m/sec)	Re_{air}	m (g)	U (W/m^2K)	q (W)
Optimum	1.1	230	3060	33.5%	11.0	271	3.80	468	**52.7**
Optimum	2.2	280	2420	39.1%	9.2	308	6.33	332	**71.1**
Actual	1.1	245	2845	35.3%	11.3	296	3.72	464	**52.6**
Actual	2.2	245	2845	35.3%	9.6	252	6.65	335	**70.3**

As the length of the heat exchanger (L) increases, the optimum hexagon side length (w) increases to allow a larger air flow rate under the pressure drop constraint.

Increasing the hexagon side length decreases the number of air channels, however the open area for air flow is increased. Though not shown, the optimum value for the water channel width (b) is equal to the design constraint (150 μm) indicating a performance enhancement for narrower water channels. The low Reynolds numbers show the flow through the air channels is laminar. The mass of the fabricated 1.5" X 1.3" heat exchanger is expected to be very light (only be few grams). Though not shown, the water/wall convection resistance and the metal wall conduction resistance accounted for less than 2% and 1%, respectively, of the overall heat transfer resistance. The performance of the metal cross flow micro heat exchanger will be compared to the previous micro heat exchangers and conventional scale heat exchangers in the performance measurement chapter.

The sensitivities of several design constraints are shown in Table VII.2.

Table VII.2 – Sensitivities

	b	t	L	P_{air}	P_{water}
Sensitivity (%)	-22	-41	46	29	4

The sensitivities were calculated for the selected design. As shown by the highest sensitivity of 46%, increasing the length of the air channel (L) is most important in improving heat transfer. In other words, increasing the length of the heat exchanger by 10% while holding the other geometrical parameters and pressure drops constant, will increase the heat transfer by approximately 4.6%. The longer air channel increases the surface area for heat transfer causing the air temperature change to increase. This heat transfer advantage overrides the fact that the mass flow rate of the air decreases to satisfy the pressure drop constraint. A longer air channel also increases the area for

water flow allowing a larger water flow rate. A disadvantage of increasing the length of the air channel is an increase in the volume and mass of the heat exchanger.

Decreasing the thickness of the metal (t) is also important in improving heat transfer. By decreasing the wall width, there is more space for micro channels. The effect of the wall thickness on overall thermal resistance is negligible. The disadvantage of reducing the metal thickness is a reduction in strength.

Less important dimensions for heat transfer are the width of the water channel (b) and the air pressure drop (P_{air}). By decreasing width of the water channel, the area for air channels is increased thereby increasing the flow rate of the air. The disadvantage of reducing the width of the water channel is increased difficultly of fabrication and a reduced water flow rate that results in a larger water temperature change (i.e. lower average water temperature). By increasing the air pressure drop constraint, the amount of heat transfer is increased due to a larger flow rate of air through the heat exchanger. This results in higher convection coefficients and a greater temperature difference between the water and air because the air exits the heat exchanger cooler. As shown by a very low sensitivity, the pressure drop of the water (P_{water}) is not an important factor for heat transfer performance.

VII.3. Fabrication

The metal cross flow micro heat exchanger was fabricated using a combination of the LIGA process, conventional machining, sputtering, and electroless plating. Initially, the LIGA process and conventional machining were used to produce a sheet of plastic with through holes. A thin conductive layer was then sputtered over the entire plastic

sheet. Electroless plating built up a thicker metal layer uniformly over the sputtered layer. Dissolving the plastic completed the fabrication of the heat exchanger.

LIGA Process

Although the LIGA process (Figure V.1) was explained in detail in Chapter V, the process used to produce the plastic sheets with hexagonal through holes will now be summarized. The x-ray mask used in the LIGA process is shown in Figure VII.5. The gold absorber forms a honeycomb shape on the graphite membrane. In the hexagons where no gold has been plated, x-rays penetrate through the mask during exposure to pattern sheet of PMMA behind the mask. The PMMA is then developed removing the x-ray damaged plastic. If the PMMA is bonded to a metal substrate, nickel is electroplated into the plastic voids to fabricate a mold insert. A mold insert with 1.1 mm tall hexagonal nickel structures is shown in Figure VII.6. If, during exposure, the PMMA was not bonded to a metal substrate, a plastic sheet with hexagonal through holes would be produced. The plastic sheet could then be sputtered and electroless plated to fabricate the heat exchanger. Although this method requires fewer steps, each plastic sheet needs to be exposed to x-rays. This is both time consuming and expensive. Therefore the plastic sheet was molded using the mold insert shown in Figure VII.6. A fabricated plastic (PMMA) sheet molded by embossing is shown in Figure VII.7. The plastic forms the honeycomb structural pattern that will be covered with metal. After molding, the backside of the molded piece was fly cut and polished using 600 grit sandpaper to open the hexagons.

Figure VII.5 – X-ray mask for metal heat exchanger

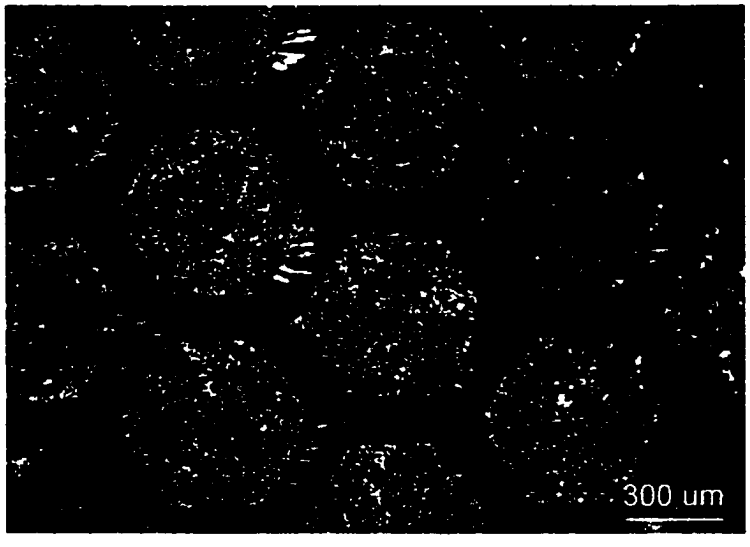

Figure VII.6 – Mold insert for metal heat exchanger

Metallizing

In order to electroless plate on a non-conductive substrate such as PMMA, a conductive layer capable of initiating the deposition reaction needs to be applied (termed metallizing). Metals that can initiate the deposition reaction are classified in two categories. The first category is intrinsically catalytically active materials such asnickel, palladium, and platinum. These are the metals that can sustain electroless

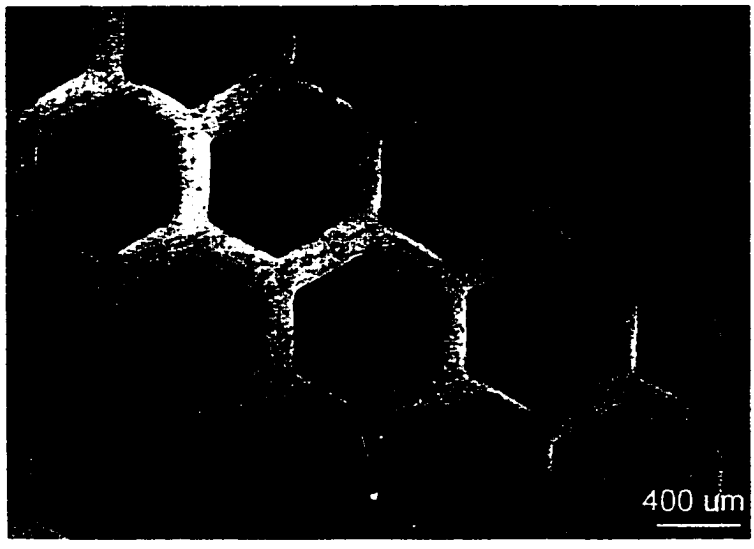

Figure VII.7 – Embossed plastic sheet for metal heat exchanger

deposition directly. The other category is extrinsically catalyzed materials. Although the surface of this type of material is not catalytically active, the nuclei of an intrinsically active material such as nickel are deposited on the surface to initiate catalytic activity. Within this category, there are metallic materials less noble and metallic materials more noble than nickel. Metals that are less noble than nickel such as iron, aluminum, and titanium can be immersed in the electroless plating solution to deposit nickel via a displacement exchange thereby allowing further electroless deposition. The displacement reaction does not occur on metals that are more noble than nickel such as copper, silver, and gold. These metals can still be electroless plated by placing them in contact with a metal less noble than nickel creating a galvanic cell to deposit nickel.

The most common metal to coat non-conductive substrates with is palladium (intrinsically catalytically active). Once the palladium is covered with nickel, electroless plating will continue since nickel is also intrinsically catalytically active.

Common methods used to metallize plastics prior to electroless plating include chemical deposition, sputtering, and chemical vapor deposition (CVD). Since a CVD machine was not readily available, the chemical deposition and sputtering methods were investigated. In chemical deposition, the sample is typically coated with palladium using several steps involving chemical dips. The sequence frequently used to chemically deposit palladium is outlined below [64,68].

1. Cleaning
2. Swelling
3. Etching
4. Neutralizing, conditioning
5. Activation
6. Reduction

Two common plastics that are best suited for this method are ABS and polypropylene. Not included in the plastics best suited for the chemical deposition method are polyethylene, polycarbonate, and PMMA. These are the plastics that are currently being micro-molded at LSU. Attempts at using chemical deposition to coat polycarbonate and PMMA with palladium using this method were unsuccessful.

The other method investigated to coat the plastic piece with a conductive layer is sputtering. In sputtering, plasma is created by bombarding a disc of the material to be deposited at a high negative potential with positive argon ions. Neutral atoms are ejected from the disc and are deposited on the substrate creating a thin conductive layer [42]. Sputtering can occur at a low temperature making it suitable for plastics. A multitude of metals can be deposited using sputtering. Since palladium is commonly

used in electroless plating and a gold-palladium target was readily available, a thin gold-palladium layer of thickness 50-80 nm was applied over the plastic sheet. In order to ensure the inside of the hexagons were coated, the plastic sheet was angled at 45° to the sputtering target. Using a Edwards S150 sputter coater machine, the sample was sputtered for 30 seconds at an argon pressure of 0.08 torr and current of 15 mA. By rotating the sample at 90° increments and sputtering, then flipping the sample and repeating the same process, the inside of the holes were coated. The sample was sputtered a total of eight times. The backside of the embossed piece after fly cutting, polishing, and sputtering is shown in Figure VII.8.

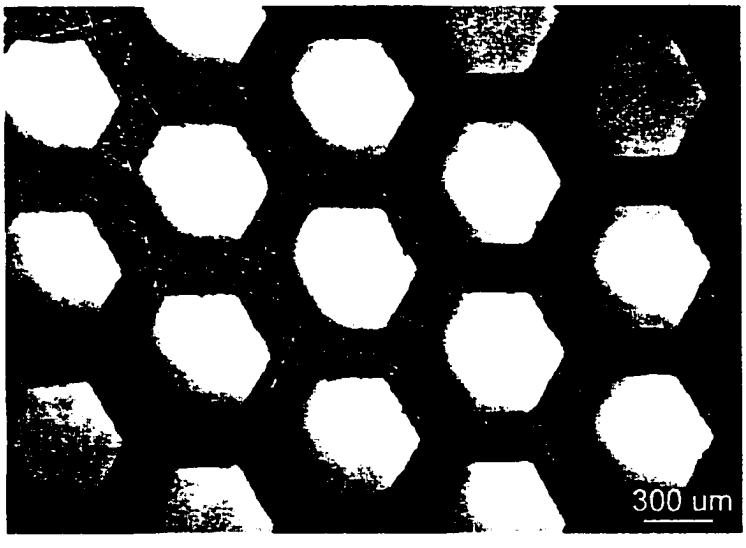

Figure VII.8 – Backside of embossed piece after sputtering

Electroless Plating

Electroless plating describes the deposition of metal onto a suitable substrate by chemical reduction. A variety of industries utilize electroless plating. Electroless copper is used by the electronics industry to create a thin conductive layer on circuit boards. Electroless nickel is used by numerous industries such as chemical, transport,

automobile, and textile for corrosion resistance, wear resistance, and coating complex shapes with high luster.

Due to its higher mechanical strength, electroless nickel was selected as the heat exchanger material over electroless copper. Attributes of electroless nickel include very high plating uniformity resulting in shiny deposits, good corrosion resistance, excellent wear resistance, and high hardness. Disadvantages of electroless nickel are low ductility and a high cost compared to electroplated nickel.

The two types of electroless nickel are nickel-phosphorous and nickel-boron. The nickel-phosphorous electroless bath was selected because it is more widely available and provides a more ductile deposit than nickel-boron baths. The bath used to electroless plate the heat exchanger was the Vandalloy 4200 High Phosphorous System by Macdermid Industrial Products. This bath is very stable and suited for plating heavy build deposits (over 50 μm). The high phosphorous concentration (11%) compared to other electroless nickel baths results in the highest deposit ductility possible and low internal stress. The plating conditions shown in Table VII.3 result in a plating rate of 12 μm per hour.

Table VII.3 – Electroless nickel plating conditions

	T (°C)	pH	Bath Size (L)	Agitation Rate (RPM)
Plating Conditions	88	5.0	6	180

The mechanical properties of electroless nickel deposits vary considerably from pure nickel. A comparison between the mechanical properties of electroless nickel deposits and pure nickel is shown in Table VII.4. In addition to the differences in properties, the

microstructure of high phosphorous electroless nickel is non-crystalline whereas the microstructure of pure nickel is crystalline face centered cubic.

Table VII.4 – Mechanical properties of electroless and pure nickel

	ρ (g/cm^3)	k (W/mK)	Tensile Strength (MPa)	Elongation (%)	Modulus (GPa)
Electroless [64]	7800	4.2	750	2	65
Pure [68]	8900	85	480	40	207

Properties such as the density and ductility vary with phosphorous content. The quality of the deposit as well as the phosphorous content in the deposit depends on the bath composition, temperature, pH, and agitation. In order to have consistent properties throughout the deposit, these parameters need to be controlled during plating. Replenishing the bath periodically with consumed constituents controls the bath composition. The temperature is held constant by placing the electroless bath in a constant temperature water bath. The pH is checked and adjusted using appropriate acids or bases before plating to ensure the correct bath pH. Agitation is necessary to drive hydrogen bubbles from the part surface to avoid pitting. For agitation, an electronic motor driven stirrer is used to rotate the sample during plating. A special jig was machined to hold the sample and connect to the rotating shaft. To remove bath particles that reduce deposit quality, the plating solution was constantly filtered during plating.

After electroless plating, the plastic was first dissolved using acetone. Then chloroform was used in an ultrasonically-agitated bath. A heat treatment was not used because it would reduce the ductility of the nickel and might cause the deposit to crack [64].

An overview of a fabricated metal heat exchanger is shown in Figure VII.9. The thickness of the nickel-phosphorous is about 70 μm. Entrances into the air channels are slightly rounded and the plating is uniform. The plastic that defined the water channels has been completely dissolved and the passages are well defined. A side view of two air channels is shown in Figure VII.10. The entrance into the air

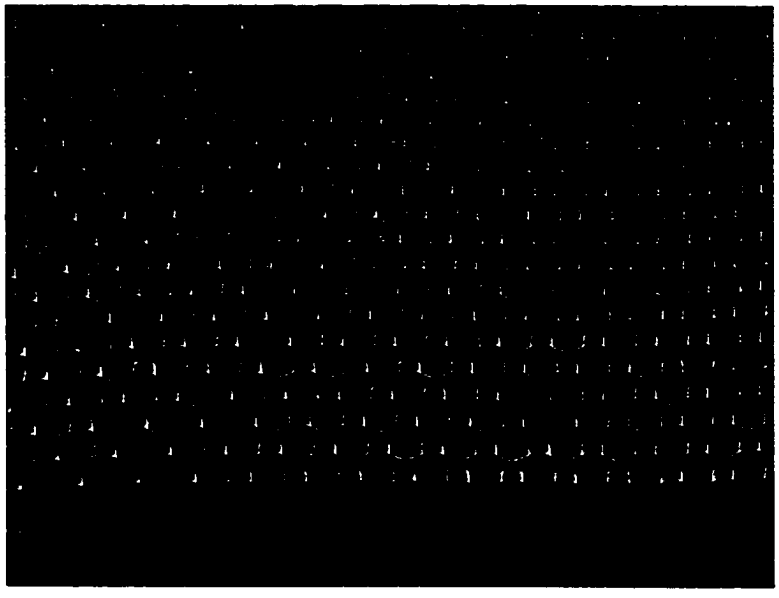

Figure VII.9 – Fabricated metal cross flow micro heat exchanger

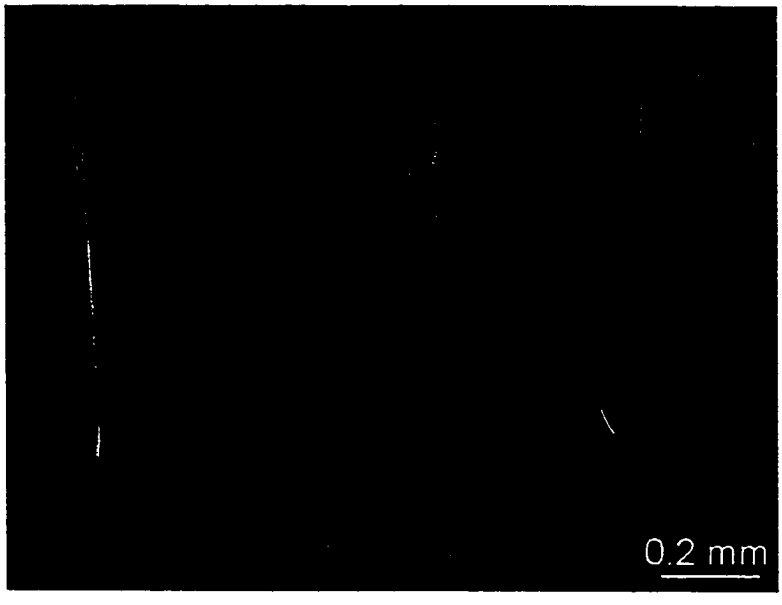

Figure VII.10 – Cross section of air and water channels

channels is rounded. Striations created during x-ray exposure were reproduced by electroless plating indicating high plating uniformity. A top view of several air channels is shown in Figure VII.11. As shown by minimal rounding of hexagon corners, the contour of the plastic was replicated by the electroless plating. A magnified picture of several water channels is shown in Figure VII.12. The water passages are well defined and the plastic has been completely dissolved.

Figure VII.11 – Top view of air channels

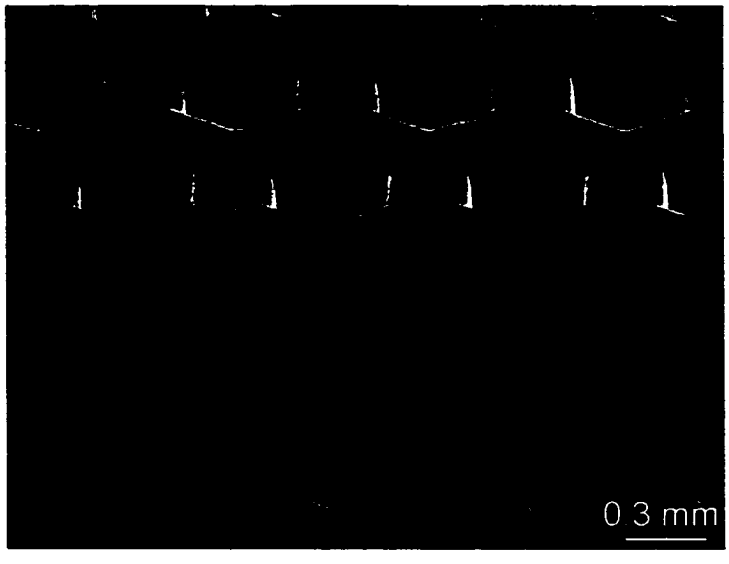

Figure VII.12 – Magnified view of water channels

Stacking

Numerous plastic sheets with through holes can be stacked and bonded prior to sputtering and electroless plating to increase the thickness of the heat exchanger. Figure VII.13 shows a thick (over 2 mm) metal heat exchanger created from stacking two plastic sheets with through holes. The plastic sheets were aligned using lead polished to the dimensions of the holes and bonded using heat. The result of a thicker metal heat exchanger is increased heat transfer rates under given pressure drop constraints.

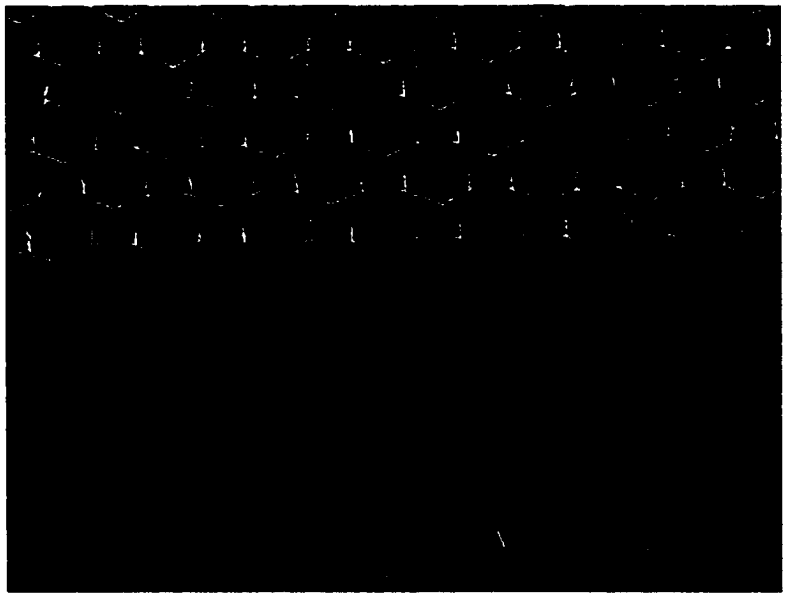

Figure VII.13 – Thick metal heat exchanger

Results

A metal cross flow micro heat exchanger was successfully fabricated. The flatness of the heat exchanger was verified by measuring the maximum deflection across the heat exchanger. Over the 1.5" heat exchanger width, the maximum deflection was only about 125 μm. Water was pumped through the heat exchanger with leakage from less than 0.5% of the air channels. A plated heat exchanger was broken in numerous pieces

to investigate if the plastic had been completely dissolved. No plastic was seen indicating that the ultrasonically agitated solvent successfully removed all of the plastic. Measurements of geometrical parameters of the heat exchanger were taken using an optical microscope coupled with a displacement measurement system. Statistical data of the measurements are summarized in Table VII.5.

Table VII.5 – Measurements (in μm) of fabricated metal heat exchanger

		Mean	Standard Deviation	Design
Water channel width (b)	- polished face	180.5	3.0	150
	- molded side	174.6	2.5	
Heat exchanger thickness (L)	- sample 1	1254.2	10.3	1100
	- sample 2	1257.3	21.1	
Plated hexagon side length (w)	- sample 1	238.0	2.9	244
	- sample 2	227.4	4.7	
Metal wall thickness (t)	- sample 1	65.5 (305.3)	(4.2)	70
	- sample 2	72.1 (318.9)	(5.4)	

Values for the water channel width are given for both sides of the plastic piece. Measurements for the heat exchanger thickness, plated hexagon side length, and metal thickness are given for the two heat exchangers that were tested since the thickness of the electroless plated layer is slightly different between heat exchangers. The measurements for the plated hexagon side length and the metal wall thickness were taken on the molded side to eliminate the contribution of lips possibly present from polishing. The thickness of the plated metal was estimated by measuring the distance between hexagons (shown in parenthesis in Table VII.5), subtracting the measured water channel width on the molded side, and dividing by two.

Since it impossible to take measurements of the water channel width dimension on the plated heat exchanger at random positions without breaking the heat exchanger, the width of the plastic honeycomb structures was measured and assumed to be equal to the

water channel width. The mean of the polished face water channel dimension is about 6 μm wider than the molded side water channel width dimension due to the fly cutting and polishing used to open the air channels. Conversely, the polished face plastic dimensions are expected to be about 2 μm wider than the molded side due to imperfect x-ray collimation. Therefore the lip created by the fly cutting and polishing step accounts for a widening of about 8 μm on the polished face. Consequently, an average lip size of about 4 μm is expected. Since these values are small compared to the overall geometrical dimensions, the heat exchanger performance is affected only slightly. Additional polishing with extra high grit sandpaper or briefly exposing the heat exchanger to solvent fumes could be used to reduce the lip caused by polishing.

The lateral dimensions determined by the conventional LIGA process differed by about 25 μm from the design values. The x-ray mask that had been used was the cause of the deviation. When the x-ray mask was fabricated, an extra thick layer of SJR resist (60 μm) was applied to enable plating of a thick (30-40 μm) gold absorber for patterning extra thick PMMA. The processing parameters for the thicker resist layer have not been optimized and a difference from the design dimensions resulted. The heat exchanger length also varied from the design. A thicker than expected piece of PMMA was used to fabricate the insert resulting mold insert structures with height of about 1.1 mm rather than 1.0 mm. Modeling calculations predict that the combined effect of the wider water channel and thicker heat exchanger will only cause a 1% enhancement in heat transfer under the design constraints.

The heat exchanger thickness varied by less than 2% over the area of the heat exchanger indicating successful fly cutting, polishing, and electroless plating. As

indicated by the small standard deviations of the plated hexagon side length and the metal thickness, electroless plating produced a uniform coating.

VII.4. Testing

The testing apparatus discussed in Chapter VI was used to measure the performance of the metal cross flow micro heat exchanger. The only difference was the method the heat exchanger was mounted. The metal heat exchanger required a testing device that directed the water from the inlet tube into the heat exchanger and from the heat exchanger to the exit tube. Other functions of the testing device are to direct the air to flow through the heat exchanger, to provide pressure taps to measure the pressure drop across the heat exchanger, and to insulate the heat exchanger to minimize heat losses from its edges. The testing device was made out of PMMA and is shown in Figure VII.14.

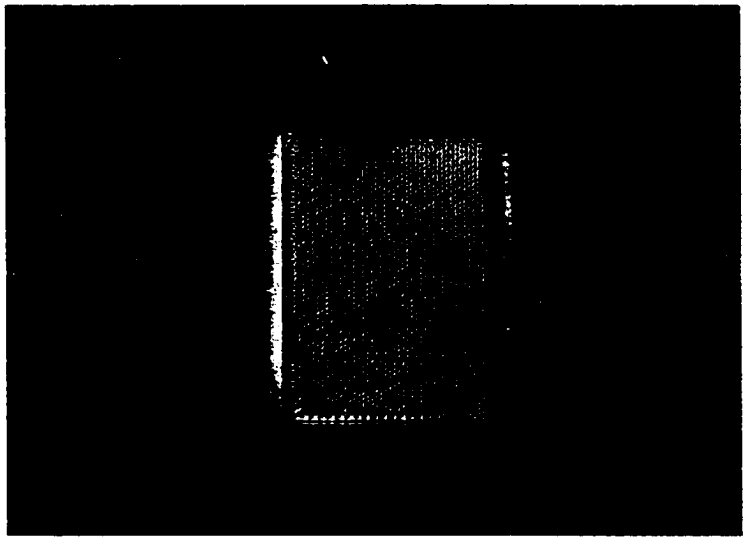

Figure VII.14 – Heat exchanger testing holder

The procedure described in Chapter VI was used to gather the experimental data. The only difference was in the water pressure drop measurement. The water pressure drop was measured directly using a differential pressure gage. Pressure losses

occurring in the testing device plenum were assumed negligible due to the low velocity of the water and the tortuous path the water traveled to pass through the heat exchanger.

Pressure drop and heat transfer testing was performed on a fabricated metal cross flow micro heat exchanger. The experimental data for the heat exchanger will be denoted as circles and the model predictions will be denoted as lines in the testing results.

The air pressure drop as a function of air velocity is shown in Figure VII.15. At low pressure drops, the model predicts a lower pressure drop than measurements indicate and at high pressure drops, the model predicts a higher pressure drop than measurements indicate. At the air pressure drop design constraint of 175 Pa, the model accurately predicted the pressure drop. The pressure drop is expected to be less than the model for high flow rates due to the rounded inlet and exit. This effect was accounted for in the loss coefficients however the friction factor for developing flow did not take the rounded nature of the inlet and exit into account. For low pressure drops, the effect of the rounded inlet and exit is expected to be reduced. The higher than predicted measured pressure drops for low flow rates may be caused by imperfections such as small bumps in the air channels.

Results for the water pressure drop are shown in Figure VII.16. Although the water pressure drop is difficult to predict, the model provides accurate estimates (within 20%) of the measured pressure drops. At low Reynolds numbers, the model slightly underpredicts the water pressure drop. The deviation between the model and the experimental data is about 10% at the water pressure drop constraint of 5 kPa. At higher Reynolds numbers, the agreement is excellent.

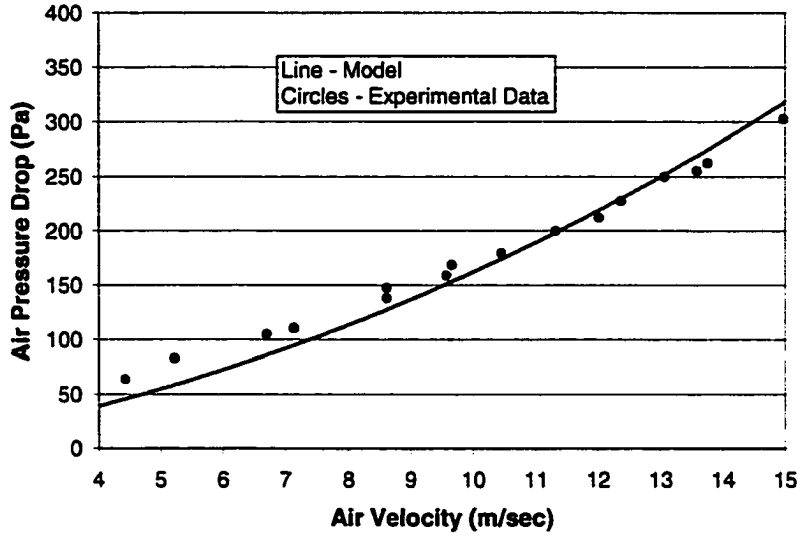

Figure VII.15 – Air pressure drop results

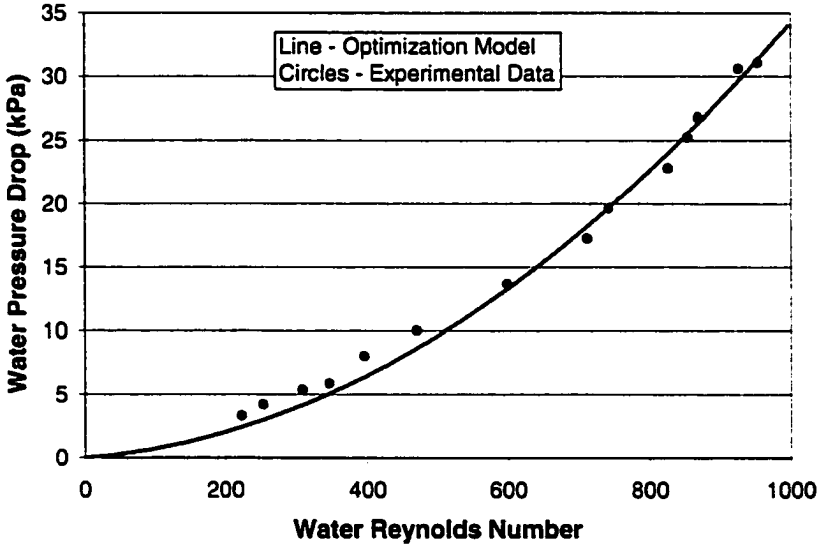

Figure VII.16 – Water pressure drop results

The percentage change of air temperature as a function of air velocity is shown in Figure VII.17. The agreement between the experimental results and the model is very good indicating the heat transfer model is accurate.

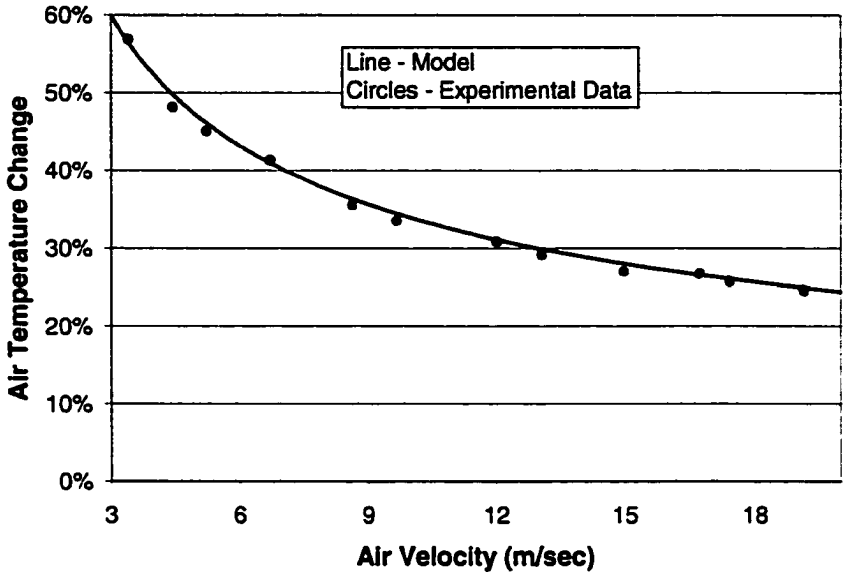

Figure VII.17 – Heat transfer results as a function of air velocity

The percentage change of air temperature as a function of air pressure drop is shown in Figure VII.18. Although this figure is a better measure of performance than Figure VII.17, inaccuracies in the pressure drop calculations and measurements are conveyed in the heat transfer results. At low pressure drops, the model predicts a lower temperature change than measurements indicate and at high pressure drops, the model predicts a higher temperature change than measurements indicate. Even though the heat transfer model may be accurate, inaccuracies of the pressure drop model lead to the deviations.

The normalized rate of heat transfer as a function of air pressure drop is shown in Figure VII.19. Although this figure is the best measure of performance, inaccuracies in the pressure drop and flow rate calculations and measurements are conveyed in the heat transfer results. At low pressure drops, the model predicts less heat transfer than measurements. Inaccuracies of the pressure drop model lead to the deviations. Near the

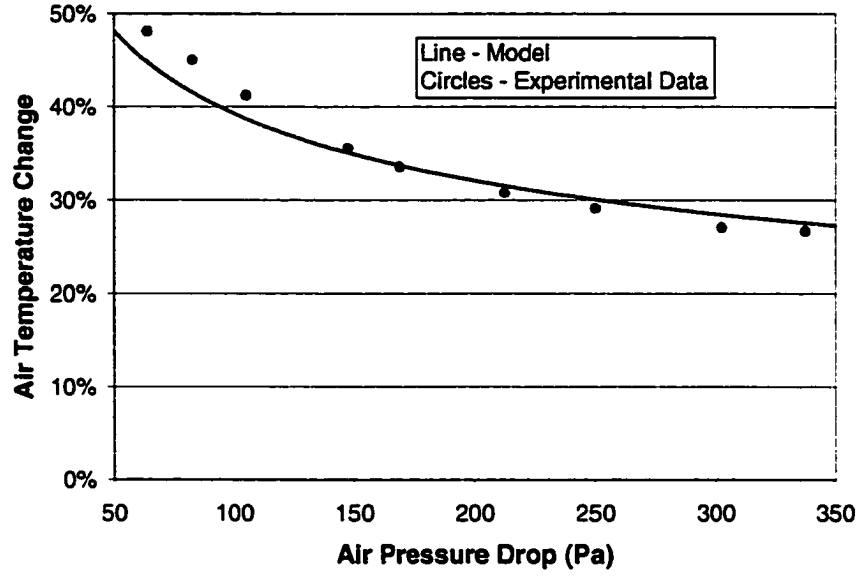

Figure VII.18 – Heat transfer results as a function of air pressure drop

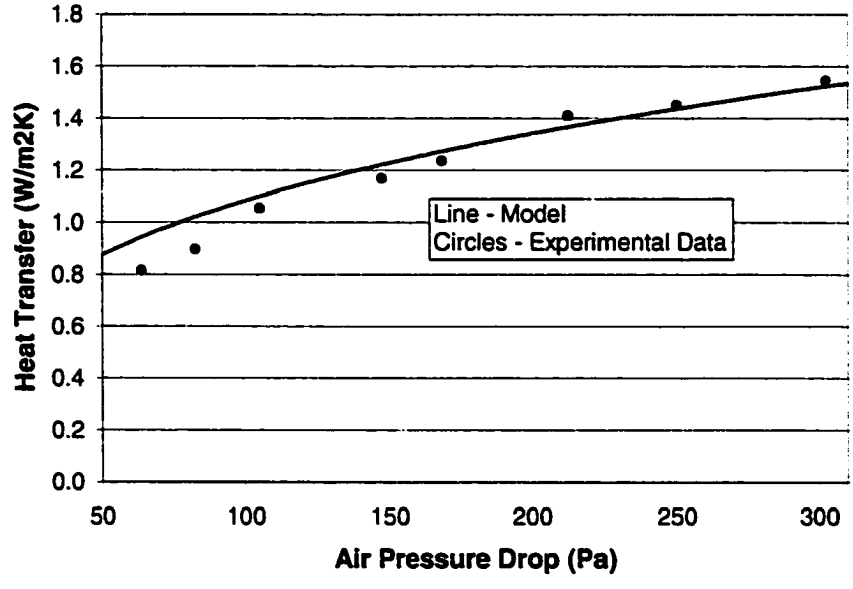

Figure VII.19 – Heat transfer as a function of air pressure drop

air pressure drop design constraint of 175 Pa, the model predicted the heat transfer accurately.

The testing apparatus limited the maximum allowable air and water pressures. Due to pressure losses between the compressed air source and heat exchanger, the maximum

ttainable air pressure at the front face of the heat exchanger was 0.9 psi. At this pressure, there was no water leakage. The water pressure transducer limited the maximum allowable water pressure to 30 psi. For water pressures at the inlet plenum up to 30 psi, no heat exchanger leakage was observed.

CHAPTER VIII - PERFORMANCE DISCUSSION

The mathematical model used to predict heat exchanger performance was validated in the pressure drop and heat transfer experiments. At the design constraints, the model predicted the air pressure drop and heat transfer performance within 10% of the measured performance for the plastic and nickel-phosphorous fabricated cross flow micro heat exchangers. Using the model for the plastic cross flow micro heat exchanger, predictions for ceramic and aluminum heat exchangers were calculated. A comparison of both types of cross flow micro heat exchangers' performance with current innovative car radiators and a cross flow micro heat exchanger with equal channel dimensions is shown in Table VIII.1. The fabricated plastic cross flow heat exchanger type will be denoted with a (1) and the fabricated metal cross flow heat exchanger will be denoted with a (2). Car radiators provide the best basis of comparison due to their similar design, heat transfer media (liquid and gas), and pressure drops to the cross flow micro heat exchanger.

Table VIII.1 – Heat exchanger performance comparison

Heat Exchanger	Δp_{gas} (Pa)	Δp_{liq} (kPa)	Q/(AΔT) (kW/m^{2}K)	Q/(VΔT) (kW/m^{3}K)	Q/(mΔT) (W/kgK)
Fabricated Plastic (1)	**175**	**5.0**	**0.58**	**400**	**692**
Ceramic (1)	175	5.0	1.14	810	619
Aluminum (1)	175	5.0	1.33	918	679
Aggressive Design (1)	175	5.0	3.64	910	1720
Fabricated Metal (2)	**175**	**5.0**	**1.30**	**1036**	**440**
Metal Aggressive Design (2)	175	5.0	2.71	677	349
Car Radiator (1 Row) [1]	179	1.7	3.12	123	283
Car Radiator (2 Row) [1]	204	7.4	3.11	98	252
Cross Flow Micro – Equal Channel Dimensions [20]	1010	6.1 (N_2)	6.38	455	138

The fabricated cross flow micro heat exchangers exhibit lower rates of heat transfer/frontal area however have far greater rates of heat transfer/volume or mass compared to innovative car radiators. This can be important in applications where heat exchanger volume and weight need to be kept to a minimum. If an aggressive geometrical design (minimum dimension = 50 μm, L = 4 mm) is implemented using hot water (T = 95°C), the rate of heat transfer/frontal area achieved can exceed that of innovative car radiators. For the plastic heat exchanger type of heat exchanger, the thermal conductivity and density for the aggressive design was assumed to be 100 W/m-K and 2,700 kg/m^3.

The pressure gradient in the liquid channels is about an order of magnitude greater for the cross flow micro heat exchangers than for the innovative car radiators. This is often unimportant since considerably greater power is required to pump the air than the water. If the pressure gradient within the cross flow micro heat exchangers needed to be reduced by an order of magnitude, the heat transfer for the plastic and metal cross flow heat exchangers would only be reduced by 16% and 20%, respectively. If higher temperature liquids were used in the cross flow micro heat exchangers such as those used in car radiators, the pressure gradient would be reduced considerably because the viscosity of the liquid would be reduced.

In the innovative car radiator, the liquid was a water-glycol mixture. Although this changes some of the fluid properties such as specific heat and viscosity, the overall heat transfer difference in using water-glycol instead of water is very small (<2%). Two reasons a water-glycol mixture is used as an engine coolant are the mixture's boiling point is higher than water and the mixture's freezing point is lower than water.

The fabricated cross flow micro heat exchangers exhibit similar rates of heat transfer/volume and greater rates of heat transfer/mass compared to a cross flow micro heat exchanger with equal channel dimensions that transfers heat between nitrogen streams. The cross flow micro heat exchanger with equal channel dimensions also has a considerably greater gas pressure drop because its micro channels are long compared to their diameter (i.e. high L/D^2 ratio). As a result, the cross flow micro heat exchanger with equal channel dimensions has a higher rate of heat transfer/frontal area. As mentioned previously, the cost and time involved in manufacturing and bonding together numerous plates (100 plates were used to achieve a 1 cm tall heat exchanger) is a disadvantage of the cross flow micro heat exchanger with equal channel dimensions.

The performance of the fabricated plastic and metal cross flow micro heat exchangers is shown in Figure VIII.1. For the same air pressure drop, the heat transfer in the metal heat exchanger is about twice the heat transfer for the plastic heat exchanger. Advantages of the plastic heat exchanger are greater heat transfer/mass, low cost, and the ability to fabricate the heat exchanger out of a multitude of materials. Advantages of the metal heat exchanger are greater rates of heat transfer/area and volume, resistance to high temperature fluids, and ease of fabrication.

A final issue that has not been addressed is the strength of the micro heat exchangers. Since the current designs are only 1-2 mm thick, additional reinforcement may be necessary to withstand the vibration, shock, and stagnation pressure applied to the front face of the heat exchanger. This would slightly reduce the heat transfer/volume or weight.

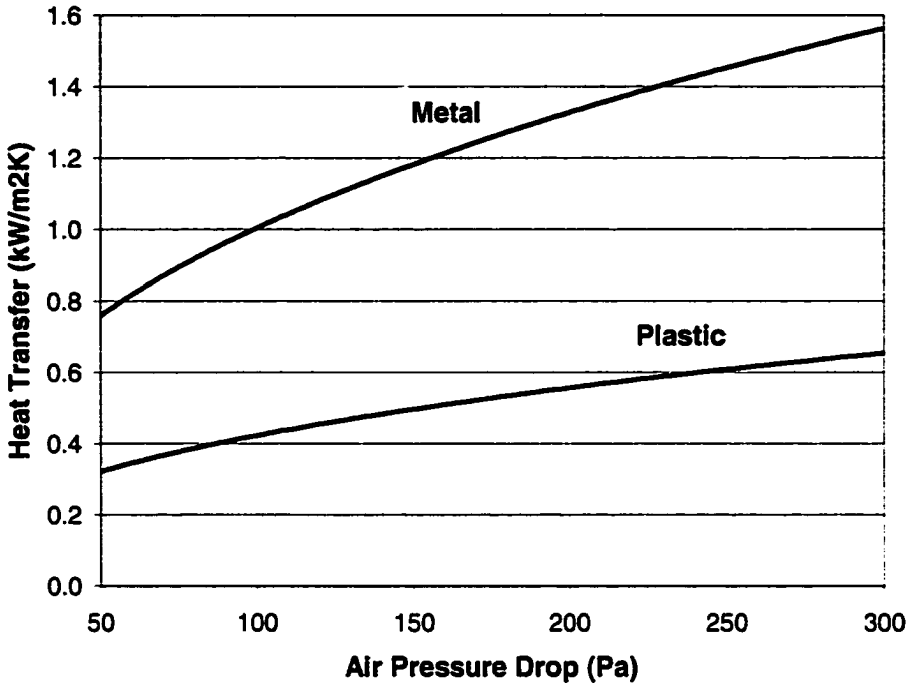

Figure VIII.1 – Performance of fabricated heat exchangers

CHAPTER IX – CONCLUSIONS AND RECOMMENDATIONS

IX.1. Conclusions

Cross flow micro heat exchangers were developed to efficiently transfer heat between a gas and a liquid in a small volume. The optimum design for two types of heat exchangers under a set of design constraints was determined. Additionally, a finite element analysis was performed for a plastic heat exchanger to more accurately model the heat transfer. Using the geometries determined in the optimization, cross flow micro heat exchangers were successfully fabricated out of PMMA and nickel-phosphorous. The PMMA heat exchanger was fabricated using the LIGA process with bonding and alignment steps. The nickel-phosphorous heat exchanger was fabricated using the LIGA process with sputtering and electroless plating. Channel sizes for these heat exchangers were an order of magnitude smaller than those found in compact heat exchangers. A testing apparatus was developed to measure the pressure drop and heat transfer performance. Using the test apparatus, fabricated heat exchangers were tested to validate the models. At the design constraints, the mathematical models predicted the fluid pressure drops and heat transfer performance within 10% of the measured performance.

Different cross flow micro heat exchanger designs were compared to innovative car radiators due to their similarity in design. Although the rate of heat transfer/frontal area was lower, rates of heat transfer/volume or mass for the cross flow micro heat exchangers far exceeded the innovative car radiators. Using aggressive design constraints, the cross flow micro heat exchanger concept has the ability to transfer a

greater rate of heat transfer/frontal area than an innovative car radiator while maintaining its rate of heat transfer/volume and mass advantage.

IX.2 Recommendations for Future Work

Successful fabrication of plastic and nickel-phosphorous cross flow micro heat exchangers under modest design constraints has been achieved. For the heat exchanger fabricated using the LIGA process, alignment, and bonding, fabricating the heat exchanger out of a material with better thermal properties can achieve better thermal performance. Methods of fabrication such as ceramic molding and metal injection molding should be explored since they are potentially inexpensive and rapid means of producing very high performance micro heat exchangers. To reduce the cost of the metal cross flow micro heat exchanger, electroplating nickel on a thinner electroless plated layer should be investigated because the cost of electroplating solutions are about an order of magnitude less than electroless plating solutions. Methods of cleaning the molded pieces of plastic after the backing has been removed should also be investigated and the subsequent fabrication steps (sputtering and electroless plating) should be performed in a cleanroom environment to minimize the defects that cause leakage.

Within any given fabrication technology, the most aggressive design constraints feasible need to be determined and used in the design of the micro heat exchanger. Currently, the frontal area of heat exchangers made using the LIGA process is limited to a size of approximately 0.01 m^2. In order for these heat exchangers to be useful in many applications, technologies need to be developed to enable the fabrication of micro heat exchangers with frontal areas up to 1 m^2. Other application specific aspects that need to be examined are filtering requirements and strength of the heat exchanger.

BIBLIOGRAPHY

1. R. Webb, P. Farrell, "Improved thermal and mechanical design of copper/brass radiators", SAE Technical Paper Series 900724.

2. M. Parrino, A. Parola, L. Dentis, "A high efficiency mechanically assembled aluminum radiator with real flat tubes", SAE Technical Paper Series 940495.

3. A. M. Kays, A. L. London, Compact Heat Exchangers, 3rd Ed., 1984, pages 108-114.

4. D. Tuckerman, R. Pease, "High-performance heat sinking for VLSI", IEEE Electron Device Letters, Vol. 2, No. 5, May 1981, pages 126-129.

5. B. Gromoll, "Advanced micro air-cooling systems for high density packaging", Tenth IEEE SEMI-THERM, 1994, pages 53-58.

6. M. Kleiner, "High performance forced air cooling scheme employing microchannel heat exchangers", IEEE Transactions on Components, Packaging, and Manufacturing Technology, Part A., Vol. 18, No. 4, December 1995, pages 795-804.

7. C. Hilbert, S. Sommerfeldt, O. Gumpta, D. Herrell, "High performance micr-channel air cooling", Sixth IEEE SEMI-THERM Symposium, 1990, pages 108-113.

8. R. Wegeng, K. Drost, "Developing new miniature energy systems", Mechanical Engineering, September 1994, pages 82-85.

9. J. M. Cuta, W. D. Bennett, C. E. McDonald, T. S. Ravigururajan, "Fabrication and testing of micro-channel heat exchangers", SPIE Microlithography and Metrology in Micromaching, Vol. 2640, 1995, pages 152-160.

10. L. J. Missaggia, J. N. Walpole, Z. L. Liau, R. J. Phillips, "Microchannel heat sinks for two-dimensional high-power-density diode laser arrays", IEEE Journal of Quantum Electronics, Vol. 25, No. 9, September 1989, pages 1988-1992.

11. K. Azer, R. S. McLeod, R. E. Caron, "Narrow channel heat sink for cooling of high powered electronic components", Eigth IEEE SEMI-THERM Symposium, 1992, pages 12-19.

12. R. Hahn, A. Kamp, A. Ginolas, M. Schmidt, J. Wolf, V. Glaw, M. Topper, O. Ehrmann, H. Reichl, "High power multichip modules employing the planar embedding technique and microchannel water heat sinks", Thirteenth IEEE SEMI-THERM Symposium, 1997, pages 49-56.

13. N. Goldberg, "Narrow channel forced air heat sink", IEEE Transactions on Components, Hybrids, and Manufacturing Technology, Vol. CHMT-7, No. 1, March 1984, pages 154-159.

14. S. Kitajo, Y. Takeda, Y. Kurokawa, T. Ohta, H. Mizunashi, "Development of a high performance air cooled heat sink for multi-chip modules", Eigth IEEE SEMI-THERM Symposium, 1992, pages 119-124.

15. R. Knight, J. Goodling, B. Gross, "Optimal thermal design of air cooled forced convection finned heat sinks – experimental verification", IEEE Transactions on Components, Hybrids, and Manufacturing Technology, Vol. 15, No. 5, October 1992, pages 754-760.

16. R. Beach, W. Bennet, B. Freitas, D. Mundinger, B. Comaskey, R. Solarz, M. Emanuel, "Modular microchannel cooled heatsinks for high average power laser diode arrays", IEEE Journal of Quantum Electronics, Vol. 28, No. 4, April 1992, pages 966-975.

17. W. Bier, W. Keller, G. Linder, D. Seidel, K. Schubert, "Manufacturing and testing of compact micro heat exchangers with high volumetric heat transfer coefficients", Microstructures, Sensors, and Actuators, ASME DSC-Vol.19, 1990, pages 189-197.

18. S. Kang, Micro Cross Flow Heat Exchanger, Dissertation, Louisiana Tech University, 1992.

19. D. Rachkovskij, E. Kussul, S. Talayev, "Heat exchange in short microtubes and micro heat exchanger with low hydraulic losses", Microsystem Technologies, Vol. 4, 1998, pages 151-158.

20. W. Bier, W. Keller, G. Linder, D. Seidel, K. Schubert, H. Martin, "Gas to gas transfer in micro heat exchangers", Chemical Engineering and Processing, Vol. 32, 1993, pages 33-43.

21. P. Wu, W. A. Little, "Measurement heat transfer characteristics of gas flow in fine channel heat exchangers used for microminiature refrigerators". Cryogenics, Vol. 24, pg. 415-420, 1984.

22. P. Wu, W. A. Little, "Measurement of friction factors for the flow of gases in very fine channels used for microminiature Joule Thomson refrigerators", Cryogenics, Vol. 23, pg. 273-277, 1983.

23. G. W. Swift, A. Migliori, J. C. Wheatley, Microchannel crossflow fluid heat exchangers and method for its fabrication, US patent 4,516,632 (1995).

24. D. Kountouris, Fabrication, modeling, and testing of a thrust bearing surface with integral micro heat exchanger, Thesis, LSU, 1999.

25. J. C. Coynel, A study of a micro heat exchanger for turbine blades, Thesis, LSU, 1999.

26. C. Marques, Heat transfer of microstructure-covered cylinder in crossflow, Thesis, LSU, 1997.

27. A. L. Tonkovich, C. J. Call, D. M. Jimenez, R. S. Wegeng, M. K. Drost, "Microchannel heat exchangers for chemical reactors", Proc. of the 1996 National Heat Transfer Conference, Houston, Texas.

28. A. L. Tonkovich, J. L. Zilka, M. R. Powell, C. J. Call, "The catalytic partial oxidation of methane in a microchannel chemical reactor", 1998, Pacific Northwest Laboratory.

29. P. Sandberg, "Take another look at your heat exchanger test data – a method to read between lines in the test data table", SAE Technical Paper Series 9311423.

30. J. Pfahler, J. Harley, H. Bau, J. N. Zemel, "Gas and liquid flow in small channels", Micromechanical Sensors, Acutators, and Systems, DSC-Vol. 32, pg. 49-60, 1991.

31. M. I. Flik, B. I. Choi, K. E. Goodson, "Heat transfer regimes in microstructures", DSC-Micromechanical Sensors, Actuators, and Systems, Vol. 32, pg. 31-47, 1991.

32. S. B. Choi, R. F. Barron, R. O. Warrington, "Fluid flow and heat transfer in microtubes", DSC-Micromechanical Sensors, Actuators, and Systems, Vol. 32, pg 123-134, 1991.

33. Z. Y. Guo, X. B. Wu, "Compressibility effect on the gas flow and heat transfer in a microtube", International Journal of Heat and Mass Transfer, Vol. 40, No. 13, pg. 3251-3254, 1997.

34. C. Ho, Y. Tai, "Micro-electro-mechanical-systems (MEMS) and fluid flows", Annual Review of Fluid Mechanics, Vol. 30, 1998, pages 579-612.

35. X. F. Peng, G. P. Peterson, "Convective heat transfer and flow friction for water flow in microchannel structures", International Journal of Heat and Mass Transfer, Vol. 39, No. 12, pg. 2599-2608, 1996.

36. X. F. Peng, G. P. Peterson, "The effect of thermofluid and geometrcial parameters on convection of liquids through rectangular microchannels",

International Journal of Heat and Mass Transfer, Vol. 38, No. 4, pg. 755-758, 1995.

37. X. F. Peng, G. P. Peterson, "Frictional flow characteristics of water flowing through rectangular microchannels", Journal of Experimental Heat Transfer, Vol. 7, No. 4. pg. 249-264, 1995.

38. B. X. Wang, X. F. Peng, "Experimental investigation on liquid forced-convection heat transfer through microchannels", International Journal of Heat and Mass Transfer, Vol. 37, Supp. 1, pg. 73-82, 1994.

39. X. F. Peng, B. X. Wang, G. P. Peterson, H. B. Ma, "Experimental investigation of heat transfer in flat plates with rectangular microchannels", International Journal of Heat and Mass Transfer, Vol. 38, No. 1. pg. 127-137, 1995.

40. S. Kakac, R. Shah, W. Aung, Handbook of Single Phase Convective Heat Transfer, 1987.

41. J. Brandup, E. Immegert, Polymer Handbook, John Wiley and Sons, New York, 3rd Ed, 1989.

42. M. Madou, Fundamentals of Microfabrication, CRC Press, 1997, pages 275-324.

43. P. Bley, W. Menz, W. Bacher, K. Feit, M. Harmening, H. Hein, J. Mohr, W. K. Schomburg, W. Stark, "Application of the LIGA process in fabrication of three-dimensional mechanical microstructures", Microprocess 91, Int. Microprocess Conf., Kanazawa, Japan, 1991, pages 384-389.

44. J. Gottert, P. Coane, F. DeCarlo, Y. Desta, D. C. Mancini, "Lithographic fabrication of graphite-based x-ray masks", 42nd Electron Ion and Photon Beam Technology and Nanofabrication (EIPBN) Conf., Chicago, IL, 1998.

45. C. Harris, Y. Desta, K. Kelly, G. Calderon, "Inexpensive, quickly producible x-ray mask for LIGA", Microsystems Technologies, (5) 1999 pages, 189-193.

46. S. K. Griffiths, J. M. Hruby, A. Ting, "The influence of feature sidewall tolerance on minimum absorber thickness for LIGA x-ray masks", Journal of Micromechanics and Microengineering, Vol. 9, pages 353-361.

47. C. G. Khan Malek, S. S. Das, "Adhesion promotion between poly (methylmethacrylate) and metallic surfaces for LIGA evaluated by shear stress measurements", Journal of Vacuum Science Technology B16(6), Nov/Dec 1998, pages 3543-3546.

48. S. S. Das, C. G. Khan Malek, "Adhesion promotion by surface-modification at the PMMA-metal interface for LIGA-type processing", Mat. Res. Soc. Symp. Proc., Volume 518, 1998, pages 149-154.

49. B. Chaudhuri, H. Guckel, J. Klein, K. Fischer, "Photoresist application for the LIGA process", Microsystem Technologies, Vol. 4, pages 159-162.

50. R. Buchhold, A. Nakladal, G. Gerlach, K. Sahre, K. Eichhorn, M. Muller, "Reduction of mechanical stress in micromachined components caused by humidity-induced volume expansion of polymer layers", Microsystem Technologies, Vol. 5, pages 3-12.

51. A. C. Henry, R.L. McCarley, S. Das, K. Malek, D. S. Poche, "Structural changes in PMMA under hard X-ray radiation", Microsystem Technologies, Vol. 4, pages 104-109.

52. V. Ghica, W. Glashauser, "Verfahren fur die Spannangsfreie Entwicklung von Bestrahlten Polymethyl-methacrylat-Schichtyen", Offenlegungsschrift, DE3039110, Siemens AG, Munich, Germany.

53. M. Despa, Injection molding of high aspect ratio microstructures, Thesis, LSU, 1998.

54. M. Keckele, W. Bacher, K. D. Muller, "Hot-embossing – The molding technique for plastic microstructures", Microsystem Technologies, Vol. 4, pages 122-124.

55. R. Ruprecht, T. Benzler, T. Hanemann, K. Muller, J. Konys, V. Poitter, G. Schanz, L. Schmidt, A. Theis, H. Wollmer, J. Haubelt, "Various replication techniques for manufacturing three-dimensional metal microstructures", Microsystem Technologies, Vol. 4, pages 28-31.

56. K. Fischer, J. Klein, B. Chaudhuri, H. Guckel, "Design and fabrication of one millimeter high structures", Microsystem Technologies, Vol. 4, pages 176-179.

57. H. Becker, W. Dietz, "Microfluidic devices for μ-TAS applications fabricated by polymer hot embossing", SPIE Conf. on Microfluidic Devices and Systems, Vol. 3515, Sept. 1998, pages 177-182.

58. S. Ford et al., "Micromachining plastics using x-ray lithography for the fabrication of micro-electrophoresis devices", Journal of Biomechanical Engineering, Vol.121, 1999, pages 13-17.

59. "Joining plastics", Machine Design, September 14, 1995, pages 77-78.

60. E. Petrie, "Adhesive bonding plastics: meeting an industry challenge", Adhesives Age, May 15, 1989, pages 6-13

61. N. Rouse, "Improved methods for thermo-plastic bonding", Machine Design, April 11, 1985, pages 72-79.

62. J. Rotheiser, Joining of Plastics, 1st Ed., 1999.

63. F. Beer, E. Johnston, Mechanics of Materials, McGraw Hill, 1992, pages 377-379.

64. W. Riedel, Electroless Nickel Plating, ASM International, 1998.

65. R. Sadasivam, R. M. Manglik, M. A. Jog, "Fully developed forced convection through trapezoidal and hexagonal ducts", International Journal of Heat and Mass Transfer, Volume 42, 1999, pages 4231-4331.

66. R. Fox, A. McDonald, Introduction to Fluid Mechanics, John Wiley and Sons, New York, 4th Ed., 1992.

67. R. Suchentrunk, Metallizing of Plastics – A Handbook of Theory and Practice, ASM International, 1993.

68. Callister, W.D., Materials Science and Engineering – 3rd Ed., John Wiley and Sons, 1994.

69. F. Incropera, D. DeWitt, Introduction to Heat Transfer, John Wiley and Sons, New York, 3rd Ed., 1996.

NOMENCLATURE

a – Thickness of wall that separates the water and air channels (μm)
A_{HT} – Total heat heat transfer area (m^2)
b – Width of water channel (μm)
c_p – Specific heat (kJ/kgK)
D_h – Hydraulic diameter (μm)
f – Friction factor
F_w – Overall width of heat exchanger (cm)
F_h – Overall height of heat exchanger (cm)
h – Convection coefficient (W/m^2K)
H – Height of air channel (μm)
k – Thermal conductivity (W/mK)
K – Loss coefficient for inlet and exit effects
L – Length of air channel (μm)
$\dot{m}$ - Mass flow rate (kg/sec)
N – Number of air channels
NTU – Number of heat transfer units
Nu – Nusselt number
Δp – Pressure drop of air or water (Pa)
Pr – Prandtl number
q – Total heat transfer (W)
$q_{channel}$ – Heat transfer for one air channel (W)
R_1 - Convection resistance at the water/wall interface (K/W)
R_2 - Conduction resistance of wall separating the water and air channels (K/W)
R_3 – Convection resistance at the air side, including resistance in the fin (K/W)
R_{tot} – Total resistance to heat transfer (K/W)
Re – Reynolds number
S - Sensitivity
T – Temperature of air or water (K)
T_{lm} – Log mean temperature difference between the water and air (K)
t – Metal thickness (μm)
V – Velocity (m/sec)
w – Width of air channel or hexagon side length(μm)
y – Width between air channels (μm)
U – Overall heat transfer coefficient (W/m^2K)
η_f – Fin efficiency
μ - Viscosity (kg/msec)
ρ - Density of fluid (kg/m^3)
Λ – Characteristic number for longitudinal conduction

APPENDIX A: PROGRAM FOR DESIGN OPTIMIZATION

Properties and Constants [69]

```
ρair = 1.15;
μair = 0.0000186;
kair = 0.0265;
cpair = 1007;
Prair = 0.707;
ρwater = 967;
μwater = 0.000489;
kwater = 0.65;
cpwater = 4184;
kwall = 0.193;
K = 1.6;
Tairinlet = 25;
Twaterinlet = 58;
Fh = 0.0508;
Fw = 0.0508;
Ratio = 0.5;
```

Notes - Ratio is the ratio of the water channel depth to the overall thickness (L) of the heat exchanger
- mks system of units is used
- Fluid properties at average fluid temperatures of Tair = 30 C, Twater = 57 C

Calculations

■ Step #1

```
Dhair[H_, w_] := 4 * H * w / (2 * (H + w))
```

■ Step #2

■ Friction factor - 1st iteration

```
Vairguess = 7;
Reairguess[H_, w_] := ρair * Vairguess * Dhair[H, w] / μair
xplusguess[H_, w_, L_] := L / (Dhair[H, w] * Reairguess[H, w])
fReguess[H_, w_, L_] := 11.206 * xplusguess[H, w, L] ^ (-0.252)
```

■ Velocity

```
Vair1[Pair_, H_, w_, L_] := (Pair / (4 fReguess[H, w, L] * ρair *
      L / (Reairguess[H, w] * 2 * Dhair[H, w]) + K * ρair / 2)) ^ .5
```

■ Friction factor-2nd iteration

```
Reairguess2[Pair_, H_, w_, L_] :=
 ρair * Vair1[Pair, H, w, L] * Dhair[H, w] / μair
xplusguess2[Pair_, H_, w_, L_] :=
 L / (Dhair[H, w] * Reairguess2[Pair, H, w, L])
fReguess2[Pair_, H_, w_, L_] :=
 11.206 * xplusguess2[Pair, H, w, L] ^ (-0.252)
Vair2[Pair_, H_, w_, L_] :=
 (Pair / (4 fReguess2[Pair, H, w, L] * ρair * L / (Reairguess2[
          Pair, H, w, L] * 2 * Dhair[H, w]) + K * ρair / 2)) ^ .5
```

■ Friction factor-3rd iteration

```
Reairguess3[Pair_, H_, w_, L_] :=
 ρair * Vair2[Pair, H, w, L] * Dhair[H, w] / μair
xplusguess3[Pair_, H_, w_, L_] :=
 L / (Dhair[H, w] * Reairguess3[Pair, H, w, L])
fReguess3[Pair_, H_, w_, L_] :=
 11.206 * xplusguess3[Pair, H, w, L] ^ (-0.252)
Vair[Pair_, H_, w_, L_] :=
 (Pair / (4 fReguess3[Pair, H, w, L] * ρair * L / (Reairguess3[
          Pair, H, w, L] * 2 * Dhair[H, w]) + K * ρair / 2)) ^ .5
```

■ **Friction factor-Final**

```
Reair[Pair_, H_, w_, L_] :=
 ρair * Vair[Pair, H, w, L] * Dhair[H, w] / μair
xplus[Pair_, H_, w_, L_] := L / (Dhair[H, w] * Reair[Pair, H, w, L])
fRe[Pair_, H_, w_, L_] := 11.206 * xplus[Pair, H, w,] ^ -0.252
```

■ Step #3

■ **Nusselt number**

```
xstar[Pair_, H_, w_, L_] := xplus[Pair, H, w, L] / Prair
Nuair[Pair_, H_, w_, L_] :=
 0.0343 / xstar[Pair, H, w, L] + 5.0446 + 7.2 * (0.2 - w / H)
```

■ Step #4

■ **Water convection coefficient**

```
Nuwater = 3.7;
Dhwater[b_, L_] := 4 * Ratio * L * b / (2 * (Ratio * L + b))
hwater[a_, b_, L_] := Nuwater * kwater / Dhwater[b, L]
```

■ Step #5

■ **Water convection resistance**

```
R1[a_, b_, L_, w_, y_] := 1 / (hwater[a, b, L] * (w + y) * L)
```

■ **Wall conduction resistance**

```
R2[a_, w_, y_, L_] := a / (kwall * (w + y) * L)
```

- **Air convection resistance**

```
hair[Pair_, H_, w_, L_] := Nuair[Pair, H, w, L] * kair / Dhair[H, w]
m[Pair_, H_, w_, L_, y_] :=
 ((2 * hair[Pair, H, w, L] / (y * kwall)) ^ .5) * H / 2
nf[Pair_, H_, w_, L_, y_] :=
 Tanh[m[Pair, H, w, L, y]] / m[Pair, H, w, L, y]
R3[Pair_, H_, w_, L_, y_] :=
 1 / (hair[Pair, H, w, L] * (nf[Pair, H, w, L, y] * H + w) * L)
```

- **Total resistance**

```
Rtot[Pair_, H_, w_, L_, y_, a_, b_] :=
 (R1[a, b, L, w, y] + R2[a, w, y, L] + R3[Pair, H, w, L, y]) / 2
```

- **Exit air temperature**

```
mdotair[Pair_, H_, w_, L_] := ρair * Vair[Pair, H, w, L] * H * w
qchannel[Pair_, H_, w_, L_, y_, a_, b_] :=
 -(Twaterinlet - Tairinlet) * Exp[-1 / (mdotair[Pair, H, w, L] *
       cpair * Rtot[Pair, H, w, L, y, a, b])] + Twaterinlet
Tairexit[Pair_, H_, w_, L_, y_, a_, b_] :=
 -(Twaterinlet - Tairinlet) * Exp[-1 / (mdotair[Pair, H, w, L] *
       cpair * Rtot[Pair, H, w, L, y, a, b])] + Twaterinlet
```

- **Heat transfer**

```
qchannel[Pair_, H_, w_, L_, y_, a_, b_] := mdotair[Pair, H, w, L] *
  cpair * (Tairexit[Pair, H, w, L, y, a, b] - Tairinlet)
Nair[H_, w_, y_, a_, b_] := Fh * Fw / ((b + 2 * a + H) * (y + w))
q[Pair_, H_, w_, L_, y_, a_, b_] :=
 Nair[H, w, y, a, b] * qchannel[Pair, H, w, L, y, a, b]
```

■ Step #6

■ Coolant exit temperature

```
Vwater[Pwater_, b_, L_] :=
 Dhwater[b, L]^2 * Pwater / (32 * μwater * Fw)
Nwater[H_, a_, b_] := Fh / (b + 2 * a + H)
mdotwater[Pwater_, b_, L_, H_, a_] :=
 ρwater * Vwater[Pwater, b, L] * Ratio * L * b * Nwater[H, a, b]
Twaterexit[Pair_, H_, w_, L_, y_, a_, b_, Pwater_] :=
 Twaterinlet - q[Pair, H, w, L, y, a, b] /
   (mdotwater[Pwater, b, L, H, a] * cpwater)
```

■ Heat transfer correction

```
Twateravg[Pair_, H_, w_, L_, y_, a_, b_, Pwater_] := Twaterinlet -
  (Twaterinlet - Twaterexit[Pair, H, w, L, y, a, b, Pwater]) / 2
qfinal[Pair_, H_, w_, L_, y_, a_, b_, Pwater_] :=
 q[Pair, H, w, L, y, a, b] *
  (Twateravg[Pair, H, w, L, y, a, b, Pwater] - Tairinlet) /
   (Twaterinlet - Tairinlet)
```

■ Step #7

Optimize heat transfer under the design constraints using iterative method.

Results

■ Table 1 Data

```
Nair[0.00075, 0.0002, 0.0002, 0.000125, 0.0005]
```

```
4301.07
```

```
Vair[175, 0.00075, 0.0002, 0.00145]
```

```
7.92915
```

```
Reair[175, 0.00075, 0.0002, 0.00145]
```

```
154.814
```

```
qfinal[175, .00075, .0002, .00145, .0002, .000125, .0005, 5000]
```

```
57.6
```

Note: The heat transfer shown in Table 1 was obtained from the finite element analysis

■ Sensitivity calculation example

```
Sensw = (qfinal[175, .00075, .0002, .00145,
     .0002, .000125, .0005, 5000] - qfinal[175, .00075,
     .00019, .00145, .0002, .000125, .0005, 5000]) *
  .0002 / (.00001 * qfinal[175, .00075, .0002, .00145,
      .0002, .000125, .0005, 5000])
```

```
-0.222226
```

■ Plots

In addition to the plot of heat transfer rate (Q) vs. (a) shown in the text, the following graphs give the heat transfer effect of changing design variables.

■ Q vs. b

```
Plot[qfinal[175, .00075, .0002, .00145, .0002, .000125, b, 5000],
 {b, 0.0001, 0.0011}]
```

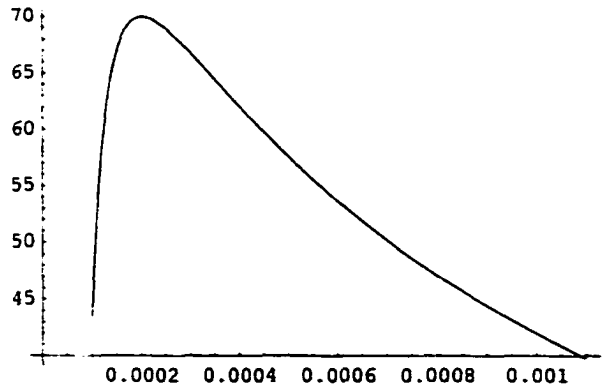

■ **Q vs. L**

```
Plot[qfinal[175, 0.00075, .0002, L, .0002, .000125, .0005, 5000],
 {L, 0.001, 0.004}]
```

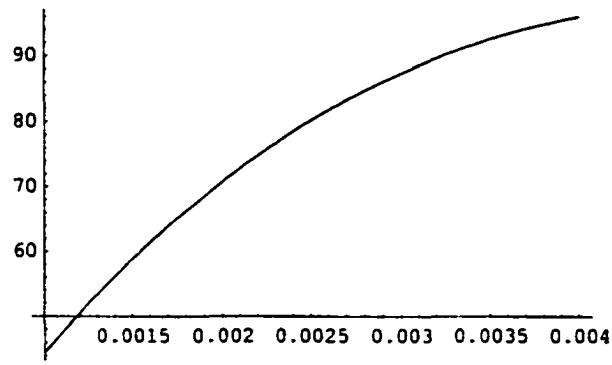

■ **Q vs. Pair**

```
Plot[qfinal[Pair, 0.00075, .0002, .00145,
  .0002, .000125, .0005, 5000], {Pair, 100, 500}]
```

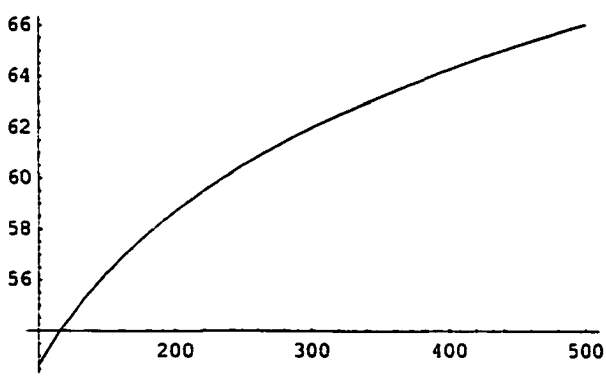

APPENDIX B: FINITE ELEMENT MODELING

The finite element model used to account for three-dimensional effects is presented in this section. Using the geometry calculated in the optimization analysis, a unit cell volume was constructed. The boundaries of the unit cell were at planes of symmetry. A finite difference solution using ANSYS was then performed to obtain the solution to the following steady state three-dimensional heat equation with no heat generation.

$$\frac{\partial^2 T}{\partial x^2}+\frac{\partial^2 T}{\partial y^2}+\frac{\partial^2 T}{\partial z^2}=0 \qquad (13)$$

The surface boundary conditions used in the solution are shown in Figure B.1.

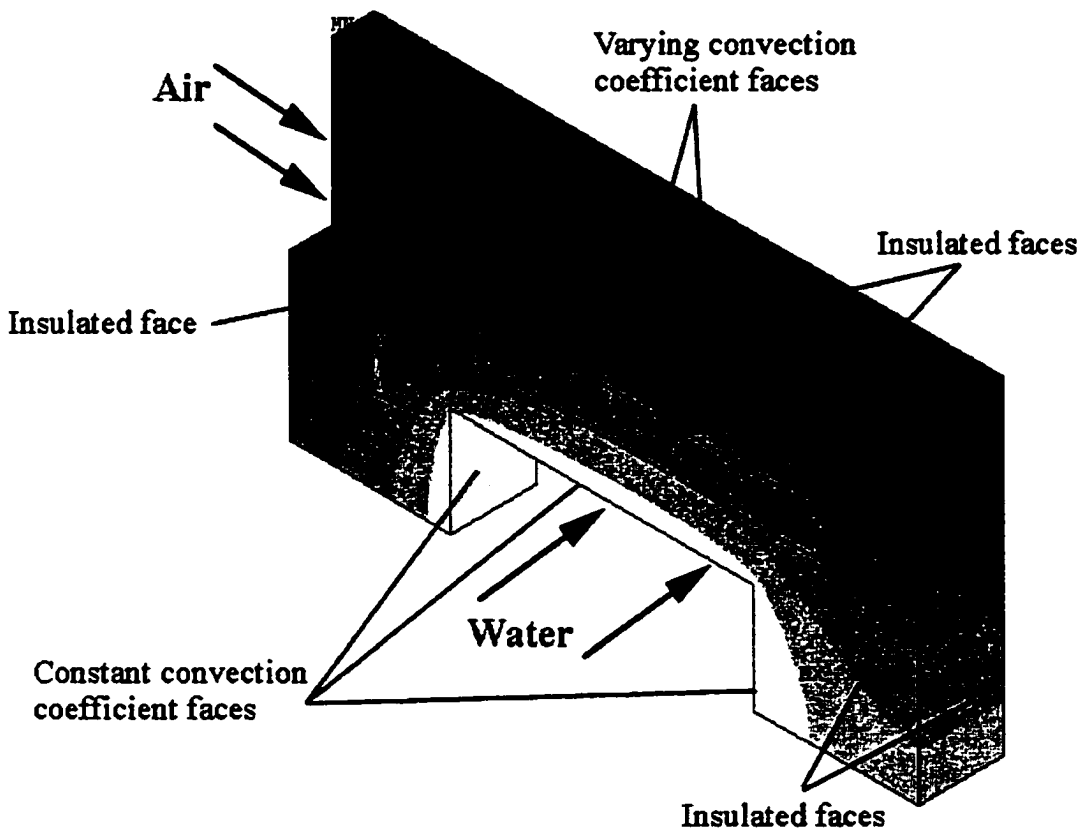

Figure B.1 – Boundary conditions for unit cell

The two types of boundary conditions used in the finite element solution are the insulated surface condition and the convection surface condition. The front and rear faces as well as the planes of symmetry had the following insulated surface condition.

$$\left.\frac{\partial T}{\partial x}\right|_{x=0} = 0 \tag{15}$$

The x direction is normal to the plane of the surface. The water and air channel surfaces had the following convection surface condition.

$$-k\left.\frac{\partial T}{\partial x}\right|_{x=0} = h(T_{fluid} - T_{surface}) \tag{16}$$

Along the length of the air channel, the convection coefficient was varied since the air is developing in the channel. The water channel convection coefficient was held constant in the water channel. Assumptions of macroscale fluid behavior for convection coefficient correlations and negligible front and rear face heat transfer were used in the solution.

In order to vary the air channel convection coefficient down the length of the channel, the unit cell volume was divided into 13 sections using planes normal to the direction of air flow. Each section had a different convection coefficient that was obtained from curve fit tabular empirical correlations [40]. Since the convection coefficient changes rapidly near the inlet of the air channel, the sections in this region were narrower than the sections near the exit of the air channel.

The air temperature used in the air channel surface boundary conditions was also varied for each of the 13 sections. Initial estimates of the air temperatures were obtained using the optimization analysis equations for the exit temperature of the air. The air was assumed to exit the air channel at a length equal to the distance from the inlet of the air channel to the midpoint of each section. The finite element analysis using ANSYS was then performed resulting in the temperature field for the unit cell.

For the plastic heat exchanger, the average temperatures at the base of the fin varied considerably from the optimization analysis in some sections (Figure 8). As a result, the estimates of the air temperature using the optimization analysis were not accurate. An iterative method was used to correct the initial solution. The method is based on the heat transfer being approximately proportional to the temperature difference between the base of the fin and the air at a given length down the air channel. A corrected air temperature was estimated sequentially beginning at the channel entrance using Equation (17).

$$T_{air-corr-2} = \left(T_{air-inlet} - T_{air-exit}\right)_{opt}\left(\frac{\left(T_{base-fe} - T_{air-avg}\right)}{\left(T_{base-opt} - T_{air-avg}\right)}\right) + T_{air-corr-1} \quad (17)$$

where: $\left(T_{air-inlet} - T_{air-exit}\right)_{opt}$ is the temperature change of the air across one section in the optimization analysis.

$\left(T_{base-fe} - T_{air-avg}\right)$ is the difference in the average temperature at the base of the fin determined using the finite element analysis (fe) and the average temperature of the air in the section.

$\left(T_{base-opt} - T_{air-avg}\right)$ is the difference in the average temperature at the base of the fin calculated using the optimization analysis (opt) and the average temperature of the air in the section.

$T_{air-corr-1}$ is the previous section's corrected air temperature.

The corrected air temperatures are used to perform another finite element analysis to determine a new temperature profile for the unit cell. The air temperatures are again corrected using Equation (18) with the previously corrected air temperatures and the new temperature profile at the base of the fin.

$$T_{air-corr-2} = (T_{air-inlet} - T_{air-exit})_{opt}\left(\frac{(T_{base-fe} - T_{air-avg})}{(T_{base-fe-1} - T_{air-avg})}\right) + T_{air-corr-1} \qquad (18)$$

The only difference between Equations (17) and (18) is the replacement of the temperature at the base of the fin calculated using the optimization analysis ($T_{base-opt}$) by the temperature at the base of the fin determined by the first iteration of the finite element analysis ($T_{base-fe-1}$).

An additional iteration results in a negligible change in the predicted heat transfer (<1%). The finite element analysis predicted heat transfer was then calculated using Equation (19).

$$q = \dot{m}c_p(T_{air-exit} - T_{air-inlet}) \qquad (19)$$

The heat transfer was calculated for three different average air channel velocities (4.4 m/sec, 7.7 m/sec, 10.7 m/sec). The results for the average air channel velocity of 7.7 m/sec are shown in Table 5. The difference between the predicted heat transfer for the optimization and finite element analysis was about 15% for each of the flow velocities.

Table 5 – Finite element analysis results for V=7.7 m/sec

Section (μm from air channel inlet)	T-base-opt.	T-air-opt. at inlet of section	T-base-f.e.	T-air-corr. at inlet of section	T-base-f.e.	T-air-corr. At inlet of section
0-50	35.89	25.00	34.00	25.00	33.97	25.00
50-100	41.60	25.71	35.80	25.59	35.70	25.59
100-150	43.95	26.22	37.30	25.90	37.13	25.91
150-200	45.30	26.65	38.90	26.17	38.65	26.19
200-250	46.15	27.06	40.40	26.44	40.08	26.46
250-300	46.90	27.45	42.00	26.71	41.60	26.73
300-375	47.51	27.82	43.78	26.99	43.28	27.02
375-475	48.31	28.36	45.80	27.43	45.19	27.47
475-675	48.90	29.06	47.80	28.03	47.09	28.09
675-875	49.56	30.38	49.36	29.28	48.59	29.36
875-1075	49.99	31.63	49.36	30.52	48.58	30.62
1075-1250	50.41	32.82	47.70	31.66	46.91	31.79
1250-1450	50.75	33.81	45.70	32.50	44.87	32.65
Exit		**34.90**		**33.25**		**33.45**

APPENDIX C: UNCERTAINTY ANALYSIS

Uncertainty analysis is a procedure to quantify accuracy and data validity. The goal of this section is to estimate the uncertainty of experimental measurements and calculated results due to random error. It is assumed that the testing equipment was calibrated and checked properly to ensure negligible fixed errors.

The uncertainty analysis will be broken down into the following three steps [65]:

1. Estimation of the uncertainty interval for the measured quantities.
2. Analysis of the confidence interval for each measurement.
3. Determination of the propagation of uncertainty into experimental data results.

The following analysis will involve the estimation of the uncertainty at the design conditions (P_{air} = 175 kPa, V_{air} = 7.9 m/sec, P_{water} = 5 kPa, Re_{water} = 690, $\%\Delta T_{air}$ = 25%).

C.1. Step 1: Estimation of the uncertainty interval for the measured quantities

The uncertainty interval for the measured data is estimated by plus or minus the smallest scale division of the measurement instrument. Estimates for the absolute and relative uncertainty are shown in Table C.1.

Table C.1 - Estimates of measurement uncertainty

	P_{air}	P_{water}	T	FR_{air}	FR_{water}
Absolute (+/-)	0.025"H_2O	0.005 psi	0.05°C	0.25 cfm	0.025 lpm
Relative (% +/-)	3.6	0.7	0.6	2.3	4.2

The relative uncertainty of the temperature measurement was estimated for the design air temperature difference of 8.3°C. This gives the maximum uncertainty for temperature measurements.

C.2. Step 2: Analysis of the confidence interval for each measurement

The confidence interval will be estimated using the experimenter's testing experience. The estimation is selected such that 95% of the readings (two standard deviations) will likely fall into the confidence interval. These odds are typically used for engineering work.

For pressure drop and flow rate measurements, the confidence intervals are the same as the uncertainty intervals. For reasons described in Chapter VI - Testing, the temperature measurements contain additional uncertainty. The confidence interval for the inlet air temperature is estimated to be ±0.1°C due to the inconsistency of temperature measurements between thermocouples. The confidence interval for the exit air temperature is estimated to be ±0.25°C due to the inconsistency of temperature measurements between thermocouples and the exit air temperature variations. The confidence interval for the average water temperature is estimated to be ±0.2°C due to the inconsistency of temperature measurements between thermocouples and the heat losses between the thermocouples and the inlet and exit of the water channels.

C.3. Step 3: Determination of the propagation of uncertainty into experimental data results

The uncertainty (u) of an experimental result (R) due to the combined effects of uncertainty intervals for measurements of independent variables (x_1, x_2, ..., x_n) is calculated using Equation (60) [65].

$$u_R = \pm\left[\left(\frac{x_1}{R}\frac{\partial R}{\partial x_1}u_1\right)^2 + \left(\frac{x_2}{R}\frac{\partial R}{\partial x_2}u_2\right)^2 + \ldots + \left(\frac{x_n}{R}\frac{\partial R}{\partial x_n}u_n\right)^2\right]^{1/2} \qquad (60)$$

The following quantities were experimental results given in Chapter VI - Testing: P_{air}, P_{water}, V_{air}, Re_{water}, $\%\Delta T_{air}$, and ΔT_{water}. The uncertainty of each of these quantities is investigated below.

Pressure Drops

The uncertainty interval for the fluid pressure drops (P_{air} and P_{water}) are the uncertainty interval range stated in Step 1.

Air channel velocity

The uncertainty of the average air channel velocity (V_{air}) is due to the combined uncertainties of the water flow rate and the open area for air to flow through the heat exchanger. The confidence interval for the open area for air to flow through the heat exchange is estimated to be ±2%. The average air velocity through the air channels is given by Equation (61).

$$V_{air} = \frac{FR_{air}}{OpenArea} \tag{61}$$

The necessary differentiation of Equation (61) is performed and substituted into Equation (60) to derive Equation (62). This equation is used to calculate the uncertainty of the air velocity.

$$u_{V_{air}} = \pm\left[\left(u_{FR_{air}}\right)^2 + \left(-u_{OpenArea}\right)^2\right]^{1/2} \tag{62}$$

The resulting uncertainty interval for the average air channel velocity is ±3%.

Water channel Reynolds number

The uncertainty of the average water channel Reynolds number (Re_{water}) is due to the combined uncertainties of the water flow rate, the open area for water to flow through the heat exchanger, and the hydraulic diameter. The confidence interval for the open

area for air to flow through the heat exchanger and hydraulic diameter are estimated to be ±3% and ±2% using the measurements given in Table 3. The average water channel Reynolds number is given by Equation (63).

$$Re_{water} = \frac{\left(\frac{FR_{water}}{OpenArea}\right) D_{h-water}}{\nu_{water}} \tag{63}$$

The kinematic viscosity of the water is assumed to have negligible uncertainty due to the uncertainty of the water temperature compared to the other uncertainties. The necessary differentiation of Equation (63) is performed and substituted into Equation (60) to derive Equation (64). This equation is used to calculate the uncertainty of the water channel Reynolds number.

$$u_{Re_{water}} = \pm\left[\left(u_{FR_{water}}\right)^2 + \left(-u_{OpenArea}\right)^2 + \left(u_{D_{h-water}}\right)^2\right]^{1/2} \tag{64}$$

The resulting uncertainty interval for the average water channel Reynolds number is ±6%.

Percentage temperature change of the air

The uncertainty of the percentage temperature change of the air (Equation (70)) is due to the combined uncertainties of the inlet air temperature, exit air temperature, and water temperature. The necessary differentiation of Equation (70) is performed and substituted into Equation (60) to derive Equation (65). This equation is used to calculate the uncertainty of the percentage change of the air temperature.

$$u_{\%\Delta T} = \pm \left[\left(\frac{T_{air-exit}}{T_{air=exit} - T_{air-inlet}} u_{T_{air-exit}} \right)^2 + \left(\frac{T_{air-inlet}}{T_{air=exit} - T_{air-inlet}} u_{T_{air-inlet}} \right)^2 + \left(\frac{T_{water}}{T_{water} - T_{air-inlet}} u_{T_{water}} \right)^2 \right]^{1/2} \quad (65)$$

The resulting uncertainty interval for the percentage temperature change is ±3%.

Water temperature change across the heat exchanger

The uncertainty for the temperature change of the water across the heat exchanger is the confidence interval for the temperature change of the water divided by the temperature change of the water under design conditions. The resulting uncertainty is 15%. This is why the calculation of the heat transfer is more accurately performed using air temperature measurements (discussed in Chapter VI – Testing).

Heat transfer

Using the calculated uncertainties for the air channel velocity and air inlet and exit temperatures, the heat transfer uncertainty is calculated using Equation (66).

$$u_q = \pm \left[\left(u_{FR_{air}} \right)^2 + \left(\frac{T_{air-exit}}{T_{air=exit} - T_{air-inlet}} u_{T_{air-exit}} \right)^2 + \left(\frac{T_{air-inlet}}{T_{air=exit} - T_{air-inlet}} u_{T_{air-inlet}} \right)^2 \right]^{1/2} \quad (66)$$

The resulting uncertainty interval for the heat transfer is ±4%.

APPENDIX D: MICROFABRICATION PROCEDURES

D.1. X-Ray Mask Fabrication Procedure

1. Polish graphite.
    a. Adhere graphite to clean glass plate using spray mist.
    b. Polish with 600 grit sandpaper.
    c. Polish with polishing paper.
    d. Use tissue to clean off remaining graphite dust.
    e. Remove from glass using isopropyl alcohol.
2. Secure graphite to silicone wafer using 9% PMMA.
    a. Spin PMMA at 3000 RPM for 30 seconds.
    b. Bake at 180°C for 1 hour.
3. If desired, add layer of metal to reduce resist absorption in the graphite by sputtering or electroplating.
4. Spin SJR 5740 optical resist at 1000 RPM for 30 seconds for a thickness of 20 μm. Let soak for 6 minutes.
5. Bake sample - Put in oven at 65°C. Heat to 95°C for 5 min. Reduce temperature to 60°C. Remove from oven. Let cool.
6. Expose to ultraviolet light for dose of 600 mJ/cm^2. (35 seconds at CAMD's exposure station)
7. Develop in 354 developer for 15 minutes. Look for residue. Rub q-tip dipped in acetone across developed surfaces to ensure no residue is present.
8. Electroplate gold using galvanostatic pulse plating and a Technic gold plating bath.

a. Current density = 0 or 2 mA/cm^2

b. Plating rate = 3 μm/hour

c. Temperature = 45°C

9. Dissolve SJR 5740 resist in acetone.
10. Secure graphite mask to frame.

D.2. PMMA Bonding Procedure

1. Cut PMMA in circles.
2. Clean PMMA using soap and water followed by isopropyl alcohol.
3. Anneal PMMA at 80°C for several hours. Ramp up at about 3°C/min and ramp down at about 1°C/min.
4. Clean thick (1/4") titanium substrate first using soap and water, then a dilute (2.5%) solution of hydrofluoric acid.
5. Oxidize titanium surface using an aqueous solution consisting of 20 g/L sodium hydroxide and 6.1 g/L hydrogen peroxide at 65°C. Keep in solution for 15 minutes.
6. Bake titanium at 180°C and cool [49].
7. Mix bonding solution consisting of 8.5 g MMA (methylmethacrylate), 0.5 g powdered PMMA, 0.15 g benzoyl peroxide, and 0.1 g dimethyl analine.
8. Bond PMMA to titanium using MMA bonding solution. Use minimum amount of solution to achieve completely coat the titanium/PMMA interface. This is about four to six drops for a four inch circle. This corresponds to about 10 μl per square inch [49]. Press out air bubbles. Press at 60 psi for 24 hours.

VITA

Chad was born on July 20th, 1975, in Chicago, Illinois.

In 1993, he began his college education at Louisiana State University. During his time as an undergraduate, he studied mechanical engineering and competed on Louisiana State University's men's golf team.

Chad started his doctoral studies in mechanical engineering in January 1998 as a member of the Microsystems Engineering Team (μSET) at Louisiana State University with Dr. Kevin Kelly as graduate advisor. His project focused on the transfer of heat from a liquid to a gas in a small volume using micro channels. He will earn the degree of Doctor of Philosophy at the May 2001 commencement.

MASTER'S EXAMINATION AND THESIS REPORT

Candidate: Chad Harris

Major Field: Mechanical Engineering

Title of Thesis: Design, Fabrication, and Testing of Cross Flow Micro Heat Exchangers

Approved:

Kevin W. Kelly
Major Professor and Chairman

Dean of the Graduate School

EXAMINING COMMITTEE:

Warren M. Wagenfeld

Richard L. Bengston

Date of Examination:

March 23, 2001